Dielectron production in proton-proton collisions with ALICE

Doctoral Thesis by Markus Konrad Köhler
July 2014

TECHNISCHE
UNIVERSITÄT
DARMSTADT

Institut für Kernphysik
Prof. Dr. Peter Braun-Munzinger
Prof. Dr. Jochen Wambach

Dissertation

Dielektronenproduktion in Proton-Proton Kollisionen mit ALICE

Vom Fachbereich Physik
der Technischen Universität Darmstadt

zur Erlangung des Grades
eines Doktors der Naturwissenschaften
(Dr. rer. nat.)

genehmigte Dissertation von
Markus Konrad Köhler, M.Sc.
aus Lich

Referent : Prof. Dr. Peter Braun-Munzinger
Korreferent : Prof. Dr. Jochen Wambach

Tag der Einreichung: 15.07.2014
Tag der mündlichen Prüfung: 20.10.2014

Darmstadt 2015
D 17

Abstract

Ultrarelativistic hadron collisions, such as delivered since a couple of years at the Large Hadron Collider (LHC), provide new insights into the properties of strongly interacting matter at high temperatures and densities, which is expected to have existed a few of a millionth seconds after the big bang. Electromagnetic probes, such as leptons and photons, are emitted during the entire collision. Since they do not undergo strong interactions, they reflect the entire evolution of the collision.

Pairs of leptons, so called dileptons, have the advantage compared to real photons, that they do not only carry momentum, but also have a non-zero invariant mass. The invariant mass spectrum of dileptons is a superposition of several components and allows to address different characteristics of the medium.

To understand dielectron production in heavy-ion collisions, reference measurements in proton-proton (pp) collisions are necessary. pp collisions reflect the vacuum contribution of the particles produced in heavy-ion collisions. The analysis of pp collisions is an essential step towards the extraction of medium influences on the vector meson spectral functions and the thermal radiation in heavy-ion collisions.

In this thesis, the production of electron-positron pairs (dielectrons) in pp collisions at a collision energy of 7 TeV in the ALICE central barrel is analysed. ALICE has unique particle identification capabilities at low momentum. Electrons and positrons are identified with a high purity and combined to pairs. The invariant mass distribution of dielectrons is corrected for detector effects and the selection criteria in the analysis with Monte Carlo simulations.

The dielectron invariant mass spectrum of known hadronic sources is calculated based on the cross sections measured in other decay channels using the known decay kinematics. This so called hadronic cocktail represents the dielectron spectrum at the moment of kinematic freeze-out and can be compared to the measured dielectron invariant mass spectrum. The cocktail is consistent with the measured dielectron invariant mass spectrum within the quoted statistical and systematic uncertainties.

Additionally, the fraction of direct over inclusive virtual photons is measured as a function of transverse momentum from dielectron yields at high pair momentum. The ratio is used to calculate the cross section of direct real photons, which is compared to next-to-leading order perturbative Quantum-Chromodynamics calculations. The theoretical calculations are consistent with the measurement for pp collisions at a centre-of-mass energy of 7 TeV.

The analysis and results of this work are the basis for future dielectron measurements of heavier collision systems.

Zusammenfassung

Ultrarelativistische Hadronenkollisionen, wie sie seit wenigen Jahren am Large Hadron Collider (LHC) untersucht werden, eröffnen neue Einsichten in die Eigenschaften der stark wechselwirkenden Materie bei hohen Temperaturen und Dichten, so wie sie für wenige millionstel Sekunden nach dem Urknall existiert hat. Elektromagnetische Sonden, wie Leptonen und Photonen, werden während der gesamten Kollision emittiert und erfahren darüber hinaus keine starke Wechselwirkung, wodurch gemessene Leptonenspektren die gesamte Evolution einer Schwerionenkollisionen widerspiegeln.
Paare von Leptonen, so genannte Dileptonen, haben den Vorteil gegenüber reellen Photonen, dass sie nicht nur Impuls tragen, sondern auch eine nicht verschwindende invariante Masse haben. Das Dileptonenkontinuum ist eine Überlagerung unterschiedlicher Komponenten und erlaubt die Untersuchung verschiedener Eigenschaften des Mediums.
Um spätere Analysen von Schwerionenkollisionen und die daraus folgenden Ergebnisse interpretieren zu können, müssen Referenzmessungen in Proton-Proton (pp) Kollisionen vorgenommen werden. pp Kollisionen spiegeln die Teilchenproduktion des Vakuumanteils von Schwerionenkollisionen wider. Die Analyse von pp Kollisionen stellt somit einen essentiellen Baustein für das Verständnis der Spektralfunktionmodifikationen von Vektormesonen und thermischer Strahlung in Schwerionenkollisionen dar.
In dieser Arbeit wird die Produktion von Elektron-Positron Paaren (Dielektronen) in pp Kollisionen bei einer Schwerpunktsenergie von 7 TeV in dem zentralen Teil des ALICE Detektorsystems untersucht. ALICE hat unter allen LHC Experimenten einzigartige Teilchenidentifikationsmöglichkeiten bei niedrigen Impulsen. Elektronen und Positronen können mit einer hohen Reinheit identifiziert und zu Paaren kombiniert werden. Das Massenspektrum der Dielektronen wird auf Detektoreinflüsse und die während der Analyse angewandten Auswahlkriterien auf Teilchen- und Paarebene mithilfe von Monte Carlo Simulationen korrigiert.
Bekannte hadronische Dielektronenquellen werden anhand ihrer gemessenen Wirkungsquerschnitte in anderen Zerfallskanälen und der erwarteten Dielektronenkinematik zu einem Dielektronenspektrum zusammengefasst. Dieser sogenannte hadronische Cocktail repräsentiert die Vakuumkomponenten des Dielektronenspektrums zu dem Zeitpunkt der Kollision, an dem sich die

Teilchenkomposition nicht mehr ändert und kann mit den gemessenen Spektren verglichen werden. Der Cocktail beschreibt das gemessene Dielektronenspektrum innerhalb der statistischen und systematischen Fehler.

Darüber hinaus lässt sich aus Dielektronen bei hohen Paarimpulsen der Beitrag direkter virtueller Photonen zum Dielektronenspektrum messen. Damit kann der Wirkungsquerschnitt direkter reeller Photonen als Funktion des Transversalimpulses berechnet werden, der mit Next-to-leading-order Berechnungen perturbativer Quanten-Chromodynamik verglichen wird. Die theoretischen Berechnungen sind konsistent mit dem gemessenen Wirkungsquerschnitt für pp Kollisionen bei einer Kollisionsenergie von 7 TeV.

Die Analyse und die Ergebnisse dieser Arbeit bilden die Grundlage für zukünftige Dielektronenmessungen an schwereren Kollisionssystemen.

Acknowledgements

It is a satisfying challenge to thank for all the help and the support during these years working in the ALICE group at GSI. It is satisfying, because one gets the chance to name all the people involved in the preparation of this thesis. But it also remains as a challenge, since so many people, whose names would fill many pages, came along for a longer or shorter part of this journey and contributed in the one or the other, sometimes non-scientific, way.

First of all, I would like to thank my family. The last ten years of study would have been impossible without their unconditional love, help and support. I can not put into words, what they mean to me.

I would also like to thank my wife for her patience during all these times, especially in the last months. I guess it is never easy to live together with a physicist. However, she managed it in a remarkable way and I am thankful for her love and for her companionship during the last twelve years.

Of course, deep gratitude goes to Prof. Peter Braun-Munzinger, who let me be a part of the ALICE group. Without his support, I guess also many times in the background without my knowledge, life would have been much harder. I am thanking Ralf Averbeck for many discussions and his mental support in stressful times. Silvia Masciocchi, Anton Andronic, Marian Ivanov, Ilya Selyuzhenkov and Dariusz Miskowiec supported me with their knowledge whenever necessary.

An efficient work is only possible in a good atmosphere. Therefore I am thankful for the whole ALICE group at GSI, at Heidelberg and at Frankfurt. I want to thank Nicole Martin, Jaap Onderwaater, Jan Wagner, Steffen Weber, Jacek Otwinowski, Mikolay Krzewicki, Mariella Nicassio and Jochen Thäder. Special thanks also goes to my office mates: Michael Knichel, Rossella Romita, Julius Gronefeld, Mesut Arslandok and Helen Ricaud.

I also would like to thank Marcelo Munhoz for hosting me in Brazil for three months. The friendship to Marcel Figueredo, Thais Silva and Gabriel de Barros was a big help and fun during this time.

Also many thanks to Jochen Thäder and Torsten Kollegger for their help during my time at CERN working on the HLT and the TPC.

Working on a complex topic necessitates motivation and the support of the analysis group. Therefore gratitude goes to the entire low-mass dielectron group in ALICE, especially Taku Gunji, Hongyan Yang and Harald Appelshäuser.

Many thanks also go to Ralf Averbeck, Michael Winn, Benjamin Dönigus, Alberica Toia and Jochen Thäder for reading my thesis, cleaning up the mess and giving valuable comments and suggestions.

Contents

1. Introduction

Relativistic heavy-ion collisions provide the opportunity to recreate and study under laboratory conditions a form of matter, which is believed to have existed in the early phase of the universe, the Quark-Gluon Plasma (QGP). The goal of relativistic heavy-ion physics is to understand the properties of nuclear matter at high temperatures and densities as described by the theory of strongly interacting matter, Quantum Chromodynamics (QCD).

The self-interaction of gluons leads to a non-Abelian structure of QCD, which is known since about forty years to result in asymptotic freedom [1]. The strength of the interaction weakens for smaller distances, enabling the theoretical fundament for the deconfined state of matter, the QGP.

Already in the late 1950's, high energy proton beams were available at the AGS[1] at BNL[2] and at the PS[3] at CERN[4]. First heavy-ion beams, at that time still at non-relativistic energies, were available at the BEVALAC at LBNL[5] and the UNILAC at GSI[6].

Contemporary accelerators, such as the Relativistic Heavy Ion Collider at BNL or the Large Hadron Collider at CERN, collide heavy ions up to energies of $\sqrt{s_{\mathrm{NN}}} = 0.2$ TeV and $\sqrt{s_{\mathrm{NN}}} = 2.76$ TeV, respectively. At CERN it is planned for the next year to even increase the collision energy by almost a factor two to the design energy.

Even at the highest collision energies, the time scale for which highly energetic and dense matter is formed in heavy-ion collisions is short, about 10 fm$/c$. The system thermalises and only final state particles remain as remnants of the collision. Only these remnants and their decay products can be measured by a detector and models or simulations are needed to provide a connection to the early phases of the collision.

One possibility to directly access the earliest stages of a heavy-ion collision is via the measurement of particles, which do not interact strongly and leave the medium without strong rescattering.

Candidates for such probes are electromagnetically interacting particles, such as leptons and photons, or electroweakly interacting particles, such as $\mathrm{W}^{\pm}$ and Z^0 bosons. However, $\mathrm{W}^{\pm}$ and Z^0 bosons are particles created in hard scatterings exclusively at the early stage of a collision, while leptons and photons can be emitted also at later stages, i.e. during the entire collision evolution. Consequently, yields of electromagnetic probes measured with the detector reflect the entire collision evolution and can, moreover, also bridge the gap to hard probes.

---

[1] Alternating Gradient Synchrotron

[2] Brookhaven National Laboratory

[3] Proton Synchrotron

[4] Centre Europeen pour la Recherche Nucleaire

[5] Lawrence Berkeley National Laboratory

[6] GSI Helmholtzzentrum fuer Schwerionenforschung GmbH

The importance of electromagnetic probes was already pointed out in 1978 [2]. In the last few decades, real and virtual (e^+e^- and $\mu^+\mu^-$ pairs) photons, could shed light on the composition and production of the thermal and medium component emitted during the Quark-Gluon Plasma phase as well as the high density Hadron Gas phase.

The LHC produces hot and dense collision systems larger and longer living than at any other currently running facility in the world. The analysis and understanding of the low-mass dielectron production at high energies is one of the most challenging, but also one of the most fruitful opportunities to get new insights into the hot and dense matter produced in heavy-ion collisions.

Outline

This thesis is organised as follows: In chapter 2, the status quo of relativistic heavy-ion collisions is discussed, aiming to highlight the role of dilepton and in particular dielectron measurements for the understanding of this dynamic and very rapidly developing field of research. The theory of strongly interacting matter, Quantum Chromodynamics, is sketched based on the standard model of particle physics. Signatures of the hot and dense medium are connected to previous experimental results. Results from former dilepton measurements from the low energies up to top RHIC energies are discussed.

In chapter 3, the ALICE detector system is described briefly, focusing on the detector components used for this analysis.

In chapter 4, the commissioning of the online reconstruction and compression of clusters in the Time Projection Chamber during the Pb–Pb data taking in 2011 is summarised. The partial online data reconstruction is motivated and the different cluster finders are described and compared with each other. The quality of the tracks from clusters reconstructed online and offline is analysed in data and Monte Carlo simulations and compared with each other.

The main part of this thesis is presented in chapter 5. The dielectron data analysis in proton-proton collisions at $\sqrt{s} = 7$ TeV is discussed in detail. The selection of events and of electrons is shown, followed by the estimation of the combinatorial background and a discussion of the rejection of photon conversions. The dielectron efficiency correction based on Monte Carlo simulations is described in detail. The expected dielectron spectra from hadronic decays are constructed based on previous measurements of transverse momentum spectra and particle cross sections.

The corrected and absolutely normalised dielectron invariant mass spectra are compared to the expected dielectron spectra from hadronic sources in chapter 6. Moreover, the direct photon cross section is extracted via the measurement of virtual photons and it is compared to Next-to-Leading-Order perturbative QCD calculations.

In the end, an outlook for future dielectron measurements in ALICE is given in chapter 7.

2. Relativistic hadron collisions

A major interest in contemporary nuclear physics is the investigation and understanding of strongly interacting matter. Colliding particles in accelerators at relativistic energies opens up new perspectives and insights since a couple of decades by producing systems under extreme conditions in terms of density and temperature. The systematic evaluation of the properties of the hot and dense matter produced in hadron collisions led to a fascinating landscape of strongly interacting matter, see e.g. [3].

This chapter focuses on the theoretical and experimental description of the current understanding of hadron collisions at relativistic energies with a focus on the production of dileptons.

In section 2.1, the tools and fundamental formalisms for the underlying theory, Quantum Chromo-Dynamics (QCD), are briefly described. Calculations for the medium, which undergoes significant changes when entering extreme temperature or density regimes, will be addressed. Section 2.2 lists experimental observations, which characterize the main properties of the hot and dense medium. In section 2.3 the special character of dileptons and their importance for the understanding of the processes in relativistic hadron collisions will be emphasised. The richness of dielectron physics will be highlighted by the description of the variety of dielectron sources. Finally, in section 2.4, results from previous dilepton programs will be discussed.

If not stated otherwise, natural units $\hbar = c = 1$ are used.

2.1. Quantum Chromodynamics

The Standard Model (SM) of particle physics is the contemporary status quo for the description of the dynamics of subatomic particles and the interactions between them. It includes three forces, namely the weak, the electromagnetic and the strong interaction. However, since the standard model is not incorporating the gravitational force or the dark sector phenomena, it can be understood as an effective model. One of the biggest successes of the SM was the prediction of the Higgs boson, see e.g. [4, 5], which was recently discovered at the LHC [6, 7].

The SM distinguishes two types of elementary particles: fermions, which generate fields and bosons, which mediate fields. Bosons carry integer spins, fermions carry half-integer spins. The difference in the spin properties of bosons and fermions fundamentally influences the statistical behaviour and nature of these particles [8]. A compilation of fermions is listed in Table 2.1.

One can separate fermions in leptons and quarks. Leptons do undergo the electromagnetic and weak interaction and quarks interact strongly in addition. Bosons are the mediators of the three interactions, listed in Table 2.2.

		Particle		$Q/\lvert e\rvert$
leptons	e	μ	τ	-1
	ν_e	ν_μ	ν_τ	0
		Flavour		
quarks	u	c	t	$+2/3$
	d	s	b	$-1/3$

Table 2.1.: The fundamental fermions of the SM of particle physics subdivided in their three families. Leptons carry integer electrical charges and do not interact strongly. Quarks carry multiple third charges and interact via the strong interaction. The corresponding antiparticles are not shown.

Particle	Interaction	Charge	Mass $/(\mathrm{GeV}/c^2)$
gluon	strong	colour	0
photon	electromagnetic	electric	0
$W^\pm, Z^0$	weak	weak	$\approx 80, 91$

Table 2.2.: The fundamental bosons of the SM of particle physics mediating the strong, electromagnetic and weak interactions.

The strength of the three interactions varies over several orders of magnitude. The weak interaction is the weakest interaction and, moreover, the interaction with the shortest range[1].

Due to their massless gauge boson, the reach of the electromagnetic interaction is infinite. The difference of the strength between the strong and the electromagnetic interaction is caused by their coupling constants. The electromagnetic coupling constant, the fine structure constant, $\alpha_{\mathrm{e.m.}}$, can be determined by natural constants

$$\alpha_{\mathrm{e.m.}} = \frac{e^2}{4\pi\epsilon_0} \approx \frac{1}{137}, \tag{2.1}$$

where e and ϵ_0 are the elementary charge and the vacuum permittivity, respectively.

The theory of strong interaction, which describes the dynamics of colour-charged particles, is QCD. The coupling constant of the strong interaction, α_{s}, is about two orders of magnitude larger than the electromagnetic coupling constant. In first order approximation, the strong coupling as a function of momentum transfer Q^2 is given by

$$\alpha_{\mathrm{s}}(Q^2) \approx \frac{12\pi}{(11n - 2f)\ln(Q^2/\Lambda^2_{\mathrm{QCD}})}, \tag{2.2}$$

where n the number of colours and f the number of quark flavours. The value for the QCD scale parameter $\Lambda_{\mathrm{QCD}} \approx 213 \pm 8$ MeV [9] is the only intrinsic QCD parameter. The coupling constant of QCD as function of the momentum transfer Q^2 is shown in Figure 2.1. The points show experimental values, the line indicates a theoretical calculation.

---

[1] The reach of an interaction can be estimated by the energy-time uncertainty $\Delta E \Delta t \geq \hbar/2$ and the mass of the gauge bosons.

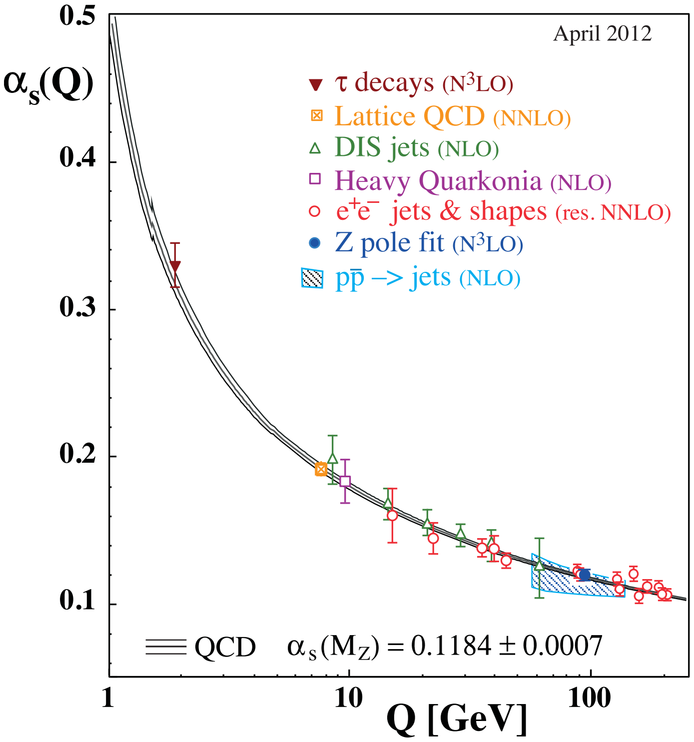

Figure 2.1.: The coupling constant of the strong interaction as a function of momentum transfer Q. From [10]

The strength of the coupling increases with small Q^2 (or large distance), i.e. quarks are confined and bound to colour-neutral states. However, the strength of the coupling decreases for large Q^2 (or small distance), i.e. quarks become quasi free particles at $\alpha_s(Q^2 \to \infty) \to 0$. This behaviour is called asymptotic freedom [1].

As a consequence of the asymptotic freedom, the existence of a state of deconfined matter was predicted at high temperatures and/or high densities [11, 12], the Quark-Gluon Plasma (QGP). Therefore, generating high temperatures or densities for a short period of time by colliding nuclei allows to produce and investigate this deconfined state of matter with partonic degrees of freedom. Previous experiments showed thermal and collective signatures for this phase transition from confined to deconfined matter, which is discussed in section 2.2.

The Lagrangian density $\mathcal{L}_{\mathrm{QCD}}$ of the strong interaction is given by

$$\mathcal{L}_{\mathrm{QCD}} = \bar{q}\left(i\gamma_\mu D^\mu - \mathcal{M}_q\right) q - \frac{1}{4} G^a_{\mu\nu} G^{\mu\nu}_a, \tag{2.3}$$

where the first term corresponds to quarks and their interaction and the second term to gluons and their (self-)interaction. The quark fields $q, \bar{q}$ are represented by the quark flavours, e.g. $q = (u, d, s)$ with a corresponding diagonal matrix $\mathcal{M}_q = \mathrm{diag}(m_u, m_d, m_s)$. The gluon field strength is given by $G^a_{\mu\nu}$, where a refers to the colour indices.

Other important characteristics of the QCD Lagrangian are related to symmetry principles. The QCD Lagrangian is based on a local colour SU(3) symmetry, in fact a gauge symmetry.

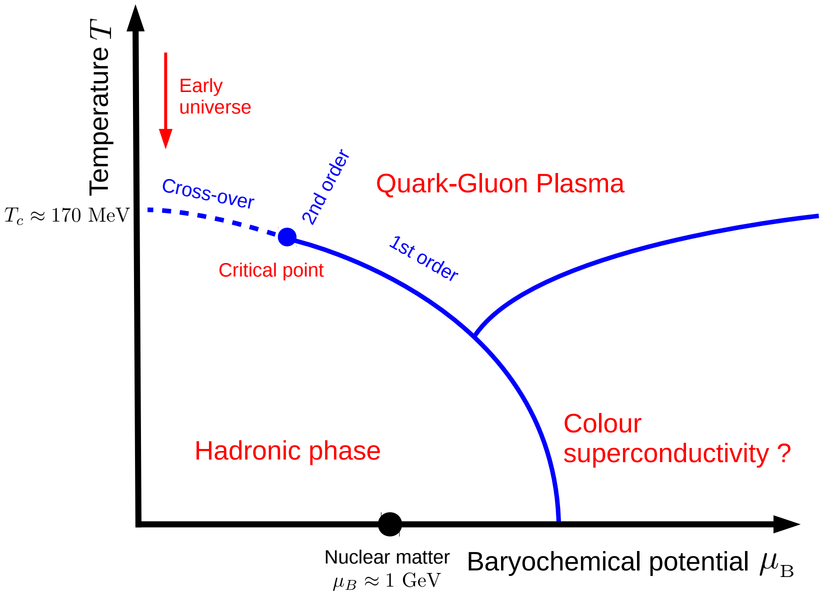

Figure 2.2.: Schematic phase diagram of QCD matter in the $\mu_{\mathrm{B}} - T$ plane. The three different phases are separated by phase transitions, indicated by lines. The transition from QGP to hadronic matter at vanishing baryochemical potential occurs at the temperature $T = T_c \approx 170$ MeV. The approximate density of ground state nucleons, atomic nuclei, is also indicated.

Quark fields can be subdivided in left-handed and right-handed components, where the handedness, or chirality[2], is given by the relative orientation of the spin and the direction of motion. For the case of non-vanishing quark masses, $\mathcal{M}_q \neq 0$, the left- and right-handed states mix and chiral symmetry is explicitly broken, but represents a good approximation. However, even in the chiral limit $\mathcal{M}_q = 0$, the chiral symmetry is spontaneously broken, which is the main symmetry breaking effect, see e.g. [13]. An order parameter for the spontaneous breaking of chiral symmetry is the chiral condensate $\langle q\bar{q}\rangle$, which is a result of QCD vacuum.

A schematic phase diagram of strongly interacting matter is shown in Figure 2.2. QCD matter is characterised by the temperature T and, to guarantee baryon number conservation, the baryochemical potential μ_{B}.

Three different phases of QCD matter may exist. At low temperature and low baryochemical potential matter exists in form of hadrons, which corresponds to the form of matter surrounding us in every day life. At high temperature and low baryochemical potential partons are in a deconfined state of matter, the QGP mentioned before. This state of matter can be produced in ultra-relativistic heavy-ion collisions. The phase at low temperature and high baryochemical potential, which is believed to be colour superconducting [14], may exist in the core of neutron stars, but is highly unlikely to play a role in ultrarelativistic heavy-ion collisions.

In Figure 2.2, the transitions between the different phases are indicated by lines, where the contin-

---

[2] Chirality is defined by the γ_5 Dirac matrix and the projection is given by $\frac{1\pm\gamma_5}{2}$ on the left $(-)$ and on the right $(+)$ component.

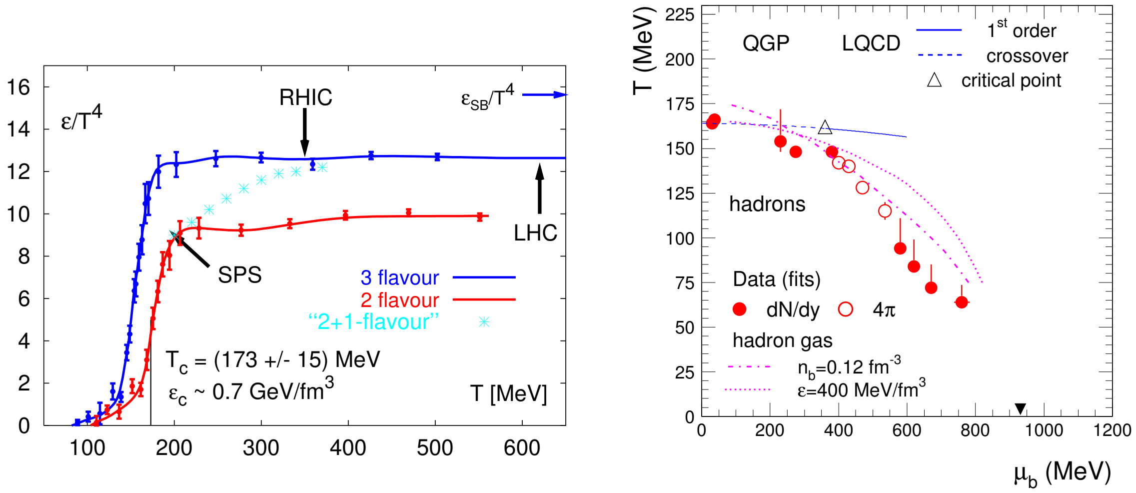

Figure 2.3.: Left: Energy density divided by the fourth power of the temperature as a function of temperature for three different cases sea quark flavours calculated on a discretized space-time lattice. From [15]. Right: Phase diagram of hadronic matter. The points characterize the system at chemical freeze-out. The blue line indicate the phase boundary from lattice, the magenta lines for freeze-out curves for a hadron gas for constant baryon density or energy density. From [16]

uous lines represent a phase transition of first order[3] and the dashed line is a cross-over. The dot indicates the position of a critical point[4].

Due to the strong coupling constant approaching unity with decreasing momentum transfer, the description of strong phase transitions with perturbative methods fails. Therefore, only a numerical solution of the QCD Lagrangian can be calculated on a discretized space-time grid, see e.g. [15]. This so-called lattice QCD provides the possibility to predict phase transitions, as long as the baryochemical potential is small.

On the left side of Figure 2.3, a lattice QCD calculation for the energy density as a function of the temperature is shown. Three cases are treated. While in the '3-flavour' case, the three quark flavours *up*, *down* and *strange* are considered, in the '2-flavour' case only two quark flavour, *up* and *down*, enter. In both cases, the quarks of the different flavours have equal masses. In the '2+1 flavour' case, quarks of the lightest two flavours, *up* and *down*, have equal masses, while the *strange* quark has a larger mass. At the critical temperature T_c a fast rise of the energy density with increasing temperature is calculated for all three cases, followed by a plateau. This gives evidence for a change of the thermal characteristics of the system. The blue arrow indicates the Stefan-Boltzmann limit.

On the right side of Figure 2.3, the QCD phase diagram is shown. The points indicate results of thermal fits at SPS energies. The magenta lines show the freeze-out curve for constant energy density and energy density. The blue lines show results for the phase boundary from lattice QCD

---

[3] The order of a phase transition is given by discontinuity in the lowest derivative of the free energy, i.e. first order phase transitions are discontinuous in the first derivative of the free energy.

[4] A critical point is characterised by the absence of a phase boundary, i.e. the coexistence of different phases at the same phase space coordinate.

calculations, which holds, as mentioned before, only for the case of small or vanishing baryochemical potential. The results from the thermal fits are well described by the calculations from lattice QCD [17] for $\mu_B < 0.4$ GeV. Beyond this value it is an open question, whether new exotic phases influence the chemical freeze-out or whether the calculations trace the QCD phase boundary.

2.2. Signatures of a hot and dense medium

The short time scale of a heavy-ion collision makes it impossible to access medium effects directly by an experiment. However, in the time evolution of a heavy-ion collision, the medium undergoes several stages, which result in a measurable impact on observables. Thereby, results from alternative collision systems can serve as reference.

To quantify modifications caused by the medium in heavy-ion collisions, measurements in pp collisions serve as a reference for a medium-free environment. The analysis of proton-nucleus (p–A) collisions allows to disentangle cold nuclear matter effects, such as gluon shadowing or anti-shadowing[5], from hot and dense medium matter effects. In the following section, experimental signatures of medium induced effects will be discussed.

Suppression of charged particle production

The direct comparison of observables measured in pp collisions and in heavy-ion collisions could indicate medium induced effects. A difference between spectra in heavy-ion collisions and in pp collisions scaled by the number of binary collisions can be interpreted as medium effects.

This can be quantified by the nuclear modification factor R_{AA}, which is, in general, calculated by

$$R_{\mathrm{AA}} = \frac{N^{\mathrm{AA}}}{\langle N_{\mathrm{binary}} \rangle \times N^{\mathrm{pp}}}, \tag{2.4}$$

where N^{AA} and N^{pp} are the yields of particles in AA and in pp collisions, respectively. The quantity $\langle N_{\mathrm{binary}} \rangle$ is the mean number of binary nucleon-nucleon collisions, calculated from the inelastic pp cross section and the nuclear overlap function [18]. If no medium effects would be present, the nuclear modification factor would be equal to unity.

The nuclear modification factor R_{AA} can be expressed as a function of transverse momentum p_{T} and normalised to the pseudorapidity window $\mathrm{d}\eta$ of the measurement. In that way, Eq. 2.4 can then be re-written in a more specific way:

$$R_{\mathrm{AA}}(p_{\mathrm{T}}) = \frac{(1/N_{\mathrm{evt}}^{\mathrm{AA}})\mathrm{d}^2 N_{\mathrm{ch}}^{\mathrm{AA}}/\mathrm{d}p_{\mathrm{T}}\mathrm{d}\eta}{\langle N_{\mathrm{binary}} \rangle (1/N_{\mathrm{evt}}^{\mathrm{pp}})\mathrm{d}^2 N_{\mathrm{ch}}^{\mathrm{pp}}/\mathrm{d}p_{\mathrm{T}}\mathrm{d}\eta}. \tag{2.5}$$

---

[5] In deeply inelastic processes, at low Bjorken-x, gluons can fuse and merge to a single gluon due to overlapping nuclear wave functions. This leads to a depletion of the very low-x region and to an excess of the slightly higher x region, which is called shadowing or anti-shadowing, respectively.

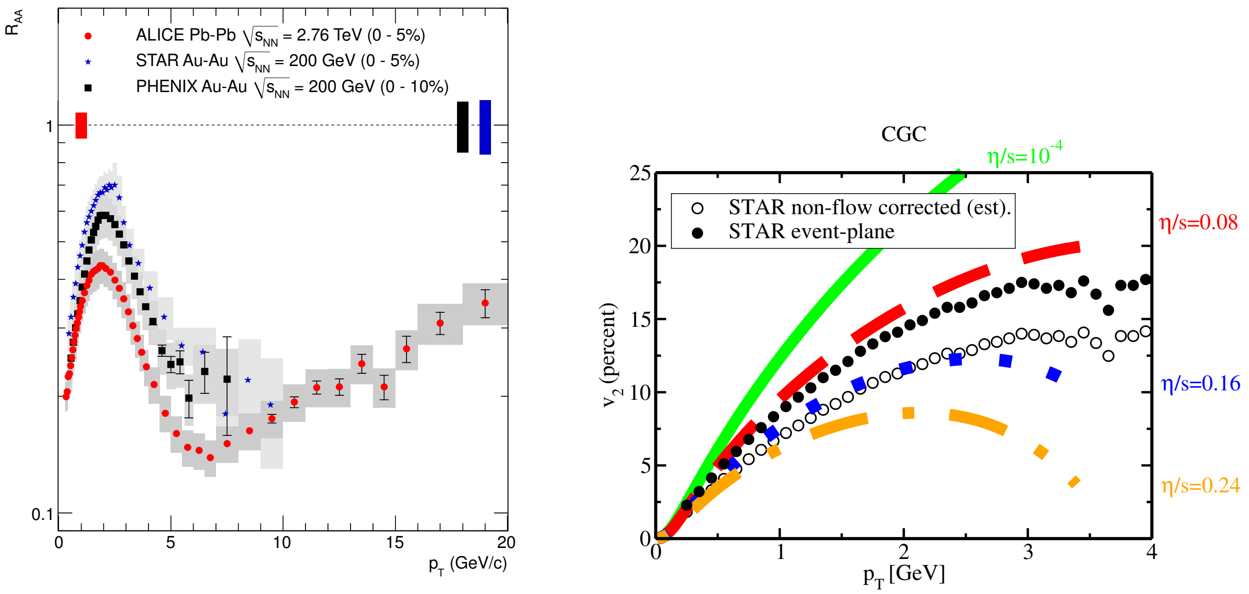

Figure 2.4.: Left: The nuclear modification factor R_{AA} is shown as a function of p_{T} for central collisions at different energies. The larger suppression at the higher collision energy at the LHC indicates the interaction of partons with a denser medium compared to RHIC. From [19]. Right: The elliptic flow v_2 as a function of the transverse momentum p_{T} measured by the STAR Collaboration [23] compared to hydrodynamical calculations for different values of η/s. From [24].

On the left side of Figure 2.4, a comparison of the nuclear modification factor R_{AA} as a function of transverse momentum is shown for central[6] collisions. The results from ALICE [19] at $\sqrt{s_{\mathrm{NN}}} = 2.76$ TeV are compared to results from the experiments STAR [20] and PHENIX [21] at a collision energy of $\sqrt{s_{\mathrm{NN}}} = 0.2$ TeV. Even though the pp reference spectra are depending on the collision energy [22] and are thus harder at the LHC compared to RHIC, the suppression measured by ALICE is stronger than for the RHIC experiments. This indicates a denser medium produced at the LHC compared to RHIC.

Elliptic flow

After a heavy-ion collision, the energy density and temperature of the produced medium undergoes an evolution. The system thermalises and forms a QGP, which collectively expands, cools down and subsequently hadronises. After the so-called kinetic freeze-out, transverse momentum spectra are fixed and particle trajectories are measured with the detector. The collective expansion is also called flow.

For semi-central heavy-ion collisions, the elliptic shape of the initial overlap region results in an anisotropic pressure gradient in the medium and leads to an asymmetric collective expansion.

It was proposed earlier [25], that the evolution of this expansion should be treated hydrodynamically,

---

[6] The centrality of a heavy-ion collision is defined by the impact parameter, which is given by the distance between the centres of the two colliding nuclei. Central events have a small impact parameter, peripheral events have a large impact parameter.

since the behaviour of the hot and dense matter showed properties of a fluid. Relativistic fluids can be quantified by the ratio of the shear viscosity η over the entropy density s, and by using gauge gravity duality [26], it follows

$$\frac{\eta}{s} \geq \frac{1}{4\pi},$$

where the minimal value $\eta/s = 1/4\pi$ corresponds to a perfect fluid.

The asymmetric expansion of the medium in momentum space can be quantified via a Fourier decomposition and its coefficients

$$v_n(p_\mathrm{T}, y) = \langle \cos[n(\varphi - \Phi_\mathrm{RP})] \rangle,$$

where n is the order of the coefficient, y the rapidity, φ the azimuthal angle and Φ_RP the reaction plane angle. The reaction plane is spanned by the beam direction and the impact parameter of the collision. The angular brackets denote the average over all particles for a given p_T and y in all events for a given centrality. The second Fourier coefficient v_2 is called elliptic flow.

On the right side of Figure 2.4, results from the STAR Collaboration [27] for elliptic flow of charged particles are shown as a function of p_T. The result for the elliptic flow is reduced by 20 % to take into account non-flow effects, such as a correlated background [28]. The data are confronted with hydrodynamical calculations for different values of η/s. The initial spatial asymmetry is based on a Colour-Glass-Condensate scenario, see e.g. [29, 30].

The hydrodynamical calculations are in good agreement with data for $\eta/s \approx 0.16$, indicating, that the assumption of a fluid is valid. However, $\eta/s \approx 0.16$ is twice the value of a perfect fluid $\eta/s = 1/4\pi$.

Photon-jet momentum imbalance

While quarks and gluons from hard scatterings interact with colour-charged particles in the medium produced in heavy-ion collisions, electromagnetic probes, such as photons, do not interact strongly and leave the medium without final-state interactions. The parton energy loss is referred to as jet-quenching. The correlation of isolated photons and jets directly accesses the parton energy loss in the medium [32].

On the left side of Figure 2.5, the average ratio of the momentum of a jet with $p_\mathrm{T}^\mathrm{Jet} > 30$ GeV/c to the momentum of an isolated photon with $p_\mathrm{T}^\gamma > 60$ GeV/c is shown as a function of the number of participants for pp collisions at $\sqrt{s} = 7$ TeV and for Pb–Pb collisions at $\sqrt{s_\mathrm{NN}} = 2.76$ TeV. Data is compared to PYTHIA [33] (for pp collisions) and PYTHIA+HYDJET [34] (for Pb–Pb collisions) simulations. While the comparison between data and MC is in good agreement for pp collisions and peripheral Pb–Pb collisions, the most central Pb–Pb distribution show a significant difference, indicating the energy loss of the parton in the medium.

On the right side of Figure 2.5, the fraction of photons with an associated jet is shown. For more

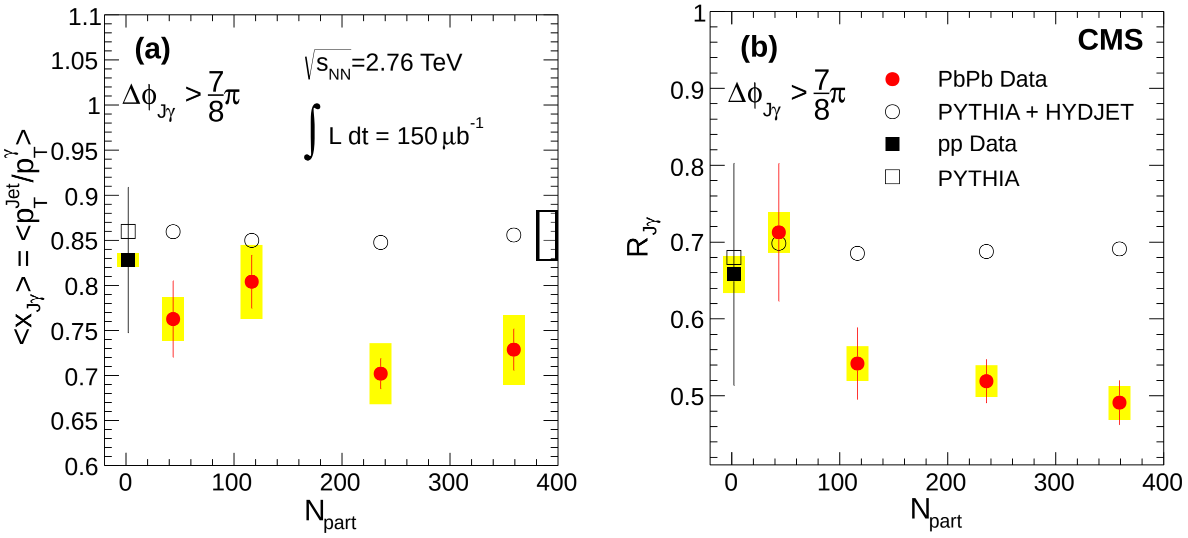

Figure 2.5.: Left: The average ratio between transverse momenta of a jet to an isolated photon as a function of the number of participants for pp collisions at $\sqrt{s} = 7$ TeV and Pb–Pb collisions at $\sqrt{s_{\mathrm{NN}}} = 2.76$ TeV measured by the CMS Collaboration. Right: The fraction of photons with an associated jet with $p_{\mathrm{T}}^{\mathrm{Jet}} > 30$ GeV/c. From [31].

central events, the fraction decreases since jets fall below the threshold $p_{\mathrm{T}}^{\mathrm{Jet}} > 30$ GeV/c due to partonic energy loss.

2.3. Role of dileptons

Dileptons are produced during the entire time evolution of a relativistic heavy-ion collision. Leptons are electromagnetic probes and do not couple to colour charges and, therefore, do not undergo any strong final-state interaction. In the following, this statement and its consequences is discussed.
The production of electromagnetic probes is suppressed, compared to hadronic probes, due to the different strength of the coupling constants. The production of direct photons is dominated by Compton scattering ($qg \rightarrow \gamma q$) and quark-antiquark annihilation ($q\bar{q} \rightarrow \gamma g$). The cross section for both processes scale by the factors $\alpha_{\mathrm{e.m.}} \times \alpha_{\mathrm{s}}$, where $\alpha_{\mathrm{e.m.}}$ and α_{s} are the coupling constants of the electromagnetic and of the strong interaction, respectively. Photons are suppressed by a factor ≈ 100 compared to hadronic processes, which scale in leading order with α_{s}^2. In Figure 2.6, the production processes of direct photons in leading order are shown.
It was pointed out in [35] that every source of real photons is also a source of virtual photons. Virtual photons convert internally into dileptons. Consequently, a quark-gluon Compton scattering $qg \rightarrow q\gamma$ has an associated process involving a virtual photon, which decays into a dielectron pair $qg \rightarrow q\gamma^* \rightarrow qe^+e^-$, i.e. this process is suppressed by another factor $\alpha_{\mathrm{e.m.}}$ compared to the process including a real photon. In contrast to real photons, virtual photons, i.e. dielectrons, have a mass. The relation between the photon yield and the invariant mass distribution of the dielectrons is

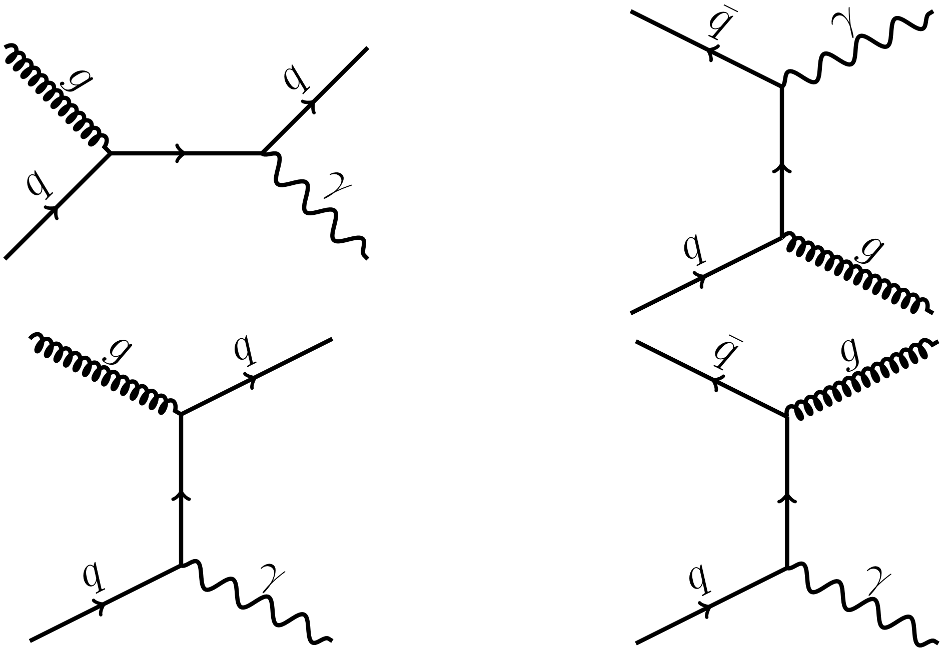

Figure 2.6.: Feynman diagrams for the dominant production mechanisms in pp collisions for direct photons. Left: Quark-Gluon Compton scattering. Right: Quark-Antiquark annihilation.

given by the Kroll-Wada equation [36]:

$$\frac{1}{N_\gamma}\frac{\mathrm{d}N_{ee}}{\mathrm{d}m_{ee}} = \frac{2\alpha_{\mathrm{e.m.}}}{3\pi}\sqrt{1-\frac{4m_e^2}{m_{ee}^2}}\left(1+\frac{2m_e^2}{m_{ee}^2}\right)\frac{1}{m_{ee}}\left|F(m_{ee}^2)\right|\left(1-\frac{m_{ee}^2}{m_{\mathrm{h}}^2}\right)^3, \tag{2.6}$$

where the number of photons N_γ is related to the mass-differential dielectron yield $\mathrm{d}N_{ee}/\mathrm{d}m_{ee}$ in terms of the electron mass $m_e = 0.511\ \mathrm{MeV}/c^2$, the electromagnetic coupling $\alpha_{\mathrm{e.m.}}$, the electromagnetic form factor $|F(m_{ee}^2)|$ and a phase space factor $(1-m_{ee}^2/m_{\mathrm{h}}^2)^3$. In a π^0 or η Dalitz decay, m_{h} is given by the hadron mass.

In the following, a brief estimation is given for the mean free path of an electromagnetic probe in the hot and dense QCD medium, created in a heavy-ion collision. After the production of a particle, it traverses the medium. The mean free path λ of a particle traversing a static medium with the particle density n and cross section σ is

$$\lambda = \frac{1}{n\sigma}. \tag{2.7}$$

In the relativistic limit ($p \gg m$) the scattering cross section can be calculated as

$$\sigma = N_{\mathrm{c}}Q_{\mathrm{f}}^2\frac{4\pi\alpha^2}{3s}, \tag{2.8}$$

where N_{c} is 1 for leptons and 3 for quarks, Q_{f}^2, α and s are the squared fermion electric charge, the

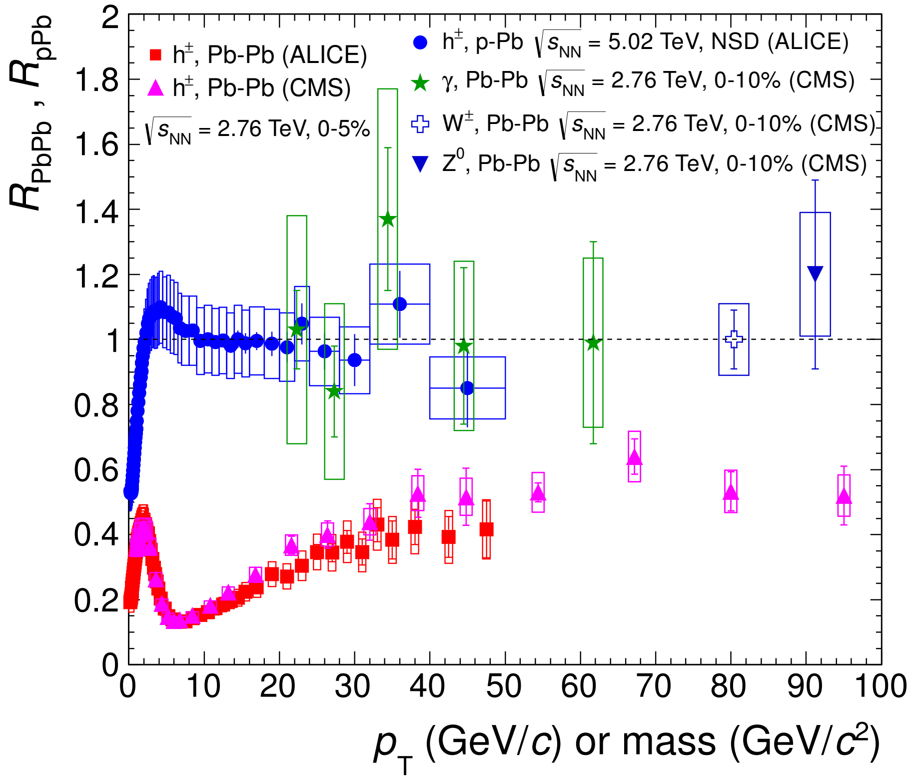

Figure 2.7.: The nuclear modification factors R_{AA} and R_{pA} are shown for a variety of different particle species. The difference in the suppression factor between strongly interacting particles (N_{ch}) and electromagnetically or electroweakly interacting particles ($\gamma, Z^0, W^{\pm}$) in Pb–Pb collisions is a striking evidence for the negligible final-state interaction of electromagnetic probes in the medium. From [37].

coupling constant of the interaction and the squared momentum transfer, respectively.

Given Eq. 2.1 and assuming $\alpha_{\mathrm{s}} \approx 0.3$, a ratio of the mean free path of a strongly interacting particle and an electromagnetically interacting particle is given by

$$\frac{\lambda_{\mathrm{s}}}{\lambda_{\mathrm{e.m.}}} \propto \left(\frac{\alpha_{\mathrm{e.m.}}}{\alpha_{\mathrm{s}}}\right)^2 \approx 10^{-4}. \tag{2.9}$$

Therefore, leptons can traverse on average a distance in the medium, which is about a factor 10^4 larger, than for strongly interacting particles, before they interact with any surrounding particle. Even in the dense medium created in a heavy-ion collision at LHC, the final-state interaction of a lepton is negligible.

In Figure 2.7, a compilation of nuclear modification factors for a variety of particles is shown for Pb–Pb collisions at $\sqrt{s_{\mathrm{NN}}} = 2.76$ TeV and p–Pb collisions at $\sqrt{s_{\mathrm{NN}}} = 5.02$ TeV. The difference in the suppression gives evidence for the different interaction with the strongly interacting medium. Hadronic probes, the majority of charged particles N_{ch}, show a strong suppression in the medium, while electromagnetic probes, such as photons γ, and electroweak probes, such as the gauge bosons $W^{\pm}$ and Z^0, show no significant suppression in heavy-ion collisions compared to pp collisions.

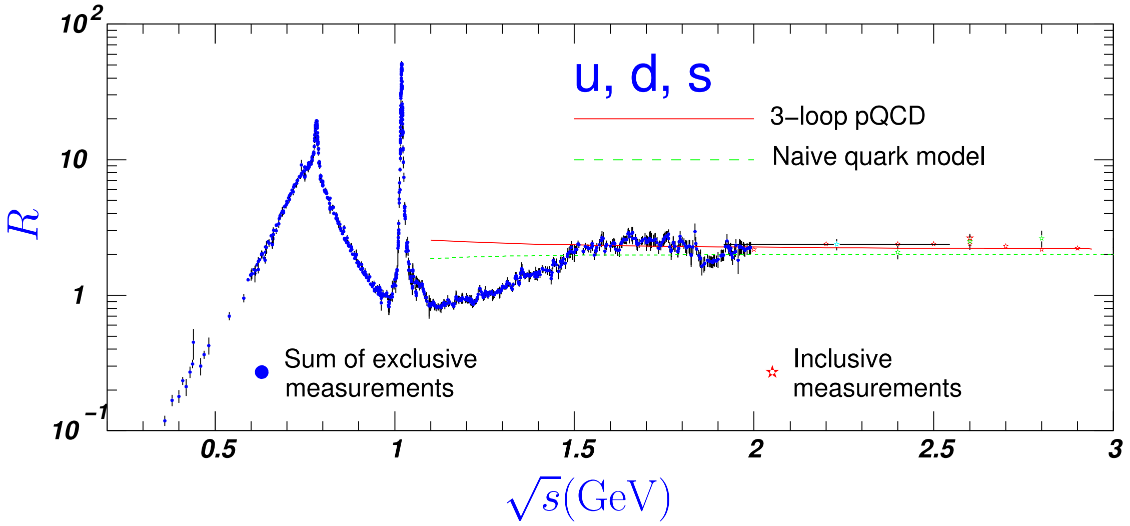

Figure 2.8.: The ratio between the hadronic and the dimuon cross section in e^+e^- annihilation as a function of the invariant mass. From [38].

To rule out other possible sources of suppression, a second reference measurement was performed by colliding protons with nuclei. The so-called R_{pA} demonstrates, that the suppression is due to the hot and dense medium and rules out initial and final-state effects due to the change of the nuclear parton distribution function for $p_{\mathrm{T}} \geq 2$ GeV/c.

As a consequence, dilepton yields are determined by their production rate and are not affected by final state effects. The production mechanisms depend on the collision system.

In general, the dilepton mass spectrum $\mathrm{d}N_{ll}/\mathrm{d}m_{ll}$ can be expressed by its integration over a realistic phase space volume

$$\frac{\mathrm{d}N_{ll}}{\mathrm{d}m_{ll}} = \int \mathrm{d}^4x \frac{m_{ll}\mathrm{d}^3q}{q_0} \frac{\mathrm{d}N_{ll}}{\mathrm{d}^4x\mathrm{d}^4q}, \tag{2.10}$$

where the energy of the dilepton $q_0 = \sqrt{m_{ll}^2 + q^2}$ is given by its invariant mass m_{ll} and its momentum q. In the case of heavy-ion collisions, the local emission rate contains a thermal contribution from the medium and a non-thermal contributions from the vacuum.

The vacuum (non-thermal) emission rate as function of the collision energy $\sqrt{s}$ can be expressed by the electromagnetic spectral function Im $\Pi^{\mathrm{vac}}_{\mathrm{e.m.}}$,

$$R = -\frac{12\pi}{s} \times \mathrm{Im}\ \Pi^{\mathrm{vac}}_{\mathrm{e.m.}}(s) \tag{2.11}$$

and is known from e^+e^- annihilation as ratio of the hadron production cross section to the dimuon production cross section:

$$R = \frac{\sigma(e^+e^- \to \text{hadrons})}{\sigma(e^+e^- \to \mu^+\mu^-)}. \tag{2.12}$$

Measurements of R are shown in Figure 2.8 as a function of $\sqrt{s}$. The invariant mass spectrum below ≈ 1 GeV/c^2 shows resonant structures and is well described by the Vector meson Dominance Model (VDM), see e.g. [39], which assumes that a vector meson, which carries the same quantum numbers as a photon, can fluctuate into a virtual photon state, where it can internally decay into a dilepton. The Feynman diagram is shown in Figure 2.9 for the case of a pion annihilation.

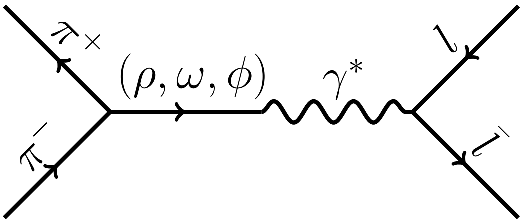

Figure 2.9.: A Feynman diagram indicating VDM in a pion annihilation.

The thermal dilepton emission rate per phase space unit can be written as

$$\frac{\mathrm{d}N_{ll}}{\mathrm{d}^4x\mathrm{d}^4q} = -\frac{\alpha^2_{\text{e.m.}}}{\pi^3 m^2_{ll}} L(m_{ll}) f^{\mathrm{B}}(q_0; T) \times \text{Im}\, \Pi^{\text{med}}_{\text{e.m.}}(m_{ll}, q; \mu_{\mathrm{B}}, T), \tag{2.13}$$

where m_{ll}, $L(m_{ll})$, $f^{\mathrm{B}}(q_0; T)$ and Im $\Pi^{\text{med}}_{\text{e.m.}}(m_{ll}, q; \mu_{\mathrm{B}}, T)$ are the invariant mass of the dilepton, a lepton phase-space factor, a thermal Bose distribution[7] and the in-medium electromagnetic spectral function, respectively.

The special character of dileptons arises from the separate dependence of the in-medium electromagnetic spectral function Im $\Pi^{\text{med}}_{\text{e.m.}}$ on the invariant mass and the momentum. The dilepton momentum q reflects mainly the kinematics of the medium and is sensitive to its expansion velocity of the medium and, therefore, can suffer from e.g. blue shifts. The invariant mass m_{ll} provides additional information. The invariant mass is invariant under Lorentz transformation and is therewith insensitive to the expansion of the medium, but it is sensitive to microscopic changes of the medium, e.g. changes of the degrees of freedom or chiral symmetry restoration [40].

As mentioned earlier, dileptons are emitted during the entire collision evolution. In that way, they reflect all phases, such as the initial hard parton scattering, the phase transition around T_c, and the decays after hadronisation. This is an essential reason for the richness of dilepton physics. The expected dielectron yield as a function of the invariant mass is sketched in Figure 2.10 and it demonstrates the variety of sources. Moreover, the different particle contributions of the dilepton mass spectrum reflect different phases of the medium properties.

---

[7] Indistinguishable particles with integer spin do not obey the Pauli exclusion principle. Therewith, one quantum state can be occupied by bosons several times.

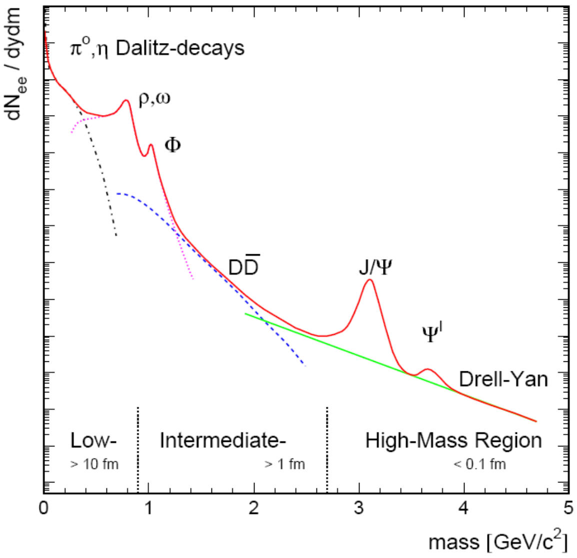

Figure 2.10.: An illustration of the expected contributions to the dielectron invariant mass spectrum. The various sources reflect the evolution of the medium in a heavy-ion collision. From [41].

In the following, the contributions to the low-mass dielectron yield will be briefly discussed.

Low-mass region The dominant source of low-mass dielectrons are Dalitz decays of the neutral pseudo scalar mesons π^0 and, to a smaller extent, the η and η' mesons. Dalitz decays are three body decays $X \rightarrow e^+e^-Y$, where Y can be a photon, as in the case of π^0, η, η' or a particle with finite mass, as in the case of $\omega \rightarrow e^+e^-\pi^0$.

At masses above 0.5 GeV/c^2, the vector mesons ω, ϕ and ρ contribute, which decay in a resonant channel $X \rightarrow e^+e^-$. It should be noted, that the spectral function of vector mesons plays an important role for the investigation of medium effects. In the later collision stages, the main constituents are pions and kaons. As shown in Figure 2.9 and according to the VDM, dilepton production is dynamically enhanced by pion annihilation. Moreover, the mass of a dilepton pair reflects the mass of a vector meson at its production. So medium modification of vector mesons, e.g. a broadening [40, 41] or a mass shift [42], would affect directly the dielectron mass spectrum and would have an impact on the measured spectrum. At the high collision energies at the LHC, already at $m_{ee} \approx 0.4$ GeV/c^2 the contribution of electrons from open charm hadrons is non-negligible. This contribution dominates the intermediate mass region.

Intermediate mass region At intermediate masses $1 \lesssim m_{ee} \lesssim 3$ GeV/c^2, decays of heavier quark flavours, charm and beauty, dominate the dielectron mass continuum. Quark-antiquark pairs, $c\bar{c}$ and $b\bar{b}$ pairs, are produced in hard partonic processes. The charm and beauty quarks form mainly D and B mesons, respectively, which can then decay semi-leptonically,

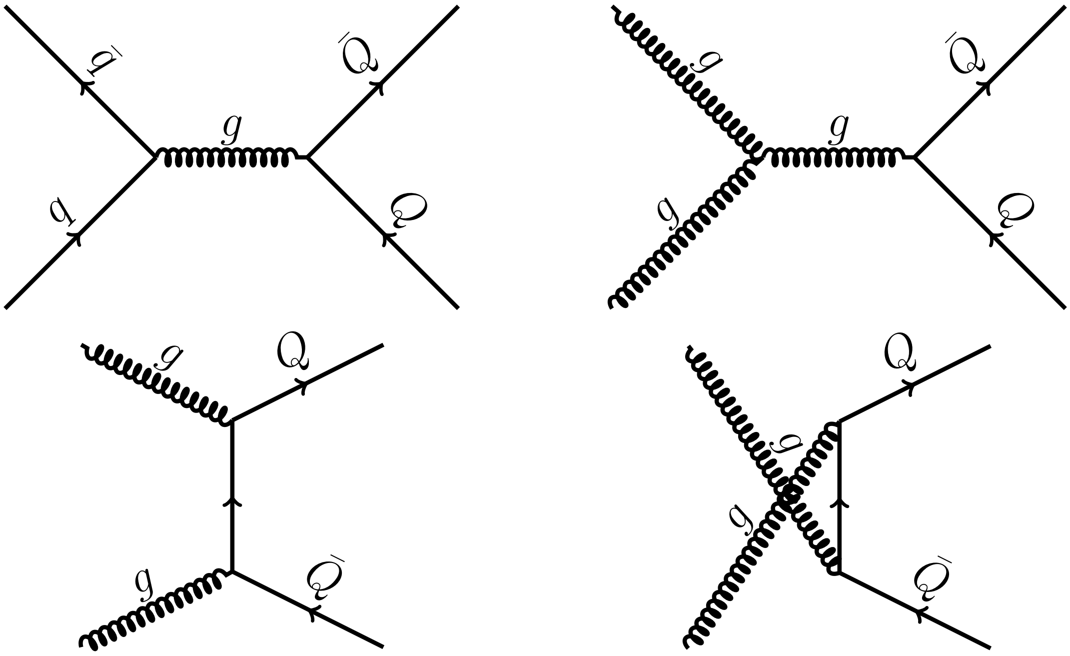

Figure 2.11.: Leading-order production processes of heavy quarks.

e.g. $D \rightarrow e^{\pm} + X$. The dielectrons from open heavy-flavour mesons decays are correlated through flavour conservation.

It is a feature of dileptons, that not only the information from the single quark can be accessed, but also information of the heavy flavour pair production mechanism is accessible through angular correlations of the dielectron. Examples for the production mechanism of heavy-flavour pairs in LO is shown in Figure 2.11.

High-mass region The higher mass region is also dominated by charm and beauty contributions. In the semi-leptonic open heavy flavour continuum the beauty contribution exceeds the contribution from charm at $m_{ee} > 4$ GeV/c^2.

However, there are also heavy quarkonia produced. The charmonium ($c\bar{c}$) ground state, J/ψ, has a dielectron and a radiative decay channel, $J/\psi \rightarrow ee\gamma$. Since the mass of the charm quark is rather large, $m_c \approx 1.3$ GeV/c^2, charm quarks are produced only in initial hard scatterings of a collision. It was proposed in [43], that J/ψ is an excellent candidate to investigate the medium due to a Debye-like colour screening, which would lead to a suppression of the J/ψ production in the medium. However, in addition to this suppression, the J/ψ can be (re-)generated by charm and anticharm quarks which meet in the medium, which would enhance the production of J/ψ.

At higher masses $m_{ll} \geq 5$ GeV/c^2, the Drell-Yan process [44, 45], the annihilation of a quark-antiquark pair into a virtual photon with a following decay into a dielectron pair contributes significantly to the dielectron continuum.

Beauty and antibeauty quarks can form at $m_{ll} \approx 9.5$ GeV/c^2 the Υ meson, which has excited states, e.g. Υ' and Υ'', at higher masses.

A compilation of the expected hadronic sources, as mentioned above, is often referred to as the dielectron cocktail. It can be calculated under the knowledge of the hadronic cross section and the consideration of dielectron kinematics. The cocktail reflects the expected dielectron signal at the moment of the chemical freeze-out.

Possible modifications of the dielectron signal, induced by the medium, would lead to a deviation of the dielectron data from the hadronic cocktail. This will be discussed later in section 5.6.

2.4. Previous dilepton measurements

The measurement of dileptons is an experimental challenge. Not only that dileptons are rare probes, which need to be identified with a high purity, the extraction of the physics signal remains difficult.

The understanding of dielectron spectra in the absence of a medium is crucial for the understanding of the production in the medium. Therefore, reference measurements are essential for any experiment. These reference measurements usually depend also on the possibilities given by the accelerator, at which the experiments are located.

In the following chapter, dilepton measurements will be described at different energy scales, from the low-energy experiments at the heavy-ion synchrotron SIS[8] 18 at GSI, to the CERN Super-Proton-Synchrotron (SPS), to the Relativistic-Heavy-Ion-Collider (RHIC).

2.4.1. Low-energy frontier

In the mid-eighties of the last century, the DiLepton Spectrometer (DLS) started to take data with a two arm setup at the BEVALAC at LBNL. It was designed to measure the dilepton pair production in pp, p–A and A–A collisions. It could be shown, that while data from pp collisions agreed to the expected dielectron sources [46] in Ca–Ca collisions [47] at 1 AGeV the dielectron cross section was larger than expected and could not be described by theoretical calculations [47]. This puzzle was motivation to build the High Acceptance DiElectron Spectrometer (HADES) at GSI SIS 18 [48]. Results from HADES reproduced the DLS data and with new calculations from theory, data could be described [49]. HADES results also showed [50], that spectra from C–C collisions could be reproduced by the superposition of the spectra from $\frac{1}{2}(\mathrm{pp}+\mathrm{pn})$. This indicates, that no evidence for medium effects occurs at low collision energy in C–C collisions.

At CERN SPS, another dilepton program was established.

The CERES experiment was a dedicated experiment for the measurement of low-mass dielectron production in a pseudorapidity window of $2.1 \leq \eta \leq 2.6$. Electrons were identified by two Ring Imaging CHerenkov detectors (RICH). The final setup included a Time Projection Chamber (TPC) for an improved momentum and mass resolution. Moreover, the energy loss information in the TPC was used for hadron identification. The lower cut-off in transverse momentum was $p_{\mathrm{T}} \geq 0.2$ GeV/c.

---

[8] German: SchwerIonen-Synchrotron

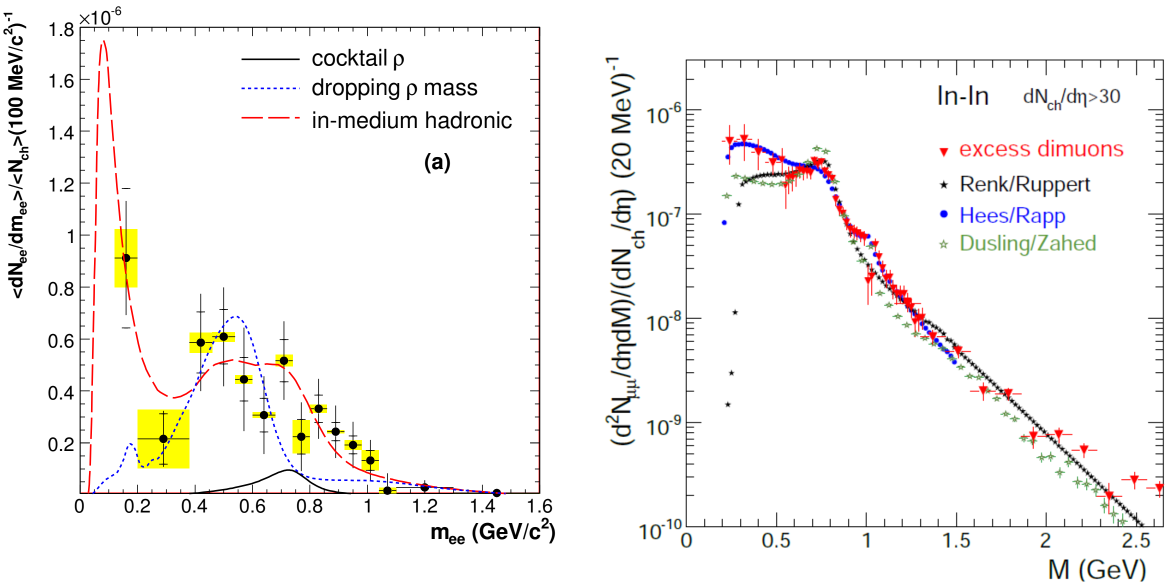

Figure 2.12.: Left: remaining dielectron yield after subtraction of cocktail except ρ meson for Pb–Au collisions at 158 AGeV. Data is compared to expected ρ contributions from cocktail, from dropping mass scenario [42] and from in-medium hadronic modification [41]. From [51]. Right: ρ spectral function for In–In collisions at 158 AGeV after absolute normalization. Data is in agreement to theoretical models [52, 53, 54]. From [55]

CERES results [51] for Pb–Au collisions at 158 AGeV favoured an in-medium broadening of the ρ meson spectral function [52]. The reference measurements were performed in p–Be collisions, which are a reasonable approximation of a medium-free collision system.

The NA60 experiment at SPS was an experiment dedicated to dimuon measurements. It combined the NA50 muon spectrometer with a high resolution silicon pixel detector. Due to the dimuon trigger and the fast read out, the statistical accuracy could be increased by a factor 1000 compared to CERES. The strong magnetic field of 2.5 T allowed a high precision measurement in momentum and mass and, moreover, bended soft muons in the spectrometer acceptance. NA60 results also show a strong broadening of the ρ mass shape in the medium compared to the expected shape and yield of the vacuum ρ spectral function [56].

In Figure 2.12, results from the SPS experiments CERES and NA60 are shown. The expected hadronic sources, excluding the ρ meson, are subtracted from the data, such that the remaining mass spectra are expected to be from the ρ meson. It is compared in both cases with different model calculations, and in the left panel to the vacuum ρ spectral function. In both cases, the vacuum spectral function of the ρ meson fails to describe data. Moreover, the broadening scenario [52] could be favoured against the 'dropping mass' scenario [42].

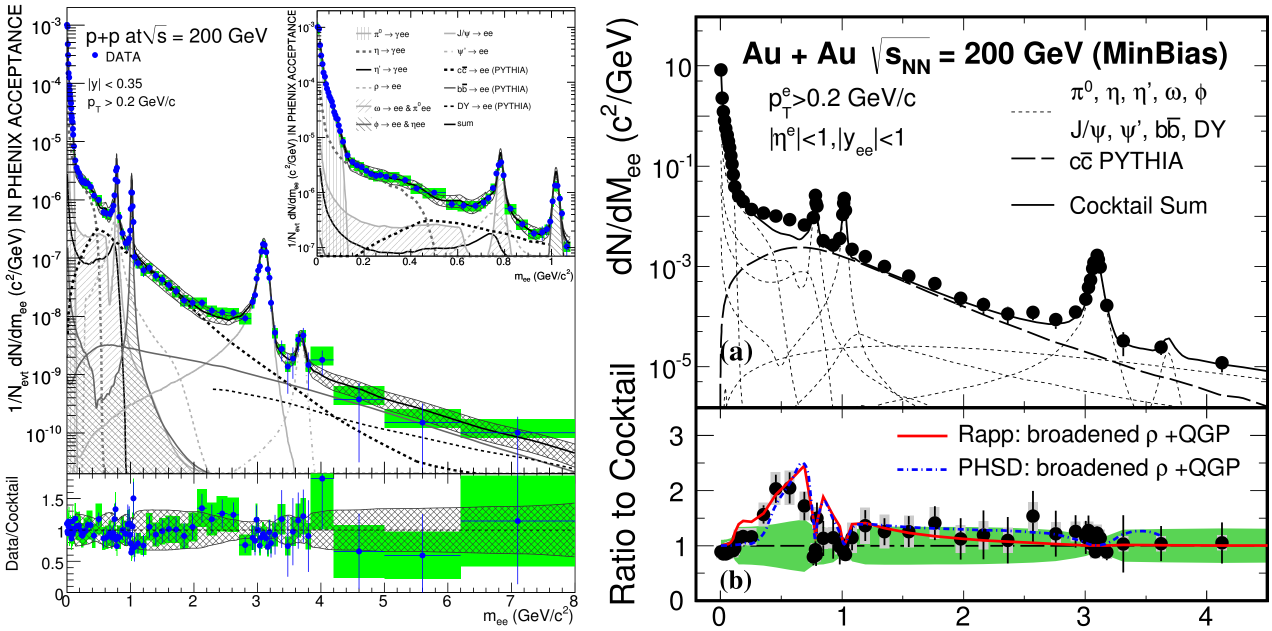

Figure 2.13.: Left: The dielectron invariant mass spectrum from pp collisions at $\sqrt{s} = 0.2$ TeV measured by the PHENIX Collaboration compared to the cocktail in the upper panel and as a ratio in the lower panel. The agreement between data and cocktail is excellent. From [57]. Right panel: The dielectron invariant mass spectrum from Au–Au collisions at $\sqrt{s_{\mathrm{NN}}} = 0.2$ TeV measured by the STAR Collaboration compared to the hadronic cocktail simulation. The lower panel shows the ratio between the data and the cocktail, which shows a significant enhancement for $0.4 < m_{ee} < 0.7$ GeV$/c^2$. The inserted lines show model calculations for the medium modification, which agree to the measured enhancement. From [58].

2.4.2. RHIC energies

Additionally to the stimulating results of the SPS dilepton program, at RHIC the experiment PHENIX was designed with emphasis on the measurement of electromagnetic probes. RHIC collides Au nuclei up to a centre-of-mass energy of $\sqrt{s_{\mathrm{NN}}} = 0.2$ TeV, but is also capable to accelerate U or Cu nuclei. As reference measurements, RHIC delivers pp or d–Au collisions.

For electron identification, PHENIX combines a Cherenkov detector with an electromagnetic calorimeter in the two central arm detectors, covering each $\pi/2$ in the azimuth and $|\eta| < 0.35$ in pseudorapidity. A mass resolution of $\Delta m_{ee}/m_{ee} \approx 1$ % at $m_{ee} \approx 1$ GeV$/c^2$ is reached.

In 2010, a Time-Of-Flight detector was added to the STAR detector at RHIC [59], providing the possibility to identify electrons with a high purity. STAR is performing its electron identification with a large TPC and additionally combining this information with the TOF measurement for $|\eta| < 1$.

The reference measurements performed in pp collisions showed an agreement between data and the expected dielectrons sources from hadronic decays in both experiments [57, 60], see left panel of Figure 2.13 for the case of PHENIX data.

In Au–Au collisions an excess over the expected sources in the mass region $0.2 < m_{ee} < 0.7$ GeV$/c^2$

was observed in both experiments [58, 61], while the rest of the mass continuum showed a good agreement, see right panel of Figure 2.13 for the case of STAR.

However, for Au–Au collisions the results from PHENIX and STAR show a discrepancy in the excess region. Also the excess character seems different. While the PHENIX results indicate a strong centrality dependence, the STAR results do not reproduce this behaviour.

In contrast to former SPS or STAR measurements, the excess observed by PHENIX can not be described by existing theoretical calculations, see e.g. [62]. More recently the beam energy scan at RHIC lead to new results. STAR measured the dielectron production in Au–Au collisions at beam energies from $0.02 < \sqrt{s_{\mathrm{NN}}} < 0.2$ TeV and covers therefore collision energies down to energies delivered by SPS. The results for the different beam energy spectra are consistent with calculations from [52], see e.g. [63].

3. ALICE detector system

The Large Hadron Collider (LHC) [64] located at CERN near Geneva is designed to accelerate and collide proton beams up to a centre of mass energy of $\sqrt{s} = 14$ TeV and Pb ions up to $\sqrt{s_{\mathrm{NN}}}$ = 5.5 TeV. The four main experiments at the LHC are ALICE [65], ATLAS [66], CMS [67], and LHCb [68].

ALICE (A Large Ion Collider Experiment) is designed for the study of heavy-ion collisions to investigate strongly interacting matter under extreme conditions. The ALICE detector setup [69, 70] is optimised to be operated in high particle density environments. A schematic view of the ALICE detector with its sub-detector systems is shown in Figure 3.1.

In total, the detector volume is ($16 \times 16 \times 26$ m^3) and ALICE has a mass of 10.000 t. It can be subdivided into two main components: the central barrel ($|\eta| < 0.9$) for the study of hadron, electron and photon signatures and the forward muon spectrometer ($-4 < \eta < -2.5$) for the measurement of muons from decays of quarkonia and semi-leptonic heavy-flavour hadrons.

The global coordinate system of the ALICE detector is a right-handed Cartesian coordinate system with its origin at the nominal collision point ($x = 0, y = 0, z = 0$). The z axis is aligned along the beam axis, where the A side is at $z > 0$ and C side is at $z < 0$. Due to the cylindrical shape of the detector, additionally, one can use cylindrical coordinates with the azimuthal angle increasing from $\varphi = 0$ from the x axis passing the y axis ($\varphi = \pi/2$) to the x axis at 2π with the observer at negative z looking towards the interaction point.

In the following chapter, the different sub-systems are described. It focuses on the detectors used for the dielectron analysis. In section 3.1 the detector systems in the central barrel are described. In section 3.2 the forward rapidity muon spectrometer will be briefly discussed. Moreover, the online infrastructure built up for taking and storing data is described in section 3.3. Finally, section 3.4 gives an overview of data processing from raw data to the data used for physics analysis.

3.1. Central barrel

The central barrel detectors are mounted within a solenoid magnet, reused from the Large-Electron-Positron Collider experiment L3, which has an internal length of 12 m and a diameter of 10 m. Along the beam axis it produces a nominal magnetic field of 0.5 T. With the ALICE central barrel detectors, particles can be reconstructed over the transverse momentum range $0.1 \lesssim p_{\mathrm{T}} \lesssim 100$ GeV/c. Hadrons, electrons and photons can be identified in the pseudorapidity range $|\eta| \leq 0.8$ over the full azimuthal angle.

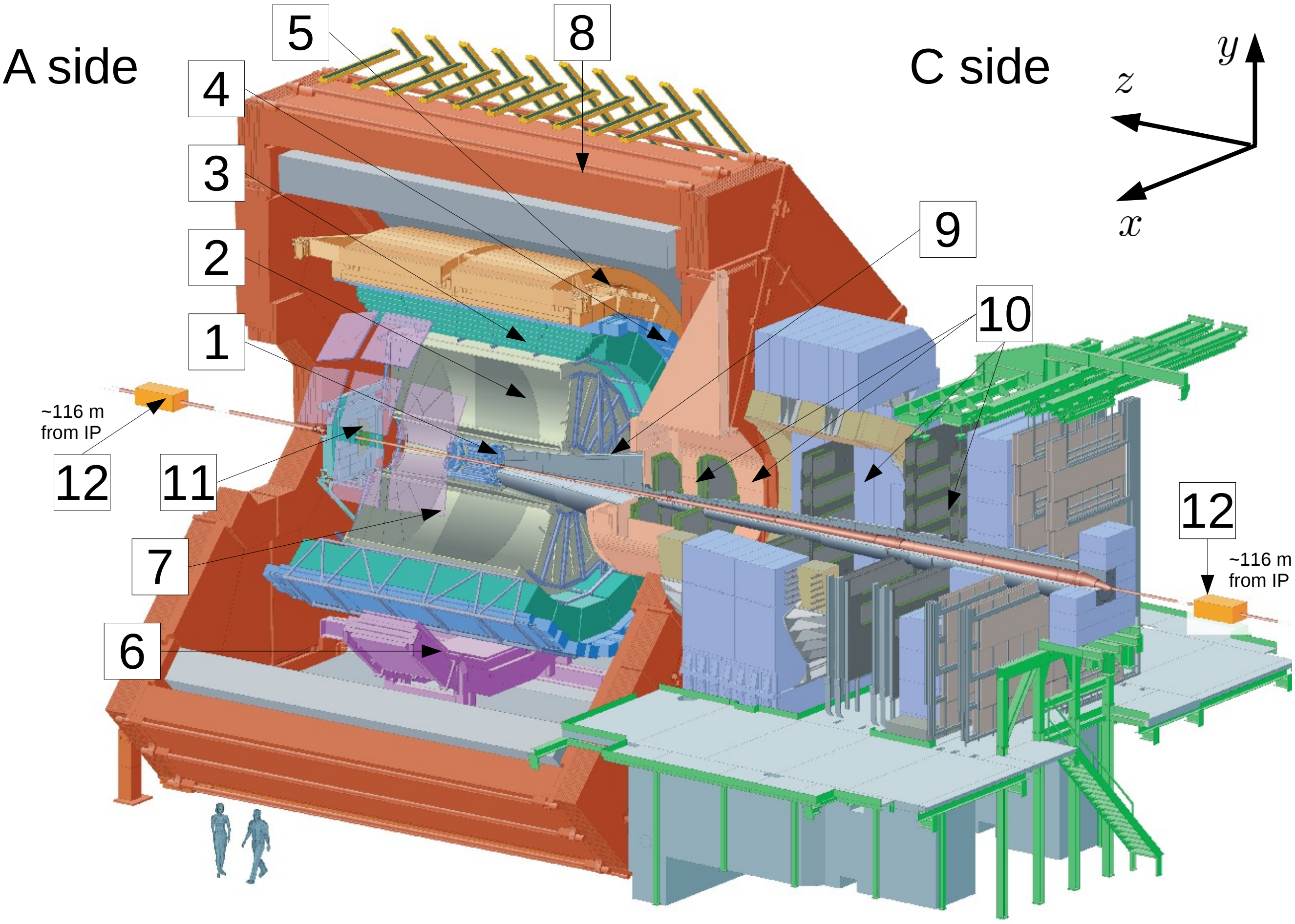

Figure 3.1.: The ALICE detector system. The detectors in the central barrel: The ITS $\boxed{1}$, the TPC $\boxed{2}$, the TRD $\boxed{3}$, the TOF $\boxed{4}$, the EMCal $\boxed{5}$, the PHOS $\boxed{6}$, and the HMPID $\boxed{7}$, surrounded by the L3 magnet $\boxed{8}$. In the forward direction the muon arm consisting of a hadron absorber $\boxed{9}$ and muon tracking chambers $\boxed{10}$. The PMD and VZERO are shown in $\boxed{11}$, and in $\boxed{12}$ the ZDC is indicated, which is located in a distance of about 116 m from the interaction point.

Inner Tracking System

The Inner Tracking System (ITS) [71] is a silicon based detector and is the detector closest to the beam interaction point. It consists of six coaxial sub-detectors with two layers each, Silicon Pixel Detector (SPD), Silicon Drift Detector (SDD), and Silicon Strip Detector (SSD), see Figure 3.2. The six sub-detectors are located in radial distances of $3.9, 7.6, 15, 24, 38$ and 43 cm from the beam axis and have an increasing length in the beam direction for the detectors with increasing radial distance.

Its main task is high precision vertexing, i.e. tracking towards the interaction point. The vertex resolution is about 60 μm and allows the determination of secondary vertices of weak decays.

The analogue read-out of the two outermost sub-systems, SDD and SSD, provides also particle identification down to $p_{\mathrm{T}} \approx 0.1$ GeV/c.

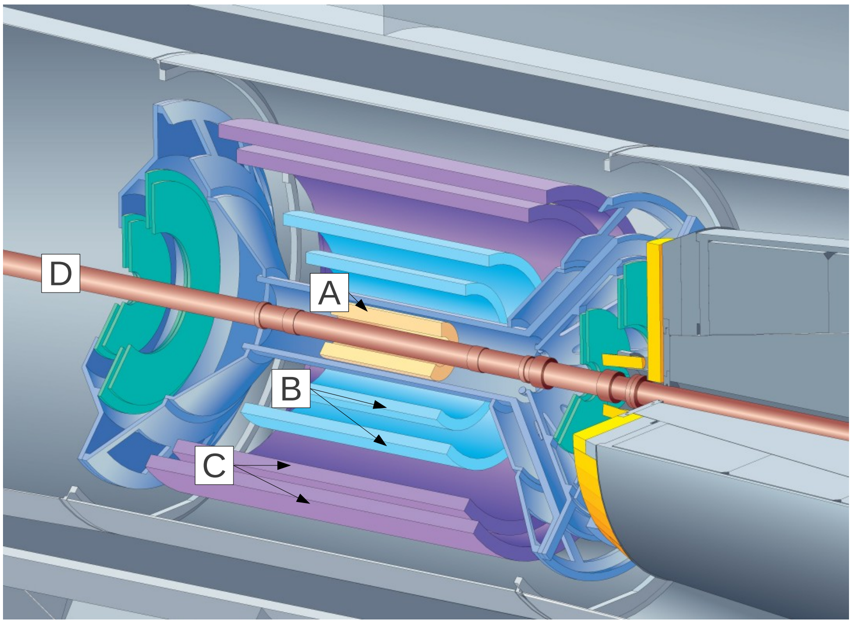

Figure 3.2.: The ITS with its six layers of sub-detectors. From inside to outside: Two layers of silicon pixel detectors (SPD, $\boxed{\text{A}}$), two layers of silicon drift detectors (SDD, $\boxed{\text{B}}$) and two layers of silicon strip detectors (SSD, $\boxed{\text{C}}$). The ITS is the closest detector surrounding the beam pipe $\boxed{\text{D}}$.

Time Projection Chamber

The Time Projection Chamber (TPC) [72, 73] is the main tracking and particle identification device in the ALICE detector system. It was built to detect and track the highest charged particle multiplicities predicted for Pb–Pb collisions at the LHC [65]. The TPC is a hollow cylinder with an inner radius of about 85 cm and an outer radius of 250 cm, where the symmetry axis is aligned along the beam axis. Its length along the beam axis is 500 cm. A schematic view is shown in Figure 3.3, left panel.

The volume is filled with a counting gas, which was chosen to be a mixture of Ne-CO_2-N_2 (85-10-5). An electric field is applied parallel to the beam axis from the outer electrodes to a central electrode, which subdivids the volume. Particles crossing the active volume ionise the counting gas and the freed electrons drift to the outer end plates of the cylinder, see e.g. [74] for more information. The arrival points are measured in two dimensions with Multi Wire Proportional Chambers (MWPC) [75].

The particle momentum can be determined from the curvature of the particle trajectory in the magnetic field. The energy loss information in combination with the particle momentum can be used for particle identification.

The design of the read-out planes of the TPC are optimised for a high-multiplicity environment. They consist of 18 trapezoidal sectors, each covering 20° in azimuth. On the right side of Figure 3.3 the cluster occupancy for a minimum-bias Pb–Pb collision at $\sqrt{s_{\mathrm{NN}}} = 2.76$ TeV is shown in local coordinates. The radial track or cluster density has a $1/r^2$ dependence, which suggests a radial segmentation of Inner Read-Out Chambers (IROCs) and two kinds of Outer Read-Out Chambers

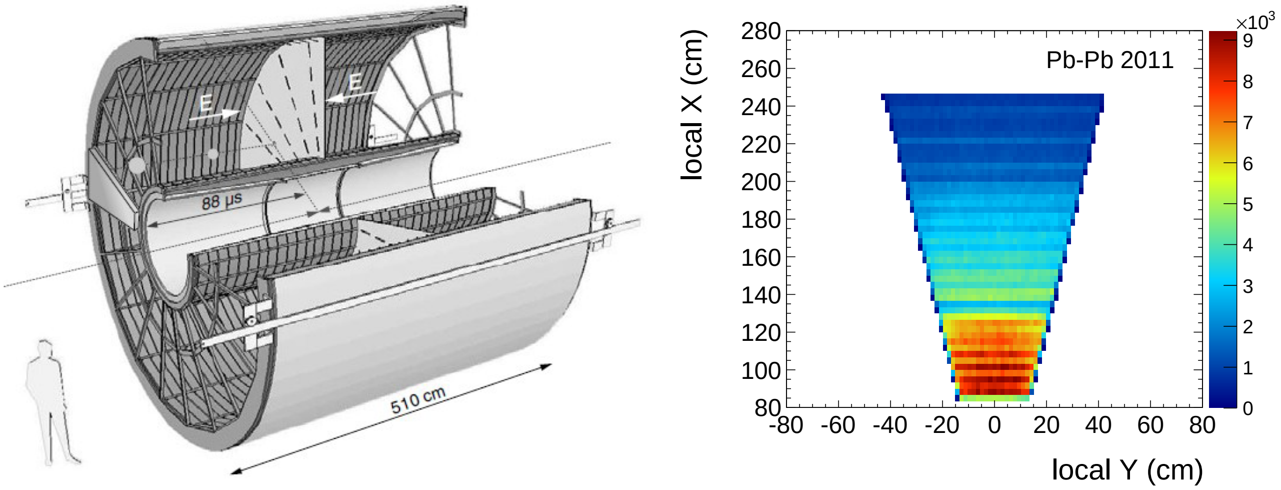

Figure 3.3.: Left: A schematic layout of the field cage of the TPC. The electric field direction is indicated by arrows.The average drift time and detector length are shown. From [72]. Right: A TPC sector in the local coordinate system. The colour code represents the pad-row occupancy of a minimum-bias Pb–Pb collision at $\sqrt{s_{\mathrm{NN}}} = 2.76$ TeV.

(OROCs), which is summarised in Table 3.1. The local coordinate system of the TPC is rotated in such way, that the local x coordinate is perpendicular to the sensitive plane of the detector, i.e. to the padrow.

The energy loss of a charged particle traversing the volume of the TPC is proportional to the amplified signal detected on the end cap plates. Local x and y coordinates are given by the detected position on the end plates and the z position can be calculated from the drift time of the secondary electrons.

chamber type	radial range (cm)	pad size (mm^2) $x \times y$
IROC	81.1 – 132.1	4×7.5
OROC	134.6 – 198.6	6×10
OROC	198.6 – 246.6	6×15

Table 3.1.: Pad sizes of a sector within the TPC.

Transition Radiation Detector

The Transition Radiation Detector (TRD) [76] is located in a radial distance of 3 m from the interaction point outside of the TPC. It consists of six layers, each consisting of a radiator and MWPC. Radiators have a large amount of boundaries between material with different dielectric constants. Charged particles with a Lorentz factor $\gamma > 1000$ produce energetic X-rays, so-called transition radiation, while traversing the radiators.

Since for the Lorentz-factor holds $\gamma \propto 1/m$, light particles produce a different signal than heavy particles at the same transverse momentum. The TRD can therewith be used for the separation of e.g. electrons and pions at higher transverse momenta, $p_{\mathrm{T}} \gtrsim 1$ GeV/c. Moreover, the TRD can deliver a hardware trigger for single electrons with $p_{\mathrm{T}} > 3$ GeV/c and for quarkonia with a single leg electron transverse momentum, $p_{\mathrm{T}} > 2$ GeV/c.

Time-Of-Flight detector

The Time-Of-Flight detector (TOF) [77] is used for the separation of pions, kaons, and protons up to a few GeV/c. It is located at a radial distance of 3.7 m to the interaction point and is segmented in 18 supermodules in azimuth surrounding the TRD. Each module consists of MRPC strips [78]. The time-of-flight measurement depends on the difference $t_{\mathrm{hit}} - t_0$, where t_{hit} is the time when a particle hits TOF detector and t_0 is the time of interaction. t_0 is measured by a dedicated detector (T0). In case T0 is not available in an event, t_0 can be determined from the collision time of bunches delivered by the LHC or statistically from the t_{hit} values of multiple particles themselves. The overall time resolution is given by $\sigma_{\mathrm{TOF}} = \sqrt{\sigma_{\mathrm{hit}}^2 + \sigma_0^2}$, which is about 120 ps for pp collisions.

Electromagnetic Calorimeter

The ElectroMagnetic Calorimeter (EMCal) [79] is located at mid-rapidity ($|\eta| \lesssim 0.7$) and covers an azimuthal range of $\Delta\varphi = 107$ °. It enhances the ALICE capabilities of jet, photon, electron and neutral meson (π^0, η...) measurements at high p_{T}. Together with the particle identification capabilities of the other ALICE detectors, photon-hadron correlation measurements become feasible, which were proposed as more differential probes of jet quenching [80].

Other detectors

The detectors described above all contribute to the measurement of electrons.
Other detectors, not directly related to electron analyses, will be described briefly in the following. The High Momentum Particle IDentification (HMPID) detector consists of an array of RICH detectors and can be used for the identification of charged hadrons in the transverse momentum range $1 < p_{\mathrm{T}} < 5$ GeV/c. The PHOton Spectrometer (PHOS) is an electromagnetic calorimeter comprising high-density $\mathrm{PbWO_4}$ crystals for the detection of electromagnetic showers. PHOS is located in a distance of 4.6 m from the collision vertex and covers the pseudorapidity of $|\eta| < 0.13$ and $\Delta\varphi = 60°$ in the azimuth.
At large pseudorapidities ($-3.4 < \eta < -1.7$ and $1.7 < \eta < 5.0$), the Forward Multiplicity Detector (FMD) extends the overall multiplicity measurement with 5 rings of silicon strip detectors. Another detector at large pseudorapidity is the Photon Multiplicity Detector (PMD), with which the multiplicity and the spatial distribution of photons can be measured on an event-by-event basis. The VZERO detectors, located asymmetrically at $z = -0.9$ m and $z = 3$ m from the interaction point, are dedicated for triggering and luminosity control and, moreover, to the measurement of the

event plane and collision centrality. The Zero Degree Calorimeters (ZDC) are located in a distance of 116 m in both directions of the interaction point. It consists of four calorimeter towers to detect spectator neutrons and protons to measure the centrality of a heavy-ion collision or, moreover, the luminosity.

3.2. Muon system

The forward muon spectrometer is located in the range $-4.0 < \eta < -2.4$ and is designed to measure single muons and dimuons from decays of low-mass vector mesons, open heavy flavour hadrons and quarkonia.

Close to the interaction point, an absorber absorbs hadrons and reduces the background from muons originating from light hadrons. The muon spectrometer composes of five tracking stations, each consisting of two cathode pad/strip chamber. The trigger system is designed to trigger one or two individual muons with four RPCs in two stations. The dipole magnet is located in a distance of 7 m from the nominal collision vertex and produces an integrated magnetic field of 3 Tm.

3.3. Data taking model

During data taking, the experiment is controlled via the Experiment Control System (ECS), which is incorporating the four online systems [81] in ALICE and the detectors:

DCS The Detector Control System (DCS) controls the sub-detectors and provides monitoring of the sub-system equipment to ensure reliable operation.

CTP For the selection of physics events of specific interest, one can characterise events by their observables. The Central Trigger Processor (CTP) delivers the trigger decision based on a pattern recognition in trigger sub-detectors and sends this read-out decision to all detectors. There are different trigger levels depending on the trigger complexity or duration of the trigger decision

- **L0** The Level 0 trigger (L0) is a fast trigger with a latency of 1.2 μs.
- **L1** Level 1 trigger (L1) is a more advanced trigger and has therefore a longer latency of ≈ 6.5 μs. If L1 rejects (L1r), the event is discarded. Otherwise the event is accepted (L1a).
- **L2** The last trigger stage, Level 2 trigger (L2), is dispatched after the TPC drift time of about 90 μs. This assures that the complete event can be read out in case, that L2 accepts the event (L2a). Moreover, it allows for pile-up rejection by the past-future protection.

DAQ In case, that L2 accepts the event, the event is sent from the data buffer in the Front-End Electronics (FEE) to the Data AcQuisition System (DAQ) using optical Detector Data Links (DDLs). The DAQ structure contains the following levels:

LDC The Local Data Collectors (LDCs) build sub-event fragments and sends them to the second level.

GDC The Global Data Collectors (GDCs) assemble the fragments to a complete event structure on a computer farm. Additionally, GDCs provide online event monitoring.

Data Storage After event building, the data is sent to the permanent data storage for offline reconstruction.

HLT The High Level Trigger (HLT) is an online system and software filter to select interesting events and optimise the use of the available bandwidth. After the read-out and L2a, it runs in parallel to DAQ. The HLT has three main functions:

Triggering Filtering of events on the basis of the physics observables reconstructed online.

Compressing Reduction of the event size by lossy or lossless data compression to optimise the use of the available bandwidth.

Selecting Selection of Region of Interests (RoI) and storing only parts of single events of events read out.

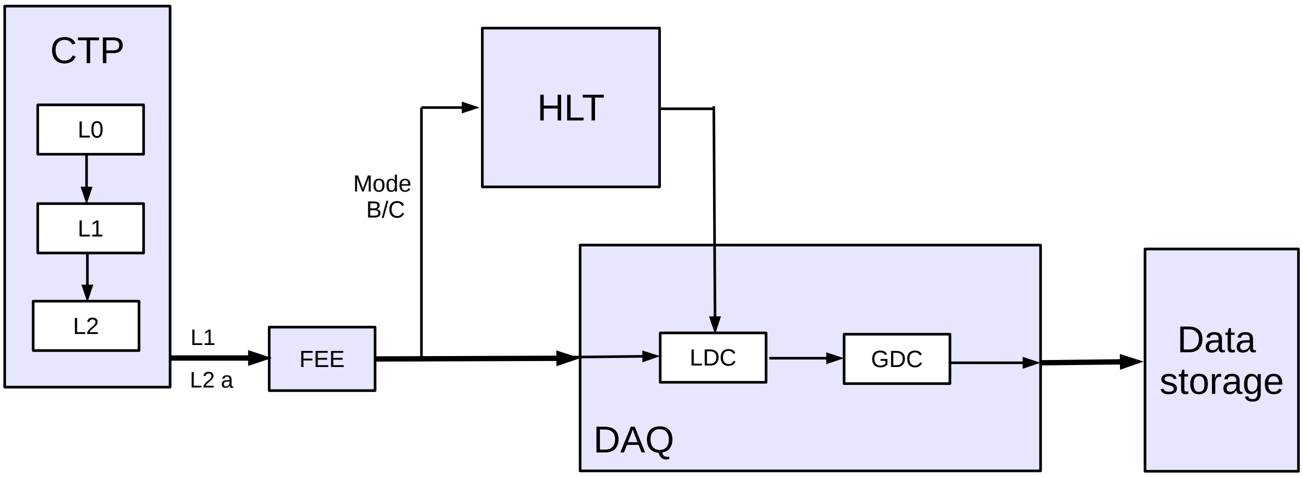

Figure 3.4.: A schematic picture of the online systems involved in the data taking. For details, see text.

A schematics of the data flow paths can be seen in Figure 3.4.

One distinguishes three running modes. In mode A, no data is sent to HLT and DAQ does not expect a decision from HLT. In mode B, data is sent to and processed by HLT. DAQ checks for the integrity of the HLT decision, but does not consider it. In mode C, data is sent to HLT. HLT processes the data and makes a decision. DAQ executes the decision of HLT.

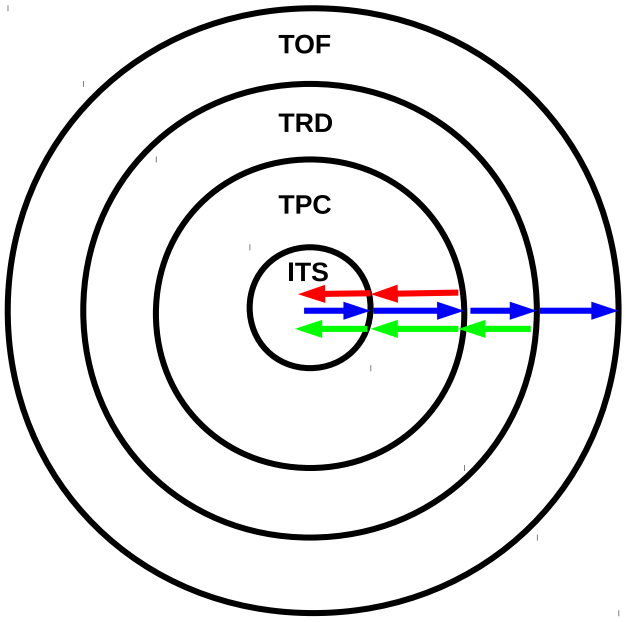

Figure 3.5.: Scheme of the offline global track reconstruction procedure. Every arrow indicates a reconstruction step. From [82]

3.4. Reconstruction

Charged particles crossing the sub-detectors produce analogue signals, i.e. their position in space, as a raw data format.

For the physics analysis of the data coming from the detectors, it is disadvantageous to use the raw data format. Many processes would be needed to be often repeated in the analysis for each physics analysis.

Therefore, tracks are reconstructed in every event together with the corresponding systematic uncertainties. A track is a trajectory along assigned space-time points, so-called clusters. The track reconstruction is based on a Kalman filter [83] with detector specific implementations and is performed in three steps, see Figure 3.5.

Prior to the track-finding, the vertex is localised based on SPD-only information to constrain the tracks to this vertex already in the beginning. The first step in the tracking starts in the outermost part of the TPC, where the track density is the lowest compared to the regions closer to the interaction point. The track is prolonged through the TPC towards the inner part of the ITS to the first primary vertex estimate (red arrows). The second step proceeds from the innermost ITS through TPC and TRD to the TOF (blue arrows).

In the last step inwards the momentum information is updated and the track is fitted from the outermost detector to the primary vertex (green arrows).

4. Commissioning of the use of online cluster reconstruction in the TPC with the High-Level Trigger

During the Pb–Pb data taking in 2010, instantaneous peak luminosities around $\mathscr{L} \approx 30$ Hz/b were reached. It was measured, that a central Pb–Pb event can produce raw data up to the volume of ≈ 80 MB. For 2011 it was planned to increase the luminosity by about a factor of 15, such that for a central Pb–Pb collision trigger running at 200 Hz, data rates of up to 16 GB/s were expected. However, the DAQ was designed to cover a maximum band width of 4 GB/s. To guarantee a fully efficient data taking, the data taking volume needed to be reduced by about a factor 4.

Since the raw data of the TPC occupies a large fraction of the data volume, it was necessary to focus on the data reduction in the TPC. The reduction of the data volume, coming from the TPC was performed as follows:

online cluster reconstruction The cluster finding in the TPC was done online in the HLT. After the online reconstruction of the clusters, the data from the HLT was encoded using a lossless Huffman compression algorithm [84]. Preprocessed TPC clusters were sent to DAQ. Only a fraction of about 1 % of the raw data was stored.

offline track reconstruction The track reconstruction was performed offline, as it is described in section 3.4.

A schematic comparison between the two reconstruction procedures is shown in Figure 4.1. The upper data flow path shows the reconstruction scheme as it was before Pb–Pb data taking 2011. The recorded raw data from the TPC is directly sent to DAQ and the permanent data storage. Cluster Finder (CF) and track reconstruction are performed offline.

The lower data path shows the data flow after commissioning of the online cluster finding and online cluster reconstruction. The recorded raw data of the TPC is replaced by the data preprocessed in the HLT.

To assure the preservation of the physics information within the read out data independently of the cluster reconstruction algorithm, extensive quality assurance (QA) studies were carried out on MC level and on data level. The performance reached with the new reconstruction scheme was compared with one the from the previously established scheme.

The QA was done on two levels:

1. The comparison of the raw cluster properties between clusters reconstructed online and offline before tracking.

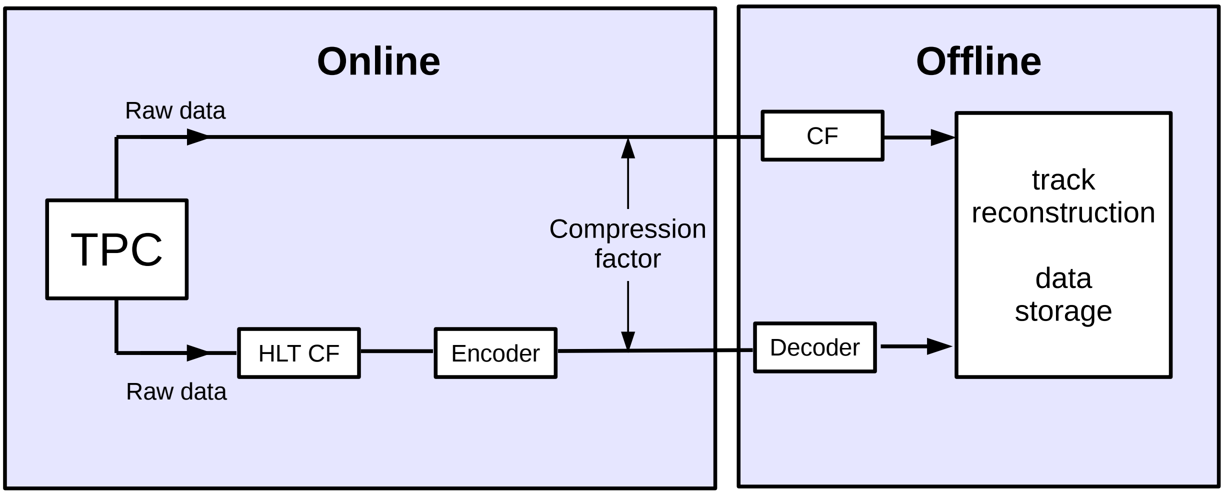

Figure 4.1.: Comparison between data flow with clusters reconstructed online in the HLT and clusters reconstructed offline. The upper data path shows the old reconstruction scheme with offline clusters, the lower data path the new reconstruction scheme with clusters reconstructed online in the HLT.

2. The comparison of tracks with clusters reconstructed online and offline in the TPC. The main focus was on the transverse momentum resolution at high momenta and the particle identification quality in the TPC.

The following chapter gives an overview of the studies carried out for the commissioning of the online cluster reconstruction algorithm for the Pb–Pb data taking in 2011. In section 4.1, the cluster fitting procedure for the online and offline reconstruction scheme is discussed. Moreover, comparisons of the cluster properties on cluster level are presented. Section 4.2 shows comparisons of track properties after the full reconstruction as it is used for physics analysis. In section 4.3 the results are summarised.

4.1. Online and Offline cluster finding

Before the actual track reconstruction, clusters need to be found and reconstructed in the TPC. Clusters are two-dimensional coordinates in a virtual padrow–time plane. There are essential differences between online and offline cluster finding, which is briefly described in the following.
Basis for the cluster finding is the charge distribution on the virtual padrow–time plane. The bin size in padrow dimension is given in Table 3.1. A time bin is given by the inverse of the frequency of 10 kHz, which corresponds to 100 ns. The cluster finding itself is a fitting procedure performed on charge distributions in the padrow–time plane with the granularity of the bin sizes.
In the offline case, cluster finding is performed in a simultaneous two-dimensional fit in time and padrow direction. For the cluster fitting in the offline case, 5×5 bin regions are investigated. Note, that the actual cluster size is smaller than the 5×5 region, the typical size of clusters around the

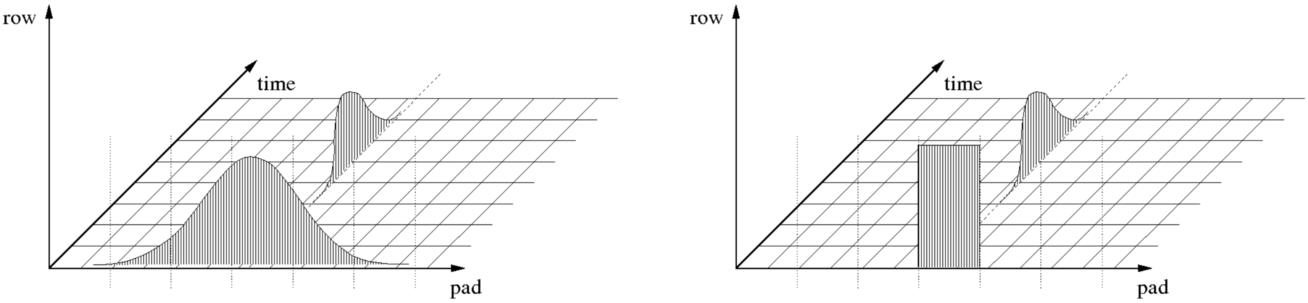

Figure 4.2.: Two different kinds of clusters are shown. Left: Normal clusters contain charge information, which is distributed over several pads and can therewith be fitted by a Gaussian function with reasonable error. Right: For single pad clusters only one pad exceeds the charge threshold. The pad resolution is deteriorated. The cluster fit and therewith also the track fit have large errors.

centre-of-gravity (COG) are σ_{pad} and σ_t, which both are approximately equal to 0.75 [85].

The online cluster finder processes one pad at a time in time direction, thus the COG is extracted by a one dimensional fit. The COG in pad direction is extracted by the comparison and merging of the neighbouring pads [86].

In high-multiplicity events, the track density is high. The distance between tracks, i.e. also between the clusters, is small and clusters can overlap. Clusters are deconvoluted in the offline and the online code. The offline code performs a polynomial interpolation to calculate the COG of both clusters. The online code extracts the minimum between the charge gradients and uses it for the cut sequence between the clusters.

A cluster is determined by the COG in y and z directions and by the widths, σ_y and σ_z, in these directions. The widths can be used later for the error estimation of the fit. Moreover, clusters are characterised by the maximum charge in one pad, Q_{max}, and the total deposited charge in the cluster Q_{tot}. In addition, the number of pads contributing to a cluster is important.

In Figure 4.2, two different cluster types are shown. On the left side a normal cluster is shown. A continuous charge distribution in the padrow dimension can be fitted by a Gaussian. On the right side a single-pad-cluster (SPC) is shown. Only one padrow bin exceeds the charge threshold. The Gaussian fit in the padrow direction gives consequently large errors.

SPCs were not used for tracking due to their detrimental impact on the transverse momentum resolution. However, SPCs are used for the calculation of the specific energy loss in the TPC.

In Figure 4.3 the cluster distributions are shown as comparison between cluster reconstructed online and offline. The distributions are normalised by their integral. A good agreement is reached between online and offline reconstructed clusters. The steps in the padrow distributions are due to the three different read-out chamber types along the radial direction, mentioned in Table 3.1. The distributions of σ_y^2 and σ_z^2 show a deviation between cluster reconstructed online and offline. This is a result of the different CFs.

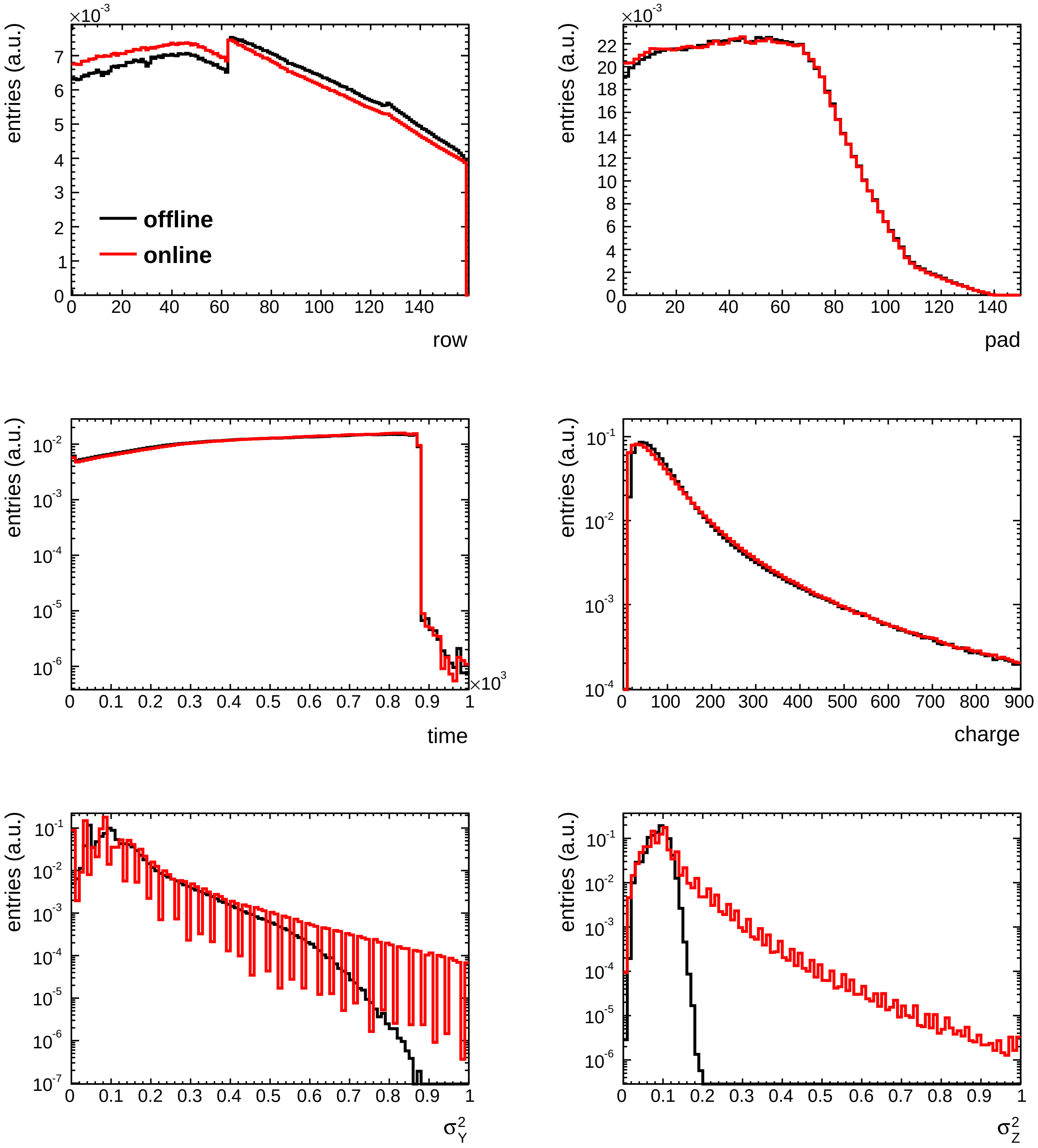

Figure 4.3.: Comparison of six cluster distributions between clusters reconstructed online (red) and offline (black). The distributions are normalised, such that the integral is equal to unity. Note, that the scale of the top two figures is linear.

4.2. Quality of tracks from clusters reconstructed online

The TPC is the main tracking device in the ALICE central barrel. The resolution of tracks is one of the central parameters for a precise measurement. Moreover, the energy loss information in the counting gas provides the possibility to identify charged hadrons and electrons over a large momentum range. When changing the cluster finding algorithm, it is crucial to preserve these functionalities and guarantee only minimal impact on physics analysis.

One fundamental quantity of tracking quality is the resolution of transverse momentum. This was studied in MC and data. The resolution σ_{TPC} using MC information is calculated by

$$\sigma_{\mathrm{TPC}} = \frac{{p_{\mathrm{T}}}^{\mathrm{rec}}}{{p_{\mathrm{T}}}^{\mathrm{MC}}} - 1, \tag{4.1}$$

where $p_{\mathrm{T}}^{\mathrm{MC}}$ and $p_{\mathrm{T}}^{\mathrm{rec}}$ are the transverse momenta at generation level and after full reconstruction, respectively.

For the generation of a MC sample for Pb–Pb collisions at $\sqrt{s_{\mathrm{NN}}} = 2.76$ TeV, different kinds of events, generated by HIJING [87] were produced. For the study of a high-multiplicity environment, Pb–Pb events in a centrality range of $0 - 5$ % were produced. To allow the study of high-p_{T} tracks, jets were embedded in minimum-bias HIJING events, including partons with $p_{\mathrm{T}} > 100$ GeV/c using PYTHIA [33].

In Figure 4.4 the transverse momentum resolution is shown for tracks using clusters reconstructed online or offline. The black points represent tracks with clusters fitted by the offline algorithm. The coloured points show the resolution for tracks using clusters reconstructed by the HLT, considering SPCs or disregarding SPCs used for tracking. Below 10 GeV/c the difference between transverse momentum resolution is about 8 % for tracks suppressing SPCs and about 12 % for tracks using SPCs, considering an offline transverse momentum resolution of about 3 %. Above 10 GeV/c the transverse momentum resolution is comparable between the two clustering algorithms within the quoted uncertainties. The worse p_{T} resolution of the tracks using SPCs for track reconstruction is a consequence of the large error which needs to be assigned to the cluster fit.

As mentioned above, also the particle identification capabilities are an important parameter for the quality of many analyses. A quality parameter for particle identification in the TPC is the separation power, which is defined as follows

$$S = \frac{\langle \mathrm{d}E/\mathrm{d}x \rangle_{p1} - \langle \mathrm{d}E/\mathrm{d}x \rangle_{p2}}{(\sigma_{p1} + \sigma_{p2})/2}, \tag{4.2}$$

where $\langle\ \mathrm{d}E/\mathrm{d}x\ \rangle$ and σ are the mean energy loss in the TPC and the width of the distribution surrounding the Bethe-Bloch expectation for two particle species $p1$ and $p2$, respectively.

At the beginning of pp data taking in 2010, only normal clusters were used for tracking and the calculation of the energy loss dE/dx. However, it turned out, that for the calculation of dE/dx the usage of SPCs improved particle identification capabilities. Therefore, during the pp run period in

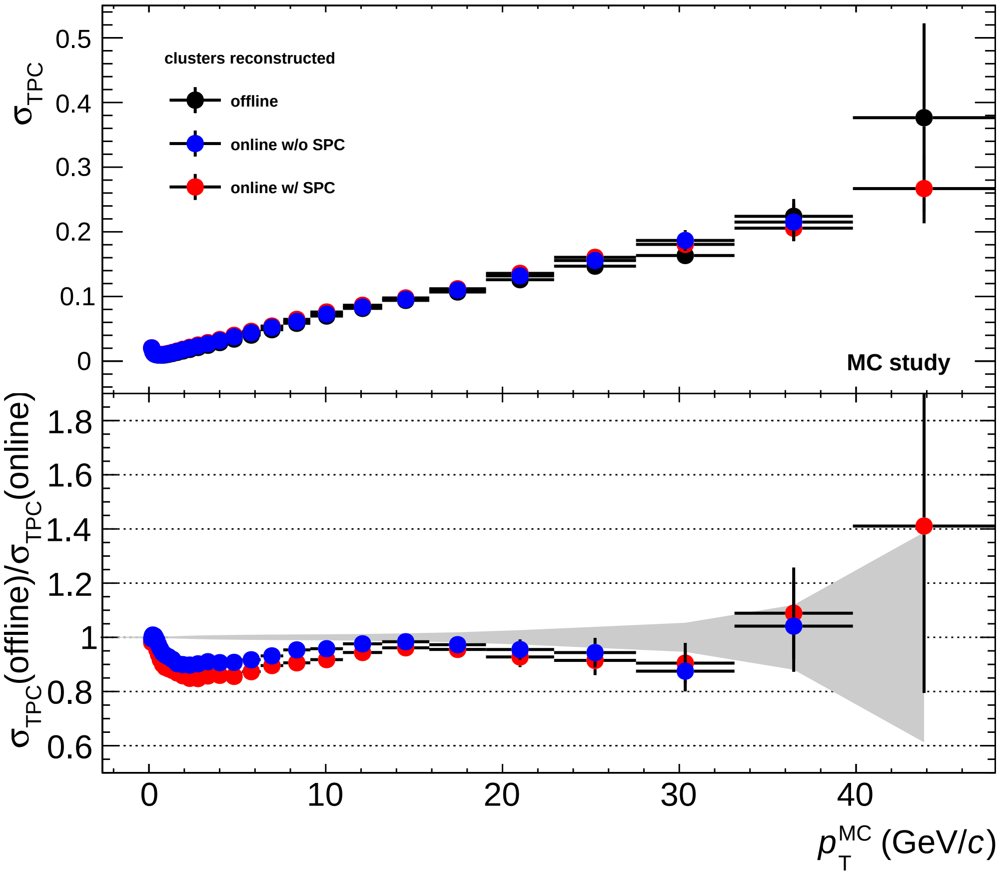

Figure 4.4.: The transverse momentum resolution for tracks only reconstructed in the TPC is shown for different cluster finding algorithms. For the clusters reconstructed online the cases are distinguished, which exclude (w/o SPC) or include (w/ SPC) the SPCs for tracking. The lower panel shows the ratio of the resolutions from tracks with clusters reconstructed online or offline. The grey band around unity represents the statistical uncertainty of the black reference points.

2010, SPCs were added for the energy loss calculation.

This was also re-evaluated during the commissioning of the use of clusters reconstructed online. In Figure 4.5, the $\mathrm{d}E/\mathrm{d}x$ distribution is shown for particles with $0.45 < p < 0.5$ GeV/c. On the left side, $\mathrm{d}E/\mathrm{d}x$ is shown for tracks from clusters reconstructed online. Two distributions are compared: In the one case, SPCs were included for the calculation of the $\mathrm{d}E/\mathrm{d}x$ and in the other case SPCs were excluded. The particle distributions are fitted by Gaussian functions to determine the mean and the width of the distribution. The results for the particle fits and the resulting separation power is included in the figure. The use of SPCs for the calculation of $\mathrm{d}E/\mathrm{d}x$ improves the separation power. This confirmed earlier findings from the 2010 pp Run. Consequently, SPCs are used for the calculation of the energy loss in the TPC.

On the right side of Figure 4.5, a comparison between the energy loss distributions in the TPC is shown for tracks from cluster reconstructed online and offline. Both distributions contain SPCs for the calculation of $\mathrm{d}E/\mathrm{d}x$. The separation power for tracks from clusters reconstructed online and

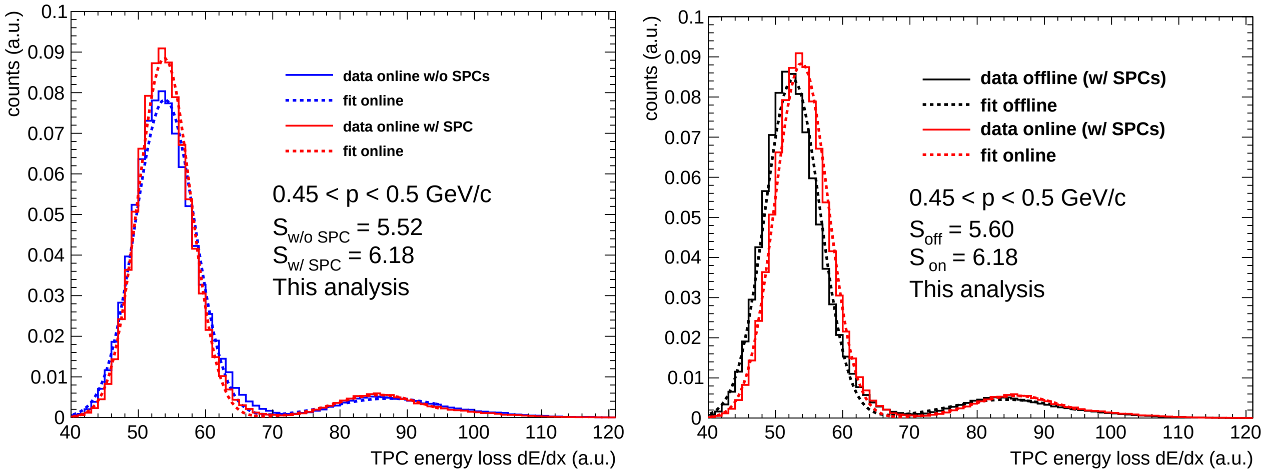

Figure 4.5.: dE/dx distribution of particles in the momentum region $0.45 < p < 0.5$ GeV/c. Left: Comparison between tracks with and without SPCs. Right: Comparison between tracks from clusters reconstructed online and offline.

offline is similar.

Minimum Ionizing Particles (MIPs) are located in the kinematic region of $\beta\gamma \approx 3.6$, i.e. in the case of pions at $p \approx 0.5$ GeV/c. MIPs are of particular importance for the calibration of the energy loss information in the TPC. In Figure 4.6, the mean and the width of MIPs is shown, determined by the fit of a Gaussian function to the dE/dx distribution of pions at $p \approx 0.5$ GeV/c.

In the upper panel of Figure 4.6, the mean position of MIPs is shown as a function of time for the runs collected over the full Pb–Pb data taking period 2011. For historical reasons, these MIPs result at a final value around 50 after calibration of the TPC.

Note, that in Figure 4.5 the mean position of tracks from clusters reconstructed online is shifted by about 10 % to higher values compared to the MIP position in Figure 4.6, since these runs were still calibrated with an algorithm tuned on tracks from clusters reconstructed offline in the early period of data taking. In Figure 4.6, the new calibration algorithm tuned for tracks from cluster reconstructed online was used and consequently the mean of the MIPs is located at 50 with negligible deviations.

In the lower panel of Figure 4.6, the resolution, i.e. width of the Gaussian distribution, of the MIPs in the TPC is shown for the corresponding distributions from the upper panel. The MIP resolution over the entire Pb–Pb data taking period in 2011 was about 8 %.

The trending of both distributions shows a stable behaviour over the four weeks of data taking. A stable tracking and particle identification performance was achieved with clusters reconstructed and compressed online.

4.3. Summary of the Pb–Pb data taking and outlook

It was shown, that the online cluster finder operated in the HLT produced cluster distributions and results comparable to the offline cluster finder. This was the case in emulated MC simulations

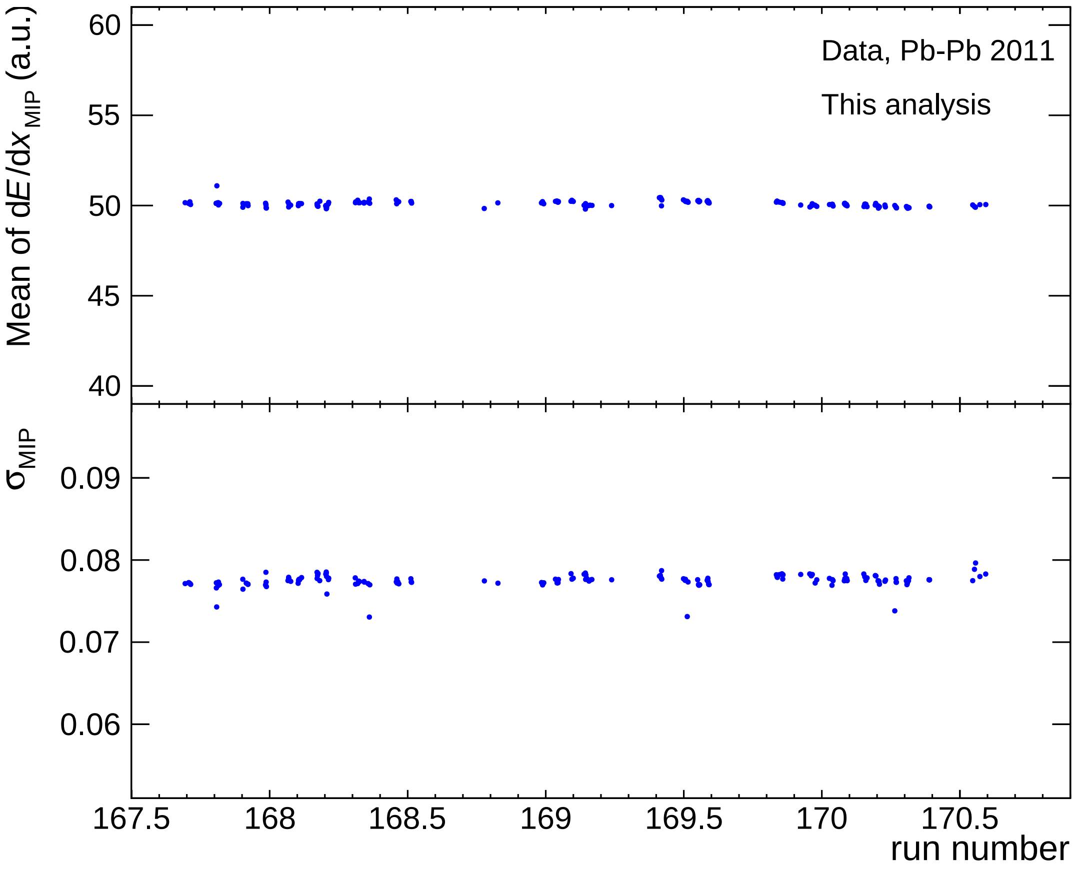

Figure 4.6.: The mean (upper panel) and the resolution (lower panel) of MIPs for all runs taken for physics analysis over the full Pb–Pb data taking period in 2011 with TPC clusters reconstructed and compressed online.

and real data for different collision systems. On the track level, the performance was similar for the transverse momentum resolution and the particle identification and stable over the entire data taking period. The online reconstruction and data compression of clusters is operational and the default running mode since Pb–Pb data taking 2011.

In Figure 4.7, the data compression factor versus the raw data size is shown. An average compression factor of 4.4 was achieved, which was even beyond the aimed compression factor.

On the left side of Figure 4.8, the luminosity as a function of time is shown for one fill during the Pb–Pb data taking 2011. The upper plot shows the luminosity measured with the ALICE ZDC. The lower panel shows the integrated distribution of the upper panel. The steps within the integration curve corresponds to times when ALICE was not taking data. On the right side of Figure 4.8, the integrated and recorded luminosity of all fills injected during the Pb–Pb data taking is shown. In total, an integrated luminosity of $\int \mathrm{d}t\, \mathscr{L} \approx 145\ \mu\mathrm{b}^{-1}$ was recorded by ALICE, which is about 90 % of the luminosity delivered by the LHC [89, 90].

Due to the clusters reconstructed and compressed online in the TPC, ALICE inspected a statistics about 15 times larger during the Pb–Pb run 2011 compared to the Pb–Pb run 2010.

Since electrons are rare probes, large data samples are a crucial requirement for any successful

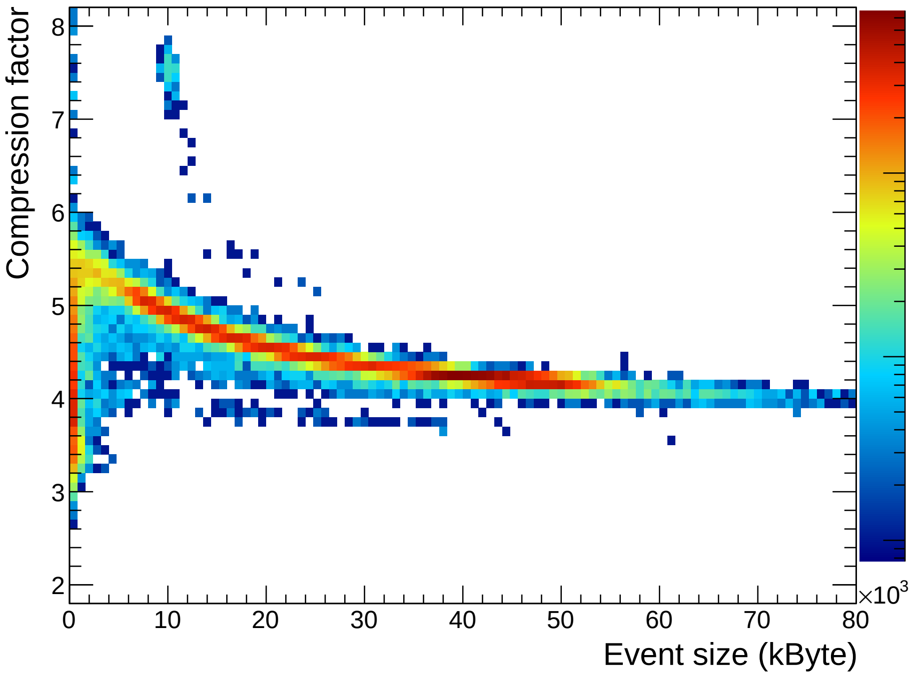

Figure 4.7.: The compression factor of the raw data is shown versus the raw data size of Pb–Pb events. In average, a data compression of 4.4 was achieved, allowing for the processing of a larger data volume. From [88].

dielectron measurement. The currently ongoing dielectron analysis in Pb–Pb collisions at a centre-of-mass energy of $\sqrt{s_{NN}} = 2.76$ TeV benefits from the 15 times larger statistics collected.

The future of the dielectron program in ALICE is strongly depending on the upgrade of the ALICE central barrel. As stated in [91], one major interest in the upgrade of the ALICE detector system, is a precise and systematic analysis of dielectron production in Pb–Pb collisions at mid-rapidity down to lowest transverse momenta. A precise vertexing with an upgraded ITS provides the rejection of dielectrons coming correlated from open-charm decays.

However, one of the main challenges is the read-out of a trigger rate of Pb–Pb events at 50 kHz. It is planned to run the TPC in a continuous read-out mode with an online calibration performed with the HLT. The HLT is foreseen to further compress the data and perform a complete online track reconstruction. However, it should be noted, that the track reconstruction is only done for cluster selection reasons. Only the clusters associated to tracks will be stored permanently and the reconstruction of the tracks will be done offline. The experience gained in the commissioning of the clusters reconstructed and compressed online by the HLT was an important first step towards the continuous running mode.

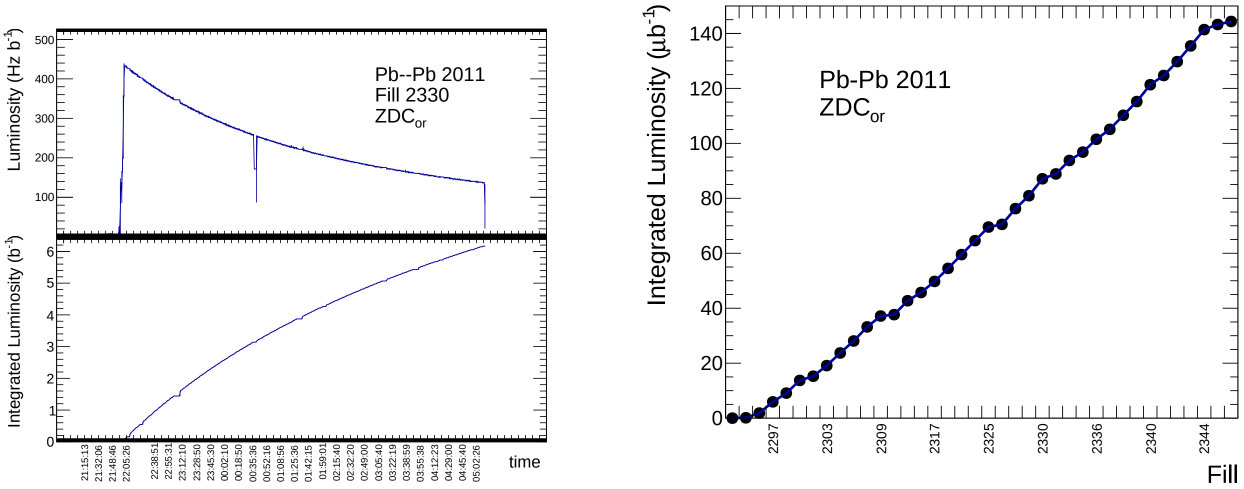

Figure 4.8.: Left upper panel: Luminosity evolution of a fill in Pb–Pb data taking 2011 measured by ALICE. Left lower panel: Integrated luminosity over time from the upper figure. Right: Integrated luminosity of all fills in the LHC during Pb–Pb data taking in 2011.

5. Dielectron analysis of pp collisions at 7 TeV

The physics goal of this analysis is to compare the measured dielectron yield with the expected dielectron sources from hadronic decays.

The major steps in the data analysis are

- event selection,
- track analysis,
- pair analysis,
- corrections.

In section 5.1 the overall selection of data suited for physics analysis is described. The quality criteria and the trigger selection are discussed.

For this analysis, it is mandatory to find a compromise between an electron sample with a high purity and an acceptable electron efficiency. In section 5.2, the selection of tracks is described. The identification of electrons and the rejection of hadrons are discussed. The remaining contamination of hadrons is estimated by a data driven procedure. The pairing procedure and the selection of pairs is described in detail in section 5.3.

A major challenge in dielectron analyses is the estimation of the combinatorial background, i.e. the calculation of the number of dielectron combinations which are produced during the pairing process but do not contribute to the physics signal. The ratio of the physics signal over the combinatorial background depends on the event multiplicity and therewith on the collision energy. The rejection of dielectrons from photon conversions in the detector material, will be discussed.

The detector acceptance and efficiency are always limited. The impact of the detector itself on the data analysis and the analysis cuts needs to be corrected to get a meaningful comparison to detector-independent calculations or theoretical models. The correction of the efficiency based on Monte Carlo (MC) calculations will be described in section 5.4.

To some extent, the measurement or the cocktail can not be corrected. Therefore, one needs to estimate the magnitude of this uncertainty. In section 5.5 the systematic uncertainties due to the applied track cuts and the background subtraction are estimated.

In section 5.6 the known dielectron sources from hadronic decays are combined to a so-called cocktail. The dielectron mass distribution is calculated based on the known decay kinematics.

5.1. Data selection

The data analysis of pp collisions at $\sqrt{s} = 7$ TeV presented in this work is based on data collected in the year 2010. The pp collisions were collected with a minimum-bias trigger (CINT1-B), which requires a hit in either one of the VZERO counters or in the SPD detector [92, 93].

Events are rejected, which do not come from a beam-beam collision, but from a collision of the circulating beam with rest gas in the beam pipe. Pile-up events, i.e. events with more than one interaction within a bunch crossing, are rejected by a SPD selection criterion.

A geometrical criterion is applied on the z position of the vertex. The distance of the collision vertex in z direction is required to be smaller than 10 cm from the nominal collision point.

In Figure 5.1 the z_{vertex} distribution after event filtering is shown for a period of about two month data taking (LHC10d). The distribution is fitted with a Gaussian function. The values shown in the figure correspond to the number of events after physics selection, after event filtering ($|z_{\mathrm{vertex}}| < 10$ cm) and to the integral of the fitted Gaussian function. The vertex inefficiency is estimated by

$$N_{\mathrm{MB}}^{\mathrm{corr}} = N_{\mathrm{MB}}^{\mathrm{PhysSel}} \times \frac{N_{\mathrm{ev}}^{|z_{\mathrm{vertex}}|<10\ \mathrm{cm}}}{N_{\mathrm{ev}}^{\mathrm{Gauss}}}, \tag{5.1}$$

where the corrected number of minimum-bias events $N_{\mathrm{MB}}^{\mathrm{corr}}$ is given by the number of events after physics selection $N_{\mathrm{MB}}^{\mathrm{PhysSel}}$ times the ratio of the integrals of the histogram and the Gaussian fit. The ratio is about 0.85 over the period of data taking in 2010. This value is in agreement with previous analyses, e.g. [94]. After vertex efficiency correction, 3.49×10^6 events are available for the analysis.

To normalise the dielectron yield in terms of the total cross section, the minimum-bias collision cross section σ_{MB} is needed. It can be calculated by

$$\sigma_{\mathrm{MB}} = \frac{N_{\mathrm{MB}}}{N_{\mathrm{V0AND}}} \sigma_{\mathrm{V0AND}}, \tag{5.2}$$

where N_{MB} and N_{V0AND} are the number of events from the minimum-bias trigger and from the V0AND trigger. The V0AND trigger requires hits in the V0A and the V0C detector. The cross section of the V0AND trigger $\sigma_{\mathrm{V0AND}} = 54.34 \pm 1.9(\mathrm{sys})$ mb was measured in a Van der Meer scan [95]. The resulting minimum-bias cross section is then

$$\sigma_{\mathrm{MB}} = 63.2 \pm 0.4(\mathrm{stat}) \pm 4.3(\mathrm{syst})\ \mathrm{mb}. \tag{5.3}$$

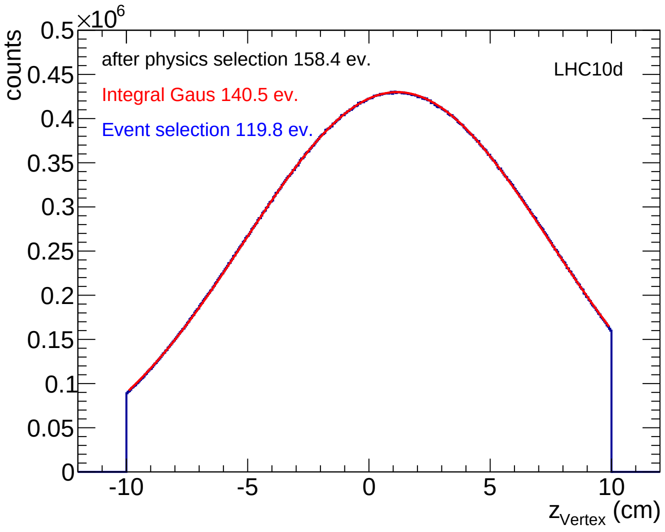

Figure 5.1.: The z_{vertex} distribution of collisions recorded in a period of about two months. The values show the number of events after the selection of beam-beam collisions, the integral of the fitted Gaussian function and the number of events after applying the selection on z_{vertex}.

5.2. Track selection

5.2.1. Quality cuts

To ensure a good quality of tracks in the analysis, several selection criteria are applied. This includes selection criteria on detector quantities and on global track kinematics.
In the ITS, tracks need to fulfil the following selection criteria:

- At least three out of six possible clusters in the ITS need to be assigned to the track.
- The track has to be refitted[1] in the ITS.
- The track needs to produce a signal in the first layer of the SPD. Since photons can not produce a signal in the SPD, this rejects all electrons, which come from a photon conversion in the detector material at a larger radius than the first SPD layer.

In the TPC, the following track cuts are applied:

- To reject short or curling tracks, at least 100 out of 159 possible rows in the TPC need to be crossed by the track.
- The track needs to be refitted in the TPC.

---

[1] A track is refitted, if the last inward tracking fit is successful within the corresponding detector, see section 3.4.

- The quality of the track fit in the TPC can be described by the residuals between the track and the clusters,

$$\chi^2/n_{cl}^{\mathrm{TPC}} = \frac{1}{n_{cl}^{\mathrm{TPC}}} \sum_{i=0}^{n_{cl}^{\mathrm{TPC}}} \frac{y_{i,cl} - y_{i,\mathrm{track}}}{\sigma_{i,y}^2} + \frac{z_{i,cl} - z_{i,\mathrm{track}}}{\sigma_{i,z}^2},$$

  where σ_y and σ_z correspond to the space point resolution in pad and drift direction. In this analysis, the quality of the fit was required to be $\chi^2/n_{cl}^{\mathrm{TPC}} < 4.0$.

Required global track properties are

- Only tracks with a transverse momentum of $p_{\mathrm{T}}^{e} > 0.2$ GeV/c are accepted in the analysis. Particles below this transverse momentum are deflected by the magnetic field out of the TPC before storing enough information in the detector. The tracking efficiency in the TPC drops below this transverse momentum.

- The pseudorapidity range is limited to $|\eta^e| < 0.8$. The tracking efficiency beyond this value is very steep and therefore not straightforward to be corrected.

- The distance-of-closest-approach of a track to the reconstructed vertex (DCA) is used in a two dimensional way to reject non-physical outliers. In direction to the beam, the track prolongation needs to be closer than $\mathrm{DCA}_z < 3$ cm. In radial direction, particles from secondary vertices are rejected by requiring $\mathrm{DCA}_{xy} < 1$ cm. It should be noted, that this cut is chosen to be looser than in other analyses of primary particles. This is due to semi-leptonic open heavy-flavour mesons, which can decay in a larger distance from the primary vertex.

- High transverse momentum tracks are weakly bended by the magnetic field in the detector and can be double reconstructed. This artificially enhances dielectrons with the same sign with very small opening angle, i.e. very small invariant mass. So tracks are rejected, which share more than one percent of their clusters with each other in the TPC. This removes about 1 % of the tracks.

- Particles from a secondary vertex and two-body kinematics, i.e. one mother and one daughter with the same charge, are likely to come from weak decays. These particles with a so-called kink topology are rejected.

5.2.2. Electron identification

For particle identification, it is indispensable to find a combination of detector quantities, which is unique for this particular particle species and makes it separable from all other particle species. The identification of electrons at low momentum is one of the central challenges in this analysis. In the following, the electron identification method in the relevant detectors, TPC and TOF, is described.

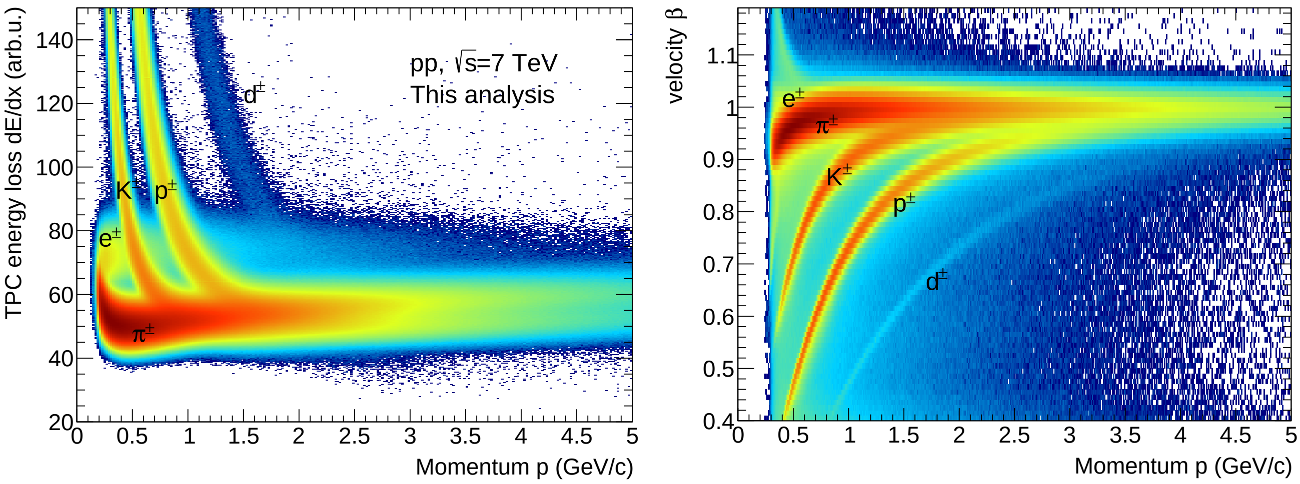

Figure 5.2.: Left: The specific energy loss $\mathrm{d}E/\mathrm{d}x$ of particles in the gas of the TPC versus the momentum of the particle. Right: the velocity of particles measured in the TOF detector versus the particle momentum. Contributions from positive and negative particles are superimposed.

The average energy loss of a charged particle within a gaseous volume can be described by the Bethe-Bloch formula [96], which is given by

$$\left\langle \frac{\mathrm{d}E}{\mathrm{d}x} \right\rangle = \frac{4\pi N e^4}{m_e c^2} \frac{z^2}{\beta^2} \left\{ \ln\left(\frac{2 m_e c^2 \beta^2 \gamma^2}{I^2} \right) - \beta^2 - \frac{C}{2} - \frac{\delta(\beta)}{2} \right\}, \tag{5.4}$$

where,

N	is the number density of electrons in the matter traversed,
z	is the charge of the projectile,
β, γ	are the velocity and the relativistic Lorentz-factor,
I	is the effective potential of ionisation, and
C, δ	are empirical correction coefficients for shell and density effects, respectively.

The energy loss in the TPC gas depends on the velocity β, the mass and the charge of the traversing particle. On the left side of Figure 5.2, the energy deposition associated to a track in the TPC is shown as a function the particle momentum. In this representation, different particle species are distinguishable by their specific behaviour, following the Bethe-Bloch formula. For low-momentum particles, i.e. small $\beta\gamma$, the curve has a $1/\beta^2$ behaviour and reaches a minimum at $\beta\gamma \approx 3.6$. With increasing $\beta\gamma$ the energy loss increases due to the logarithmic term and enters the so-called relativistic rise.

Due to the relatively small mass difference between electrons and pions, the energy loss behaviour of electrons and pions in the TPC is similar for higher momenta. A good separation between electrons and pions is achieved in the low momentum region, $0.25 \lesssim p \lesssim 2$ GeV/c. At higher momenta, the pion band approaches the electron band on its relativistic rise. In the momentum region $p \approx 0.7$ and $p \approx 1.2$ GeV/c, kaons and protons share the same energy loss information. In

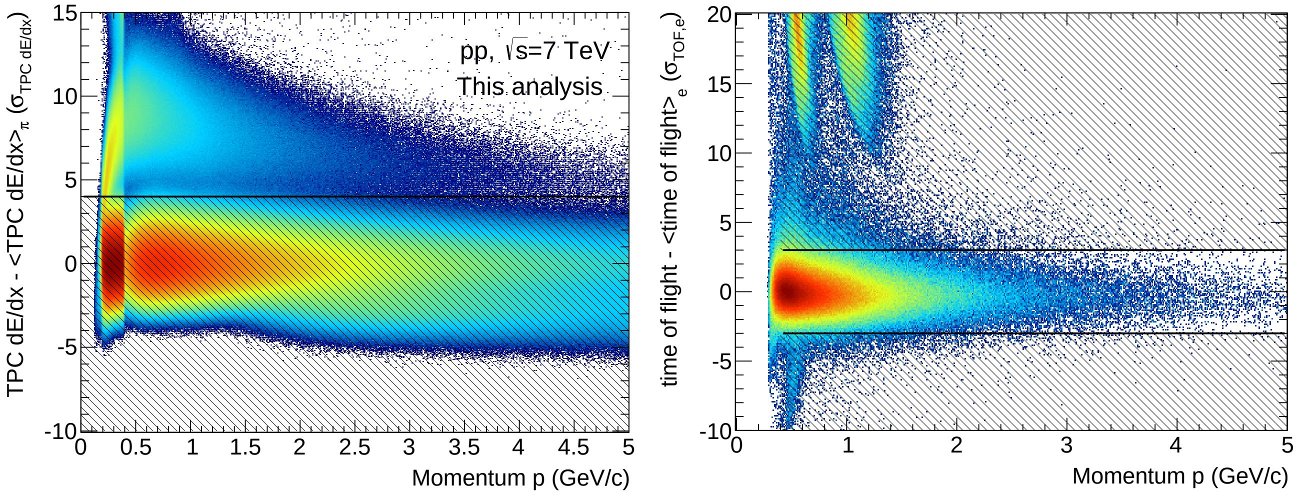

Figure 5.3.: Left: The specific energy loss in the TPC is shown after the kaons and proton rejection in the TOF detector as the deviation from the expected energy loss for pions, normalised by the energy loss resolution. Right: The time-of-flight information is shown for the expected time of electrons as a function of particle momentum after the pion rejection in the TPC. Particles with higher mass, i.e. kaons and protons, have a larger arrival time. Contributions from positive and negative particles are shown.

this momentum region, the TOF detector is used to reject kaons and protons.

On the right side of Figure 5.2, the particle velocity in terms of β measured with the TOF detector is shown as a function of particle momentum. Since electrons have a very small mass, their velocity is $\beta \approx 1$ already at small momenta. Electrons cannot be separated from pions due to their rather small mass compared to kaons or protons. Kaons and protons reach, due to their larger mass, only at a momentum of $3 - 4$ GeV/c a velocity of $\beta \approx 1$. Below this momentum electrons can be separated very efficiently from kaons and protons with the TOF. To obtain a clean electron sample, the rejection strategy is the following: pions are rejected in the TPC and kaons and protons in the TOF.

In the whole momentum region $p_{\mathrm{T}} > 0.2$ GeV/c, the following cuts are applied in the TPC

$$-1.5 < \sigma_e(\text{TPC}) < 3 \qquad \text{(inclusion)} \tag{5.5}$$

$$-100 < \sigma_\pi(\text{TPC}) < 4 \qquad \text{(exclusion).} \tag{5.6}$$

Soft particles with $p_{\mathrm{T}} < 0.4$ GeV/c are bended by the magnetic field, such that these particles do not reach TOF. Consequently, TOF is not efficient for transverse momenta below 0.4 GeV/c and TOF information is only required for transverse momenta $p_{\mathrm{T}} > 0.4$ GeV/c. Since electrons cannot be separated from hadrons above 5 GeV/c in TOF, see the right panel of Figure 5.2, TOF is used for kaon and proton rejection only for $p_{\mathrm{T}} < 5$ GeV/c. So in the transverse momentum region $0.4 < p_{\mathrm{T}} < 5$ GeV/c kaons and protons are rejected by an inclusion cut on the expectated

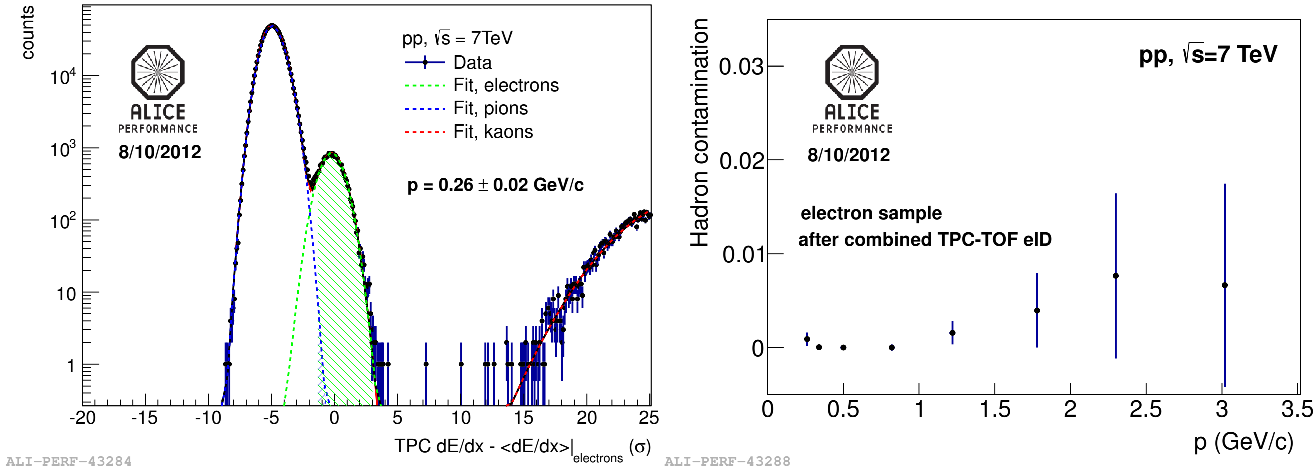

Figure 5.4.: Left: The $\mathrm{d}E/\mathrm{d}x$ distribution was fitted with a Gaussian function in different momentum ranges. The shaded area under the Gaussian function indicates the electron identification cuts. Right: Estimation for the hadron contamination in the electron candidate sample. The integrals of the fit results within the electron selection criteria are used for the estimation. The integral of the fits results in a contamination of at most 1 %.

the time of flight of an electron,

$$|\sigma_e(\mathrm{TOF})| < 3. \tag{5.7}$$

Deuterons are also visible in the left and in the right panel of Figure 5.2, but can be neglected for this analysis.

On the left side of Figure 5.3, the energy loss in the TPC in terms of the pion expectation is shown as a function of momentum after the kaon and proton rejection in the TOF for transverse momentum $p > 0.4$ GeV/c. In the very low momentum region, $p \approx 0.2$ GeV/c, the pion band approaches the electron band, which necessitates the rejection of particles 4σ below the pion hypothesis. The rejection region is indicated by the shaded area.

On the right side of Figure 5.3, the TOF information in terms of the expected time of electrons in the TOF is shown as a function of particle momentum after the pion rejection in the TPC. The remaining particles are mainly electrons, kaons and protons. Kaons and protons are visible at much larger arrival times compared to the electron expectation. They can be separated from electrons and are rejected with a very high efficiency.

The contamination of the selected electron candidate sample is estimated in a data driven procedure. On the left side of Figure 5.4 the TPC energy loss information of electron candidates is shown for a given momentum interval. Particle distributions are fitted by Gaussian functions. This is done for several momentum slices. From the integral of the fits, the hadron contamination can be estimated.

The hadron contamination $C(p)$ is calculated as follows,

$$C(p) = \left. \frac{\sum_{\text{pion}} + \sum_{\text{kaon}} + \sum_{\text{proton}}}{\sum_{\text{all}}}(p) \right|_{\text{cuts}}, \tag{5.8}$$

where $\sum_{\text{particle}}$ is the integral of the Gaussian fit to the corresponding particle within the electron identification cut ranges. The cut ranges are indicated on the left side of Figure 5.4 by the shaded area under the Gaussian functions. Only shaded areas under the Gaussian functions are considered for the calculation of the contamination.

The resulting hadron contamination as a function of the particle momentum is shown on the right side of Figure 5.4. The hadron contamination is well below 1 % over the momentum region of interest. For $p < 0.4$ GeV/c, which contains about 2/3 of the electron candidates, the contamination is on the level of 10^{-4}.

5.3. Pair analysis

The invariant mass of a multi-body decay is

$$M^{\text{inv}} = \sqrt{\sum_{i=1}^{k} p_i^{\mu} p_{\mu}^{i}} = \sqrt{\sum_{i=1}^{k} (E_i)^2 - \sum_{i=1}^{k} (\vec{p_i})^2}, \tag{5.9}$$

where $p_i^{\mu} = (E_i, \vec{p_i})$ is the four-momentum of the i-th particle with $i = \{1, 2, ..., k\}$.

Dielectrons are pairs of electrons and positrons with the invariant mass m_{ee} calculated as follows,

$$m_{ee} = \sqrt{(E_{e_1} + E_{e_2})^2 - (\vec{p}_{e_1} + \vec{p}_{e_2})^2}, \tag{5.10}$$

where the index e_i corresponds to a single leg of the pair. The energy of the electron E_e is calculated as follows,

$$E_e = \sqrt{(\vec{p_e})^2 + m_e^2}, \tag{5.11}$$

where $m_e = 0.511$ MeV/c^2 is the electron rest mass.

By definition, signal dielectrons are unlike-sign pairs, i.e. the two legs within a pair have opposite charges. The dielectron signal consists of hadron decays and semi-leptonic decays of correlated open heavy-flavour hadrons and, moreover, of internal conversions of virtual photons.

Since the origin of individual electrons and positrons is not known, every electron needs to be combined with every positron in each event, which passes the event and track selection criteria. Hence, also pairs are created, which do not contribute to the dielectron signal. The resulting distribution of measured opposite sign pairs N_{+-} is a superposition of a the physics signal S_{+-}

and a background B_{+-} of dielectron combinations,

$$N_{+-} = S_{+-} + B_{+-}.$$

The background is the sum of a combinatorial, i.e. uncorrelated, component and a correlated component. The uncorrelated background originates from randomly paired dielectrons.

The correlated background originates from higher-order dielectron correlations, where for example dielectrons do not have the same parent, but have the same grand-parent. An example is the photonic decay $\pi^0 \rightarrow \gamma\gamma$. Both photons can convert in the detector material and produce a dielectron pair, which is correlated by the π^0 mass. The pairs are referred to as cross pairs.

Another source of correlated background are di-jets produced in initial hard scatterings. Electrons in one jet are correlated to electrons from the other jet by the jet kinematics. These pairs show up at high masses, since their opening angle is large. But also electrons from different particle decays within the same jet can be correlated. Since their opening angle is small, these pairs appear mainly at low dielectron masses. However, these pairs also can have large masses if the momenta of the legs are large. These pairs are referred to as jet pairs.

For the extraction of the dielectron signal, the dielectron background needs to be subtracted. The analysis and subtraction of the dielectron background will be discussed in section 5.3.1.

Photons which are produced in the collision can convert in the detector material into dielectrons. These photon conversions appear in the unlike-sign dielectron spectrum, but do not contribute to the dielectron signal. Moreover, electrons from photon conversions increase the combinatorial background. Therefore, photon conversions need to be rejected. This will be discussed in section 5.3.2.

5.3.1. Background subtraction

In contrast to analyses, which deal with the measurement of sharp signal shapes, such as resonances on a top of a continuous background, the dielectron background cannot be disentangled from the signal by a fit. The dielectron continuum is a broad signal with a non-trivial shape. Moreover, the signal-over-background ratio is small (order of 10 % in pp collisions at $\sqrt{s} = 7$ TeV). The background therefore needs to be calculated statistically and independently from the measured unlike-sign spectrum.

To estimate the background distribution, pairs need to be generated which are not correlated in the parent generation. Three methods are established to calculate the dielectron background: same-event like-sign technique, mixed event technique and track rotation. These methods will be discussed in the following.

Like-sign technique Under the assumption, that the signal dielectrons always consist of opposite-sign pairs[2], the dielectron background can be estimated by pairs, where the single legs have

---

[2] In section 5.6.2, an exception for this assumption is shown. Neutral open beauty mesons can undergo particle-

the same charge. The geometric mean of the like-sign distribution is calculated by

$$N_{\mathrm{LS}} = 2 \times \sqrt{N_{++}N_{--}} * R, \tag{5.12}$$

where N_{++} and N_{--} are pairs with twice positive or negative sign, respectively. In order to generate the proper mass distribution with the correct normalisation, the geometrical acceptance of like-sign and unlike-sign pairs has to be equal. The factor R in Eq. 5.12 takes into account possible acceptance differences between like-sign and unlike-sign pairs. The calculation of the acceptance difference R will be discussed later. The normalisation of the like-sign distribution is straightforward since the same particles within one event are used.
A unique characteristic of the like-sign distribution is, that it also includes the correlated background. As mentioned before, the correlated background comes from dielectron pairs originating from the same grand-parent or from correlated dielectrons within a jet. Dielectrons from the decay

$$\pi^0 \rightarrow \gamma\gamma \rightarrow e_1^+ e_1^- e_2^+ e_2^-,$$

contribute to the like-sign spectrum, e.g. $e_1^- e_2^-$ In the same way, they contribute to the unlike-sign spectrum, e.g. $e_1^+ e_2^-$. These pairs are subtracted by the same-event like-sign method.

Mixed event technique The uncorrelated background in the measured unlike-sign spectrum can be generated by pairing electrons and positrons from different events. Under the constrain, that the events have a similar topology, such as the z_{vertex} in pp collisions or the centrality for the case of Pb–Pb collisions, one can pair electrons from two or more events to reduce the statistical uncertainty. Event mixing can produce a combinatorial background with extremely high statistical accuracy.
With a perfect 4π detector acceptance, the normalisation would be inversely proportional to the number of mixed events. In real data, detector acceptance and pair cuts can lead to a bias. Therefore one usually normalises the mixed event spectrum to the like-sign spectrum in a kinematic region, where contributions from correlated background is expected to be negligible.
In this analysis, events are mixed in pools with a depth of ten events. Eight pools were generated for equidistant z_{vertex} bins in the range $z_{\mathrm{vertex}} = \{-10.0; ...; 10.0\}$ cm.
The invariant mass distributions of mixed events are only influenced by the detector acceptance. Generated pairs from mixed events with unlike-sign or like-sign can reproduce the acceptance difference between pairs with opposite and same charge for pairs within the same event. The

---

antiparticle oscillation. Moreover, electrons from different generations of a open beauty meson decay can be combined. Therefore dielectrons from beauty decays can produce physical like-sign pairs.

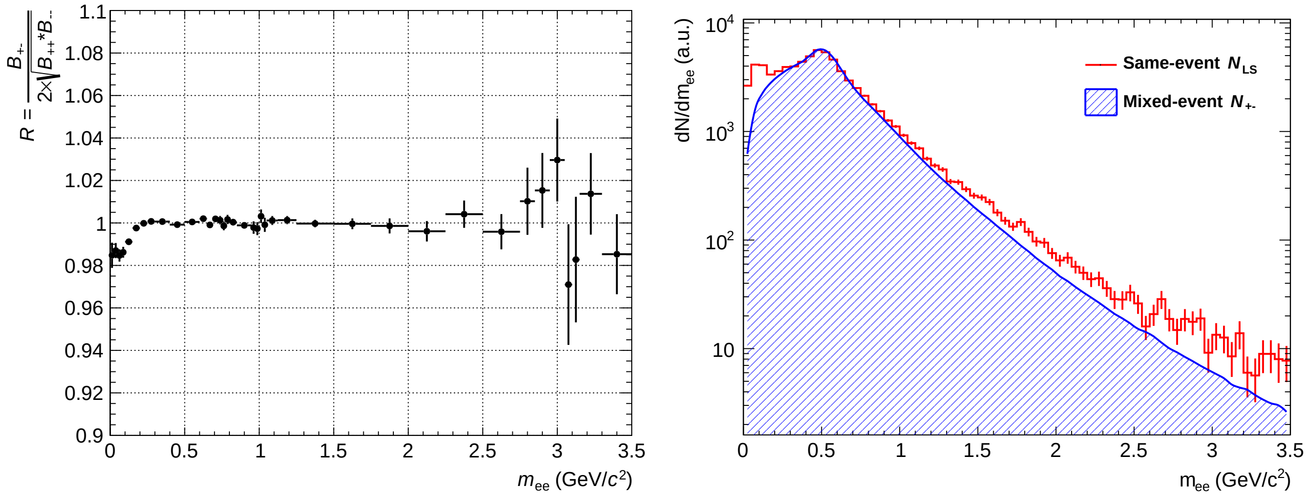

Figure 5.5.: Left: The acceptance ratio between unlike-sign and like-sign pairs R as a function of the invariant mass integrated over all pair p_{T} for $p_{\mathrm{T}}^{e} > 0.2$ GeV/c, calculated with Eq. 5.13. Right: Same-event unlike-sign distribution in comparison to mixed event unlike-sign distribution as a function of the invariant mass.

R factor from Eq. 5.12 is therefore calculated by

$$R = \frac{B_{+-}}{2 \times \sqrt{B_{++} * B_{--}}}, \tag{5.13}$$

where B_{+-}, B_{++} and B_{--} are mixed event distributions from unlike-sign, positive like-sign and negative like-sign pairs, respectively. Since the ALICE central barrel has a full azimuthal coverage, the value for R is supposed to be close to unity. It turns out, that the result is strongly depending on the p_{T} cut applied on single electrons. The lower the electron p_{T} cut is, the better is the agreement of R with unity.

On the left side of Figure 5.5, R is shown as a function of the invariant mass. It is consistent with unity within the statistical uncertainty for $m_{ee} > 0.1$ GeV/c^2.

On the right side of Figure 5.5, the mixed event unlike-sign spectrum, normalised to the same-event like-sign distribution in the mass region $0.5 < m_{ee} < 0.8$ GeV/c^2, is compared to the same-event like-sign spectrum. The like-sign spectrum shows an enhancement compared to the mixed event spectrum, which is caused by the correlated background sources, which contribute to the same-event like-sign distribution only. While in the low-mass region $m_{ee} < 0.2$ GeV/c^2 the enhancement comes mainly from cross pairs, the enhancement in the high-mass region comes from jet pairs.

Track rotation The kinematic correlation within a dielectron can be destroyed by rotating at least one of the two legs by a randomly chosen angle. The statistical precision of this method can be increased by rotating a leg more than once. However, the normalisation of the background

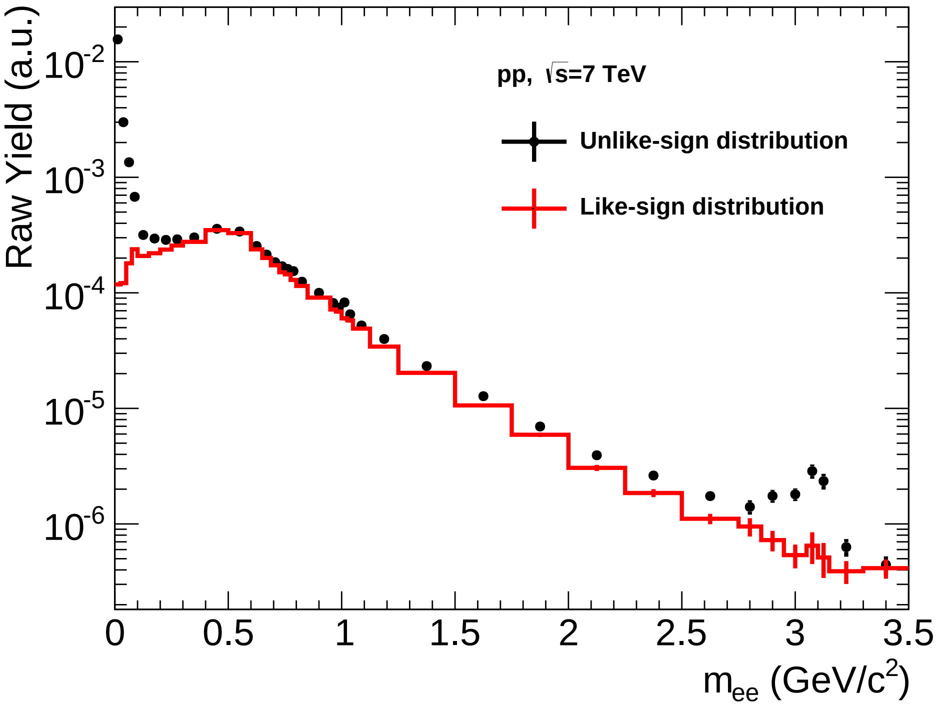

Figure 5.6.: The unlike-sign dielectron distribution including the combinatorial background is shown as a function of invariant mass. The like-sign distribution represents the combinatorial background.

with this method is not straightforward. Also a limited detector acceptance can bias the shape dof the background distribution. This method is not used for this analysis.

In Figure 5.6 the same-event unlike-sign spectrum is shown together with the same-event like-sign spectrum. Almost all unlike-sign pairs can be assigned as background. In this analysis, the same-event like-sign technique is used for the estimation of the combinatorial and correlated background. The acceptance difference between the like-sign and unlike-sign distribution R is neglected. As can be seen in the left panel of Figure 5.5, R is consistent with unity within the statistical uncertainties for $m_{ee} > 0.1$ GeV/c^2. Since the signal-over-background ratio is very high, the impact of R on the signal for $m_{ee} < 0.1$ GeV/c^2 is negligible.
The raw signal S_{+-} is then calculated by the subtraction of the like-sign distribution N_{LS} of the unlike-sign distribution N_{+-}:

$$S_{+-} = N_{+-} - N_{\mathrm{LS}}. \tag{5.14}$$

5.3.2. Conversion rejection

One of the main sources contributing to the combinatorial background are electrons which originate from photon conversions in the detector material. Due to energy and momentum conservation, real photons can convert into a dielectron in material only. As mentioned in section 5.2.1, all electron

candidates are required to have a hit in the first layer of the SPD. Since photons do not produce a signal in SPD layers, all photon conversions in the outer detector material do not contribute to the signal. This requirement rejects the majority of photon conversions.
However, there is still a non-negligible fraction of photons, which can convert in the beam pipe material, in air, or in the first SPD layer itself. To identify and reject these remaining electrons, a two step procedure has been established:

1. ALICE has a good position resolution photon conversion, see [97]. So electrons with a displaced vertex coming from a photon conversion can be tagged and removed from further pairing. One can distinguish between the tagging efficiency and the signal efficiency.

   Tagging Efficiency The tagging efficiency ϵ_{tag} is given by the ratio

   $$\epsilon_{\text{tag}} = \left. \frac{\mathrm{d}N/\mathrm{d}m^{\text{tag}}_{\gamma\to ee}}{\mathrm{d}N/\mathrm{d}m^{\text{conv}}_{\gamma\to ee}} \right|_{\text{in pair acceptance}}, \tag{5.15}$$

   of tagged photon conversions $\mathrm{d}N/\mathrm{d}m^{\text{tag}}_{\gamma\to ee}$ over all photon conversions $\mathrm{d}N/\mathrm{d}m^{\text{conv}}_{\gamma\to ee}$ within the pair acceptance. The tagging efficiency is calculated from a full minimum-bias MC and is shown in the left panel of Figure 5.7 as a function of the invariant mass in the region $m_{ee} < 0.04$ GeV/c^2.
   Dielectrons, which are identified as photon conversions by this method, are removed from the further pairing procedure to reduce the combinatorial background. In the right panel of Figure 5.7 the ratio of signal-over-background distributions before and after removal of photon conversion pairs is shown extracted from data. The ratio is systematically above unity, indicating the better signal-over-background ratio after the rejection of conversion pairs. Only in the very low mass region $m_{ee} < 0.25$ GeV/c^2, the ratio is reduced. Since photon conversions have an opening angle almost equal to zero, the corresponding dielectron masses are also small. The removal of true conversion pairs, which are included into the signal in the denominator, results therefore in a reduction of the ratio.

   Signal Efficiency The signal efficiency ϵ_S for dielectrons is calculated from full minimum-bias MC simulation, as follows

   $$\epsilon_S = \left. \frac{\mathrm{d}N/\mathrm{d}m^{\text{after}}_{ee}}{\mathrm{d}N/\mathrm{d}m^{\text{before}}_{ee}} \right|_{\text{signal in pair acceptance}}, \tag{5.16}$$

   where $\mathrm{d}N/\mathrm{d}m^{\text{after}}_{ee}$ and $\mathrm{d}N/\mathrm{d}m^{\text{before}}_{ee}$ are true signal pairs in the pair acceptance before and after applying the conversion rejection by displaced vertex identification. It turns out, that the signal efficiency of the conversion tagging is $\epsilon_S = 1$, i.e. 100 %. No signal pairs are misidentified. Another test was also done on a simulation enhanced with D and B mesons. Since these mesons decay at a displaced vertex, the results are very sensitive for misidentification of displaced vertices as photon conversions. The test confirmed the

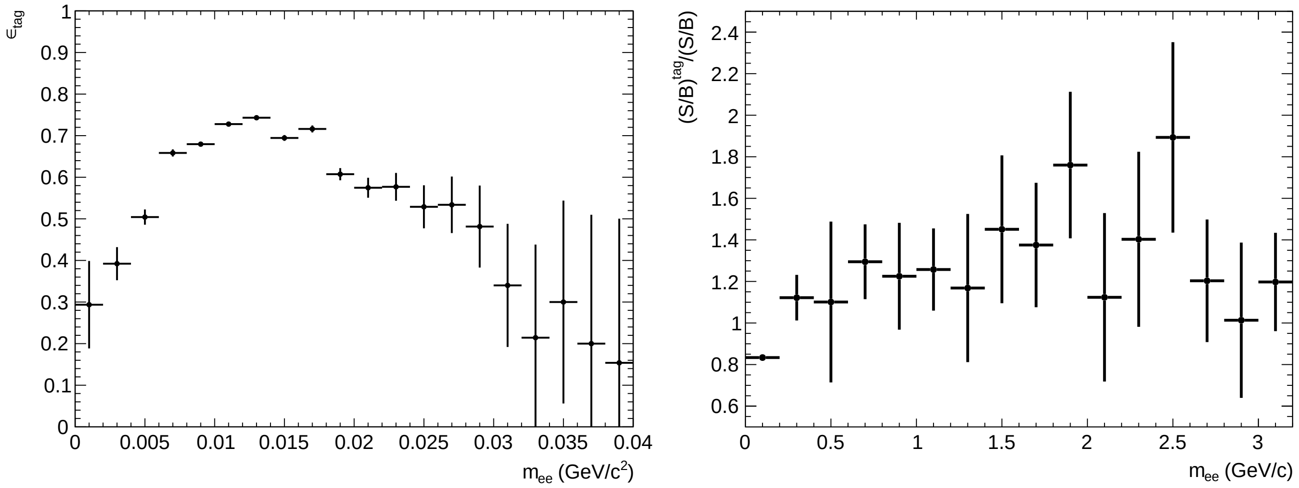

Figure 5.7.: Left: The photon conversion tagging efficiency is shown in dependence of the dielectron invariant mass. Right: The ratio of signal-over-background distributions as a function of invariant mass extracted from dielectrons before and after the rejection of photon conversions by their displaced vertex.

observation from the analysis of the minimum-bias simulation, that the signal efficiency is $\epsilon_S = 1$.

2. As can be seen in the left panel of Figure 5.7, the tagging efficiency is about $70 - 80$ %. There are still photon conversions left in the dielectron sample. Therefore, an additional rejection step is applied to the dielectrons.

   Another method, which was established in previous dielectron analyses by PHENIX, see e.g. [98, 57], is the identification of photon conversions by the kinematic orientation of the dielectrons with respect to the external magnetic field of the detector. Since this is a purely geometrical quantity, data is well described by MC.

   The momentum vectors of the single legs span up a plane. Primary dielectrons have an isotropic angular distribution ϕ_V of this plane with respect to the magnetic field. Photon conversions have no intrinsic opening angle. So the opening angle of photon conversions is only induced by the magnetic field. In that way, dielectrons from photon conversions are sensitive to the magnetic field of the detector. Their decay plane is oriented perpendicular to the magnetic field direction of the detector.

   However, this rejection step can remove also a significant fraction of signal pairs, since dielectrons from the collision vertex are isotropically distributed around the ϕ_V. Therefore the rejection step on this angle is only applied in a small mass range. The two dimensional cut is applied as

$$\begin{aligned} \phi_V &< 2.5 \text{ rad} && (5.17) \\ \text{in the mass range } m_{ee} &< 0.15 \text{ GeV}/c^2. && (5.18) \end{aligned}$$

The efficiency of the ϕ_V cut will be discussed in the next section.

5.4. Efficiency correction

Every detector has only a limited efficiency. To allow a meaningful comparison to models and theory, detector efficiencies need to be corrected. Different effects are taken into account,

- detector dead areas,
- reconstruction software (tracking etc.),
- single electron cuts and particle identification cuts,
- cuts on the pair level.

For the correction of the efficiency, a MC sample is produced with PYTHIA 6 [33]. The minimum-bias sample is enriched with dielectrons with realistic particle distributions as function of p_{T}, η and φ. Particle ratios are reproduced correctly. For the particle transport through the detector, GEANT3 [99] is used.

Figure 5.8 shows the comparison between data and MC simulation of the mean and width of the $\mathrm{d}E/\mathrm{d}x$ in the TPC for electrons. Three different track quantities are shown. The clean electron sample in data is extracted from photon conversions identified by their displaced vertex and the their V^0 topology. The underlying two-dimensional distributions are produced from data. For this purpose no cuts in the ITS are applied to not reduce the amount of photon conversions. The deviation between MC and data up to $\Delta\langle \mathrm{d}E/\mathrm{d}x\rangle_e \approx 0.2\sigma$ is in agreement with the $\mathrm{d}E/\mathrm{d}x$-resolution in the TPC of about $(5-6)$ % for pp collisions.

Several procedures exist to correct a dielectron mass distribution for efficiency. In this work, first the efficiency for the reconstruction of a single electron is calculated as a function $(p_{\mathrm{T}}, \eta, \varphi)$. The electron efficiency is used as a weighting factor in a fast MC simulation with proper electron and dielectron kinematics.

The electron efficiency is calculated as follows

$$\mathrm{Eff} = \frac{N^e_{\mathrm{reconstructed}}}{N^e_{\mathrm{generated}}}(p_{\mathrm{T}}, \eta, \varphi)\Bigg|_{p_{\mathrm{T}}>0.2\ \mathrm{GeV}/c, |\eta|<0.8}, \tag{5.19}$$

where $N^e_{\mathrm{reconstructed}}$ and $N^e_{\mathrm{generated}}$ are the numbers of electrons remaining after the full reconstruction and analysis chain and the number of electrons at the generator level, respectively. It should be noted that both, the reconstructed and generated electron sample, are filtered in the kinematic acceptance of the analysis, i.e. $p_{\mathrm{T}} > 0.2$ GeV/c and $|\eta| < 0.8$. To correct for the acceptance, the kinematic distributions outside of the ALICE acceptance would need to be known or estimated by models. Therefore, all results are only efficiency corrected within the ALICE central barrel acceptance.

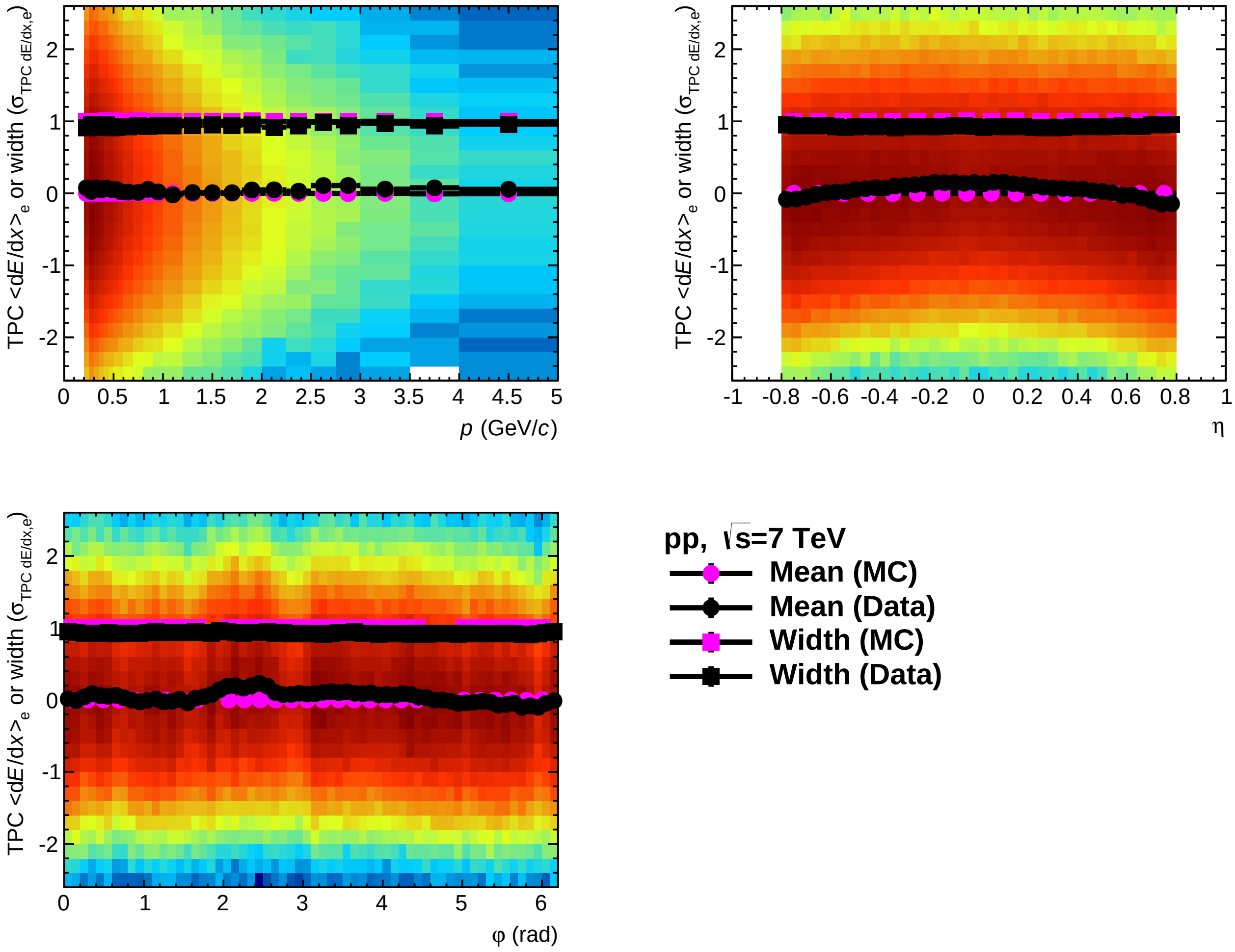

Figure 5.8.: Comparison of the mean and width of the electron dE/dx in the TPC between data and MC as a function of momentum (upper left), pseudorapidity (upper right) and azimuthal angle (lower left). The electron sample in data is extracted from photon conversions, which are identified by their displaced vertex and their V^0 topology. In the MC sample, true primary electrons are selected after full detector simulation. The underlying coloured distributions are the two-dimensional distributions from data.

On the left side of Figure 5.9, efficiencies extracted from MC simulation after track cuts and after electron identification for electrons are shown as a function of transverse momentum. The efficiency after track cuts has a flat behaviour over the transverse momentum range. Applying the electron identification cuts in TPC and TOF induces a reduction of the efficiency. Below 0.4 GeV/c a TPC only electron identification reduces the efficiency by about 15 %. Above 0.4 GeV/c additionally to the electron identification in the TPC the matching between TPC and TOF reduces the efficiency by about 40 %. This is seen by the rapid drop.

To correct for the efficiency of dielectron reconstruction, a pair efficiency is needed. The electron efficiencies as function of $(p_{\mathrm{T}}, \eta, \varphi)$ are used as weighting factors. The dielectron generator has realistic electron and dielectron kinematics. On the right side of Figure 5.9, the resulting invariant mass distribution from the pair generator is shown for dielectrons before and after the electron

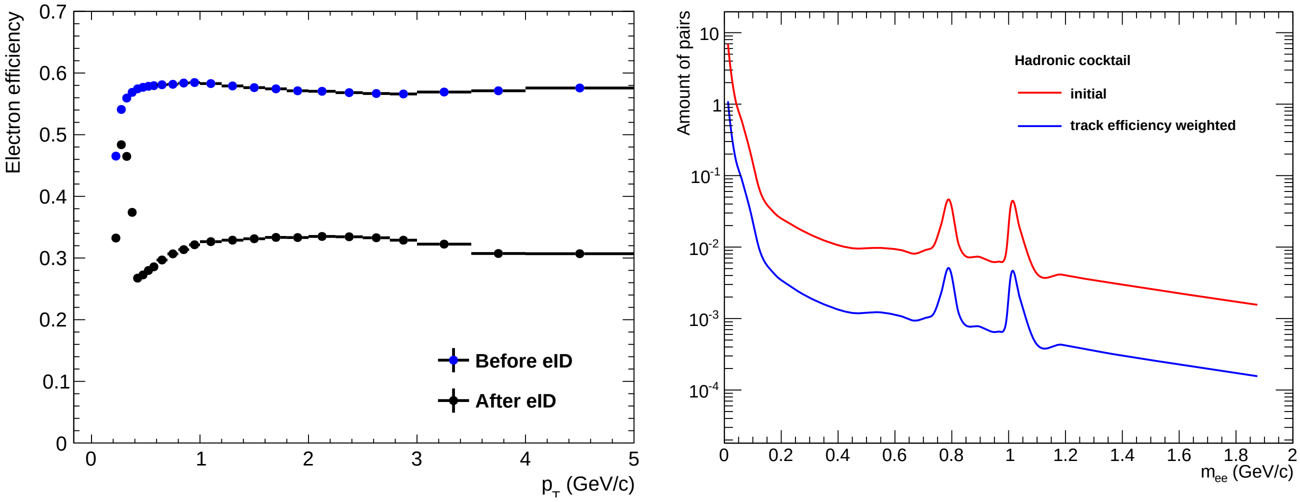

Figure 5.9.: Left: The single electron efficiency after applying the track cuts and after applying the electron identification in TPC and TOF additionally. Right: Dielectron pair distributions from a fast simulation with realistic electron and dielectron kinematics. The upper dielectron spectrum shows the initial pair distribution. The lower spectrum is weighted on single electron level with the single leg efficiency.

efficiency weighting. The single electron resolution is applied on both pair generators, so that there are no smearing effects around the resonances.

This procedure to obtain the pair efficiency does not guarantee, that single leg correlations within a dielectron pair are taken into account properly. This was tested by running an independent efficiency calculation on pair level. The resulting efficiency distributions were consistent within their uncertainties.

On the left side of Figure 5.10, the pair efficiency is shown as a function of the dielectron invariant mass. It is calculated as the ratio of the two dielectron mass distributions, which are shown on the right side of Figure 5.9. It has a decreasing structure for the low-mass region and is approximately constant for masses above 1 GeV/c^2. The origin of this behaviour can be explained by the single electron efficiency, left side of Figure 5.9. High-mass dielectrons have dominantly single electrons with high-p_T, which occupy the flat plateau in the single electron efficiency.

On the right side of Figure 5.10, the signal efficiency of the ϕ_V cut is shown as a function of the invariant mass. The cut is only applied for $m_{ee} < 0.15$ GeV/c^2, which causes the step at this mass. The efficiency is also consistent with the assumption, that all signal dielectrons are emitted isotropically over the ϕ_V space. The efficiency therefore would be calculated as $1 - (\pi - 2.5)/\pi \approx 0.79$.

As mentioned above, the signal efficiency of the conversion rejection on the V^0 topology of conversions is 100 %.

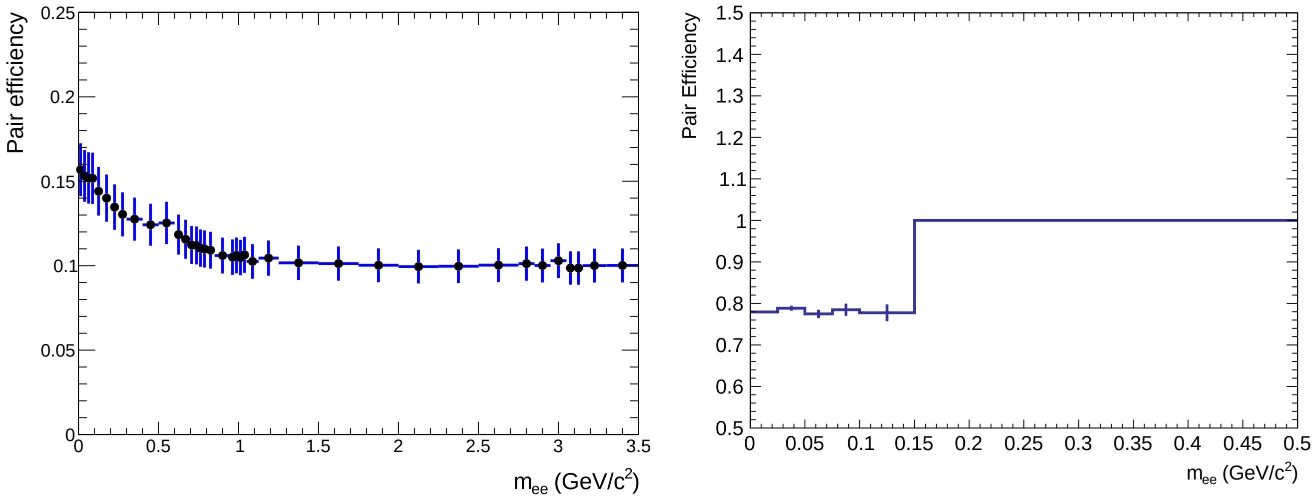

Figure 5.10.: Left: The dielectron pair efficiency coming from cuts on track level is shown as a function of the dielectron invariant mass. Right: The signal loss induced by the cut on the ϕ_V as a function of the dielectron invariant mass. Note, that the cut was only applied for $m_{ee} < 0.15$ GeV/c^2, which causes the step in the efficiency.

5.5. Systematic uncertainties

Two main sources are considered for the systematic uncertainty of the final result. The systematic uncertainty of the data analysis and the systematic uncertainty of the cocktail. The systematic uncertainty of the data analysis will be discussed in this section. The systematic uncertainty of the expected hadronic sources will be discussed in section 5.6.3.

There are several sources, which contribute to the systematic uncertainty of the data analysis and the resulting invariant mass spectrum

- track cuts,
- subtraction of the combinatorial background,
- normalisation.

The largest contributor to the systematic uncertainty in the intermediate and low mass region is the subtraction of the combinatorial background. It is given by

$$\frac{\mathrm{d}S}{S} = \frac{\mathrm{d}B}{B} \times \left(\frac{S}{B}\right)^{-1}, \tag{5.20}$$

where $\mathrm{d}S/S$ and $\mathrm{d}B/B$ are the relative systematic uncertainties of the signal and the combinatorial background, respectively. The signal-over-background ratio S/B is shown in the left panel Figure 5.11. In regions of the invariant mass, where S/B is small, the systematic uncertainty on the extracted signal is large.

To estimate the systematic uncertainty of the combinatorial background, two methods to calculate

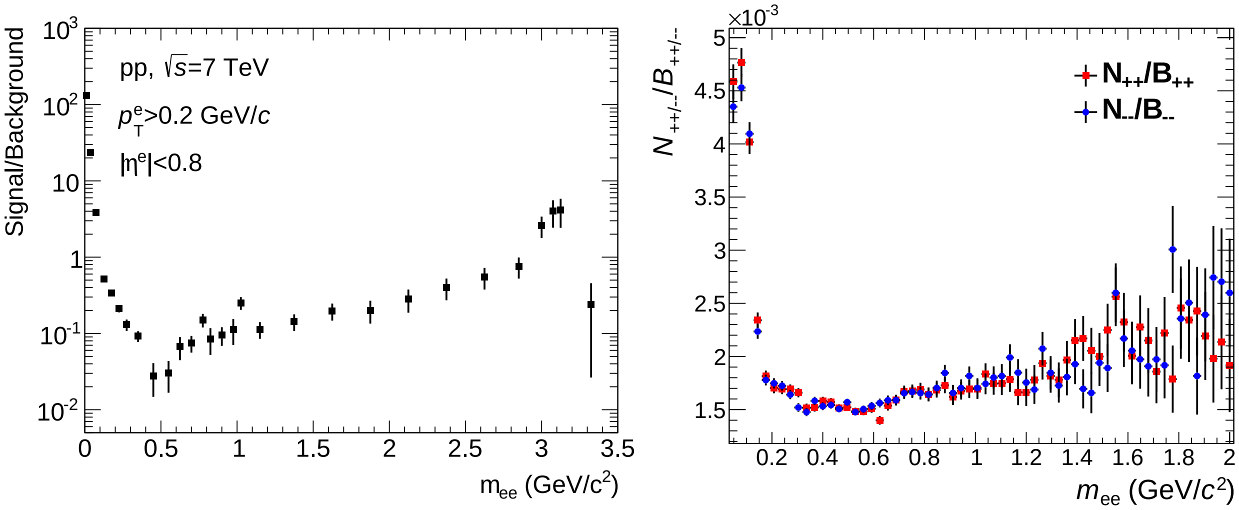

Figure 5.11.: Left: The signal-over-background ratio S/B is shown as a function of the invariant mass. Right: The ratio between same-event and mixed event like-sign distribution as a function of the invariant mass.

the signal are compared.

The first signal is calculated by the subtraction of the dielectron background corrected by R, which leads to

$$S_1 = N_{+-} - 2 \times \sqrt{N_{++}N_{--}} * R. \tag{5.21}$$

The second signal is calculated by

$$S_2 = N_{+-} - a_1 \times (B_{+-} + B_{-+}) - a_2 \times \{2 * \sqrt{N_{++} * N_{--}} - a_1 \times (B_{++} + B_{--})\}, \tag{5.22}$$

where the factors a_1 and a_2 correspond to normalisation factors of mixed events and the relative acceptance difference between like-sign and unlike-sign pairs. In Eq. 5.22, the subtraction of the second term from the first term results in the superposition of the signal and correlated background, i.e. cross pairs and jet pairs. The latter are removed by subtracting the term proportional to a_2 in Eq. 5.22. This physics signal is comparable to the one extracted in 5.21. The stability of the signal is estimated by the systematic evaluation of the results from Eq. 5.21 and Eq. 5.22 depending on the variation of a_1 and a_2.

The initial value for the normalisation factor a_1 is estimated by the ratio of same-event like-sign pairs and mixed-event like-sign pairs, which is shown on the right side of Figure 5.11 as a function of the invariant mass for positive and negative like-sign pairs.

The ratio falls off at small masses below $m_{ee} \approx 0.1$ GeV/c^2 and a gradually increase at higher masses. This can be assigned to the correlated background. In the region $m_{ee} \approx 0.6$ GeV/c^2 the contribution of correlated background in the like-sign distribution is expected to be negligible. The initial value for a_1 is estimated to be 1.5×10^{-3}.

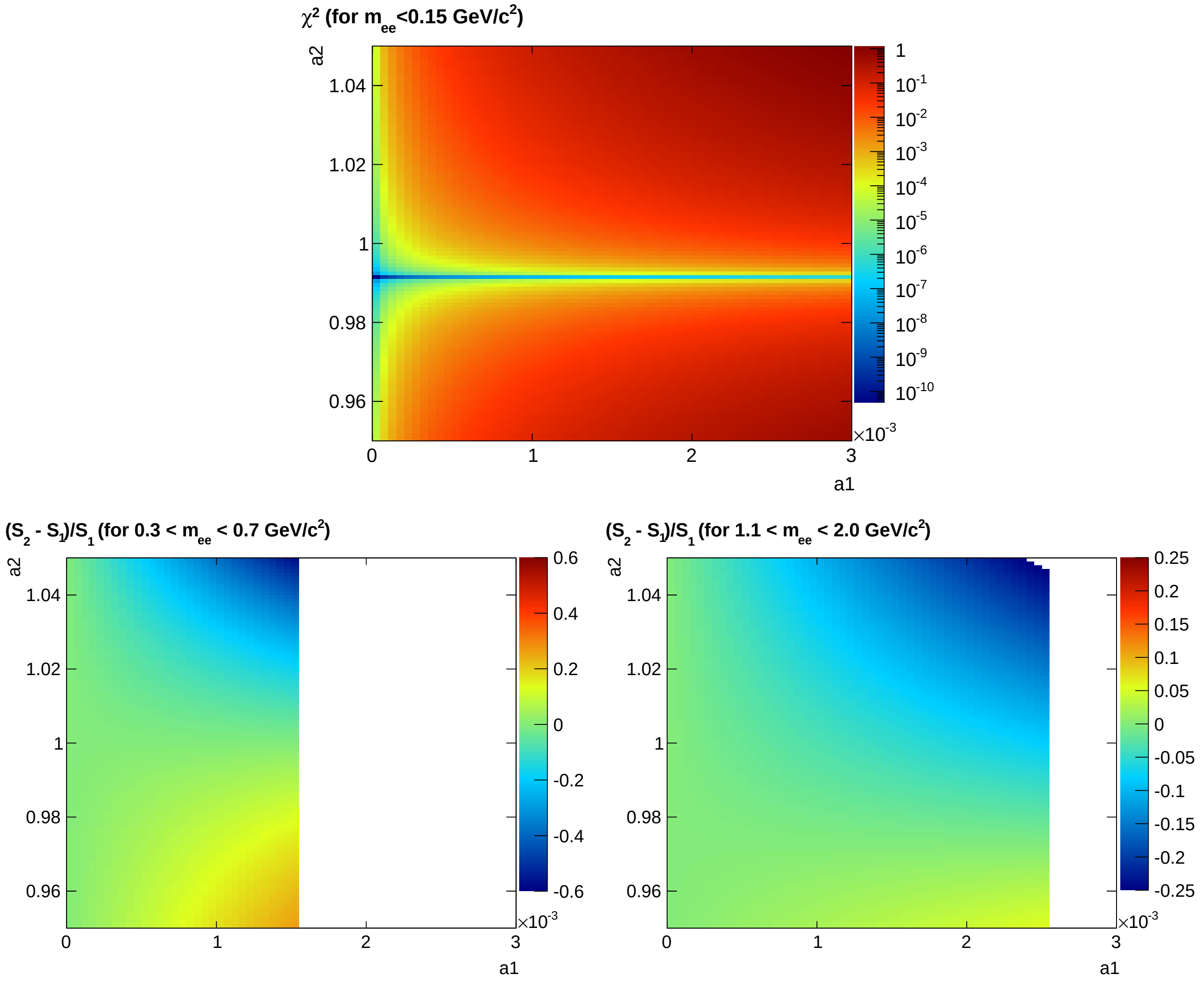

Figure 5.12.: Upper panel: The deviation of the S_1 and S_2 is shown in terms of the χ^2 as a function of the normalisation factors a_1 and a_2. Lower panel: Difference between the two signals S_1 and S_2 in the invariant mass region $0.3 < m_{ee} < 0.7$ GeV/c^2 (left panel) and in the invariant mass region $1.1 < m_{ee} < 2.0$ GeV/c^2 (right panel). Note, that the cut-off on the a_1 axis is resulting from the constraints defined in Eq. 5.24 and Eq. 5.25. For details, see text.

The acceptance correction factor a_2 is identified with the former R factor and estimated to be equal to unity, see Figure 5.5.

For the systematic evaluation of the combinatorial background, the deviation of the two signals is investigated in terms of the χ^2, which is calculated as follows

$$\chi^2 = \frac{(S_2 - S_1)^2}{(\mathrm{d}S)^2}. \tag{5.23}$$

The quantity χ^2 is calculated as a function of a_1 and a_2 for the invariant mass $m_{ee} < 0.15$ GeV/c^2, which is dominated by the Dalitz decays of the π^0, where the signal-over-background ratio is large. The resulting spectrum is shown in the upper panel of Figure 5.12. The overall agreement between

the two signals functions is excellent.
Note, that the very low values for χ^2 at $a_2 \approx 0.99$ in the upper panel are consistent for the results of the R factor in the low-mass region, see left panel of Figure 5.5.
For the following, the calculation of $\mathrm{d}S$ is constrained for the space in (a_1, a_2), where

$$\chi^2 < 1\sigma \tag{5.24}$$

for the range $m_{ee} < 0.15$ GeV/c^2. Moreover, the (a_1, a_2) space will be limited to

$$2 \times \sqrt{N_{++}N_{--}} - a_1 \times (B_{+-} + B_{-+}) > 0, \tag{5.25}$$

since the contribution of the correlated background can not be negative.
In the following, the deviations of the signal are calculated in (a_1, a_2) space for different mass regions, since the signal-over-background ratio is strongly mass dependent.
In the lower left panel of Figure 5.12 the ratio $(S_2 - S_1)/S_1$ for the invariant mass region $0.3 < m_{ee} < 0.7$ GeV/c^2 is shown as a function of a_1 and a_2. The maximum deviation is ≈ 0.33. Together with a signal-over-background ratio of 0.06 in the mass region $0.3 < m_{ee} < 0.7$ GeV/c^2 this results in a systematic uncertainty of the combinatorial background of 0.020, i.e. 2.0 %.
In the lower right panel of Figure 5.12 the ratio $(S_2 - S_1)/S_1$ is shown for the mass region $1.1 < m_{ee} < 2.0$ GeV/c^2. The maximal deviation is about 0.13. The signal-over-background ratio for this mass region is $S/B \approx 0.16$, which results in a systematic uncertainty of about 2.0 %.
Over the entire mass range $0 < m_{ee} < 3.5$ GeV/c^2, the systematic uncertainty of the combinatorial background is estimated to be 2.0 %.
The systematic uncertainty due to track cuts used for the analysis are extracted by varying the track cuts, introduced in section 5.2. In Table 5.1 and Table 5.2 the cut variations applied on the selection criteria for track cuts and electron identification cuts are shown, respectively.
The invariant mass distributions are extracted with varied cuts are corrected for efficiency and normalised as described in the section before. The relative deviation of the fully corrected and normalised mass distributions induced by the variation of the track cuts is assigned as systematic uncertainty. The deviations in the resulting mass spectra are due to the insufficient description of the data distributions in MC, which lead to a difference in the efficiency and therefore in a deviation between the final mass spectra. The pair reconstruction and calculation of the invariant mass is the dominating source of systematic uncertainties for invariant mass regions with a good signal-over-background ratio. A detailed study on the different analysis steps is performed to cover the systematic uncertainties which can arise.

In summary, the systematic uncertainty of the dielectron yield is about 10.0 % for the mass region $0 < m_{ee} < 3.5$ GeV/c^2.
In Table 5.3, the systematic uncertainties of this analysis are summarised. Additionally to the above described systematic uncertainties, the uncertainty from the normalisation, i.e. from the minimum-bias cross section σ_{MB} is shown, which is 7 %, see [95].

cut	default				
Number of ITS cluster	3	$\underline{4}$	3	3	3
Requirement of pixels in the SPD	first	first	$\underline{\text{both}}$	first	first
Number of crossed rows in the TPC	100	100	100	$\underline{120}$	100
Track deviation from assigned clusters (χ^2/cluster)	4	4	4	4	$\underline{3.2}$

Table 5.1.: Variation of the selection criteria to estimate the systematic uncertainty of the quality cuts. The columns show the different selection settings. The variations from the default setting are underlined.

cut	default				
TPC nσ_e	$-1.5 < \sigma_e < 3$	$\underline{-1. < \sigma_e < 2.5}$	$\underline{-2. < \sigma_e < 2.5}$	$-1.5 < \sigma_e < 3$	$-1.5 < \sigma_e < 3$
TOF nσ_e	$\lvert\sigma_e\rvert < 3$	$\lvert\sigma_e\rvert < 3$	$\lvert\sigma_e\rvert < 3$	$\underline{\lvert\sigma_e\rvert < 2}$	$\underline{\lvert\sigma_e\rvert < 4}$

Table 5.2.: Variation of the selection criteria to estimate the systematic uncertainty due to the electron identification cuts. The columns show the different selection settings. The variations from the default setting are underlined.

5.6. Cocktail simulations

The expected hadronic sources of dielectrons are calculated by using the measured hadronic cross sections and the knows decays kinematics. The cocktail represents the expected hadronic sources at the time of the freeze-out.

It is divided in two parts:

1. dielectrons coming from hadron decays,
2. dielectrons from correlated heavy-flavour hadron decays.

The hadron decays are calculated with a fast MC simulation in PYTHIA [33] which is embedded in the AliRoot analysis framework and tuned on EXODUS [100]. This is discussed in section 5.6.1. The contributions from correlated dielectrons of open heavy-flavour decays are calculated with LO and NLO MC generators, which are discussed in section 5.6.2. The systematic uncertainties of the cocktail are discussed in section 5.6.3.

In order to produce cocktail simulations which are comparable to data, two effects are added to the cocktail contributions, which can not be corrected in the analysis.

1. Bremsstrahlung is emitted by electrons passing detector material. The effect of bremsstrahlung is evaluated via a full MC simulation.

   The comparison of the momentum on generator level and after reconstruction as a function of the reconstructed momentum is shown on the left side of Figure 5.13. The effect of the bremsstrahlung is quantified via

$$\frac{\Delta p}{p} = \frac{p^{\text{generated}}}{p^{\text{reconstructed}}} - 1. \tag{5.26}$$

Syst. Uncertainty	
comb. bkg.	$2.0\ \% * (S/B)^{-1}$
reconstruction and electron ID	10.0 %
cross section (MB)	7 %

Table 5.3.: Compilation of the systematic uncertainties of data.

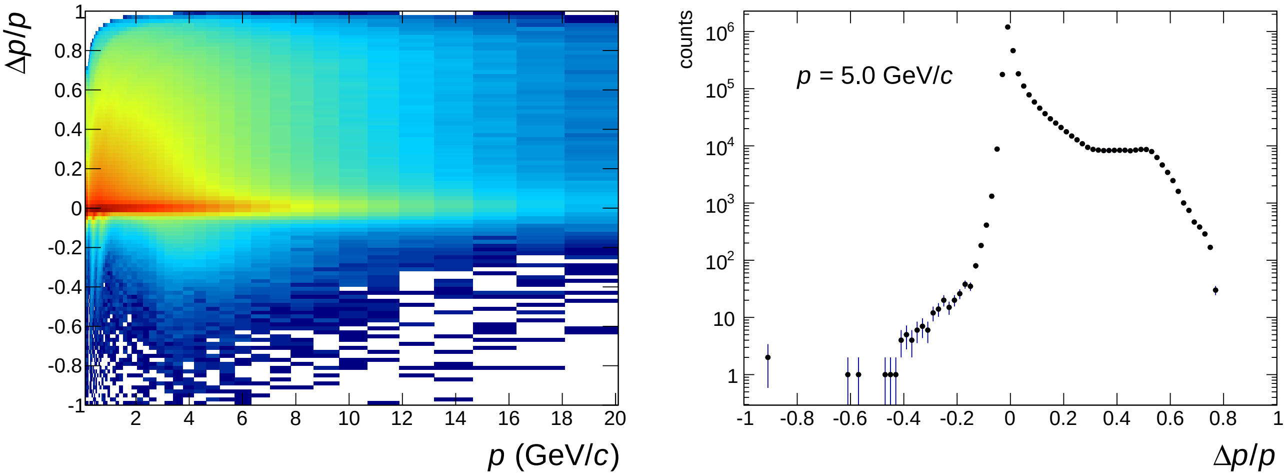

Figure 5.13.: Left: The distortion of electron momenta $\Delta p/p$ calculated with Eq. 5.26 as a function of the reconstructed electron momentum. Right: The projection of the momentum distortion for a given electron momentum of $p = 5$ GeV/c. [101]

On the right side of Figure 5.13, a projection on the $\Delta p/p$-axis is shown $p = 5$ GeV/c. The relative fraction of the momentum p is then subtracted from the electrons in this momentum range in the cocktail generator.

By applying this procedure on electrons, their momenta are automatically smeared also by the proper electron momentum resolution. The momentum resolution for fully reconstructed electrons is

$$\delta^e p_{\mathrm{T}} = p_{\mathrm{T}} \times \sqrt{0.004^2 + (0.012 * p_{\mathrm{T}})^2}. \tag{5.27}$$

2. As mentioned before, the mass spectrum is not corrected for the geometric acceptance. Therefore, all cocktail components are filtered through the kinematic acceptance cuts in this analysis, $p_{\mathrm{T}}^e > 0.2$ GeV/c and $|\eta^e| < 0.8$.

5.6.1. Hadron decays

Dielectrons originating from hadron decays were simulated with a fast MC generator. In order to obtain yields of the different dielectron sources, the transverse momentum distributions of

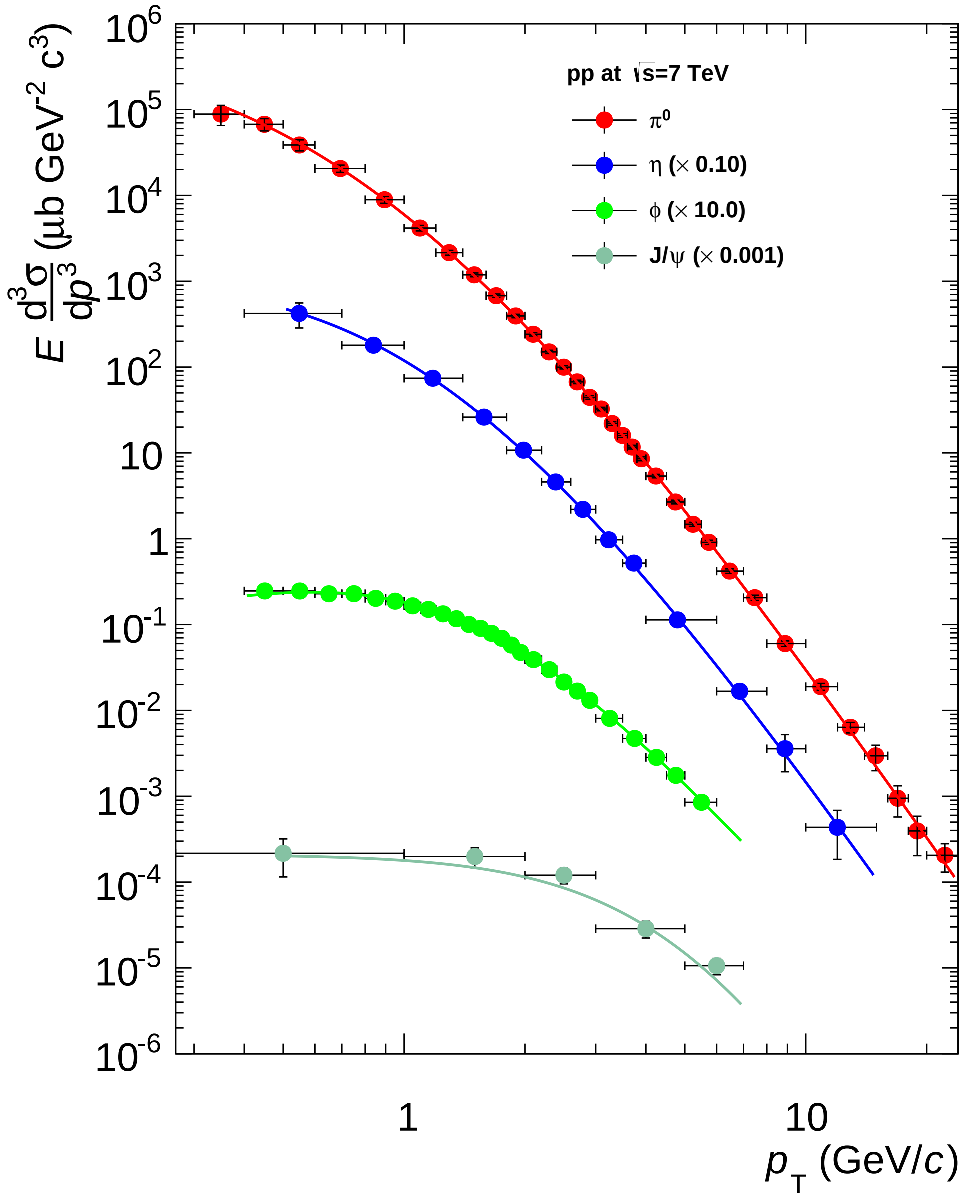

Figure 5.14.: The measured meson production cross sections are shown for π^0 and η [103], for ϕ [104] and J/ψ [94]. The lines represent the Tsallis fit functions [102], which were used as input for the cocktail.

measurements available at $\sqrt{s} = 7$ TeV are parametrised by a Tsallis function [102], which is given by

$$E\frac{\mathrm{d}^3\sigma}{\mathrm{d}p^3} = \frac{\sigma_{pp}^{\mathrm{INEL}}}{2\pi} A \frac{c \cdot (n-1)(n-2)}{nC[nC + m(n-2)]} \left(1 + \frac{m_{\mathrm{T}} - m}{nC}\right)^{-n}, \tag{5.28}$$

where A, C and n are the fit parameters and $\sigma_{pp}^{\mathrm{INEL}}$ the inelastic proton-proton cross section. The

meson rest mass is m and $m_{\mathrm{T}} = \sqrt{p_{\mathrm{T}}^2 + m^2}$ is the transverse mass.
The resulting parametrisations are shown together with the measured data points in Figure 5.14. The fit parameters are summarised in Table 5.4.

The resulting parametrisations determine the yield of the dielectron sources and the spectral shape of the cocktail. Contributions from the decays of other particles, which have not been measured, are estimated by m_{T} scaling of the π^0 cross section. For m_{T} scaling, the transverse momenta p_{T} in Eq. 5.28 are replaced by

Meson	A	C (GeV/c^2)	n
π^0	2.4 ± 0.15	0.132 ± 0.015	6.88 ± 0.007
η	0.21 ± 0.03	0.229 ± 0.021	7.0 ± 0.5
ϕ	$0.027 \pm 8.18 \times 10^{-4}$	0.271 ± 0.017	6.63 ± 0.73
J/ψ	$1.04 \times 10^{-4} \pm 2.53 \times 10^{-5}$	8963 ± 2	1.11 ± 0.25

Table 5.4.: Fit parameter of the Tsallis function for transverse momentum spectra of the mesons π^0, η, ϕ and J/ψ.

$$\sqrt{(p_{\mathrm{T}}/c)^2 + m_{\pi^0}^2 + m_h^2}, \tag{5.29}$$

where m_{π^0} and m_h are the mass of the π^0 and the hadron, respectively. The shape in p_{T} is fixed by the m_{T} scaling. In addition a relative normalisation to the π^0 cross section is achieved.
Once the yield is fixed, the shape of mass distributions depend on the decay kinematics and the branching ratios. The decay kinematics are based on the EXODUS cocktail generator. The branching ratios are taken from the particle data group [38]. The shape of the dielectron mass distribution from Dalitz decays is calculated by the Kroll-Wada equation, see Eq. 2.6. The form factors are taken from the Lepton-G Collaboration [105, 106]. The mass shape of the resonances is determined by the formalism of Gounaris and Sakurai [107].

5.6.2. Heavy flavour contribution

The contribution of semi-leptonic decays of open heavy-flavour hadrons, i.e. mostly D and B mesons, dominates the mass spectrum in the intermediate mass region.
In order to produce a realistic dielectron invariant mass spectrum from fast MC simulation, three input parameters are taken into account, which influence the mass spectrum:

1. The yield is given by the total cross sections for charm and beauty production for pp collisions at a collision energy of $\sqrt{s} = 7$ TeV. The total charm cross section was measured by the ALICE Collaboration [108] from hadronic open charm decays

$$\sigma_{\bar{c}c} = 8.5 \pm 0.5(\mathrm{stat.})^{+1.0}_{-2.4}(\mathrm{syst.}) \pm 0.1(\mathrm{BR.}) \pm 0.2(\mathrm{FF.}) \pm 0.3(\mathrm{lum.})^{+5.0}_{-0.4}(\mathrm{extr.})\ \mathrm{mb},$$

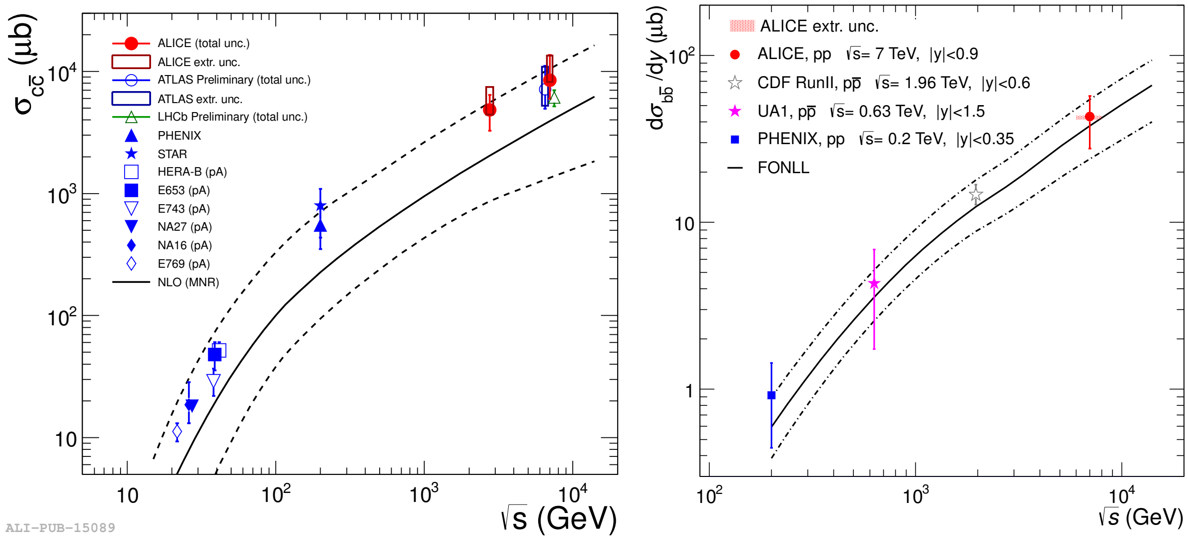

Figure 5.15.: The measured total charm cross section $\sigma_{c\bar{c}}$ (left panel) measured by the ALICE Collaboration [108] and the total beauty cross section $\mathrm{d}\sigma_{b\bar{b}}/\mathrm{d}y$ (right panel) measured by the ALICE Collaboration [111] as a function of collision energy is compared to next-to-leading-order calculations.

On the left side of Figure 5.15 the total charm cross section for pp collisions at $\sqrt{s} = 7$ TeV is shown as a function of the collision energy and compared to results from other experiments. At $\sqrt{s} = 7$ TeV the cross sections are shown for ATLAS [109] ($\sigma_{c\bar{c}} = 7.1^{+4.0}_{-2.2}$ mb) and for LHCb [110] ($\sigma_{c\bar{c}} = 6.1 \pm 0.9$ mb).

The total beauty cross section for pp collisions at $\sqrt{s} = 7$ TeV was measured by ALICE, see [111]. The result is a combination of the measurements of electrons from heavy-flavour hadrons and secondary J/ψ. The cross section is

$$\sigma_{b\bar{b}} = 281 \pm 34\ (\text{stat.})^{+53}_{-54}\ (\text{syst.})^{+7}_{-8}\ (\text{extr})\ \mu\text{b}.$$

On the right side of Figure 5.15 the beauty cross section at mid rapidity measured by ALICE is compared to other experiments and FONLL calculations [112] as a function of the collision energy.

2. The shape of the dielectron mass spectrum coming from a $c\bar{c}$ or $b\bar{b}$ pairs can be constrained by the single electron transverse momentum distribution. The transverse momentum spectra of electrons coming from open charm and beauty mesons is measured by the ALICE Collaboration [113]. This will be addressed in this following section.

3. Moreover, the correlation in $\Delta\varphi, \Delta\eta$ of heavy-flavour mesons to electrons coming from heavy-flavour hadron decays can be used to check the consistency of the heavy flavour kinematics of the cocktail and also constraint the kinematics. So far, to gain meaningful results the statistics of these analyses are too small.

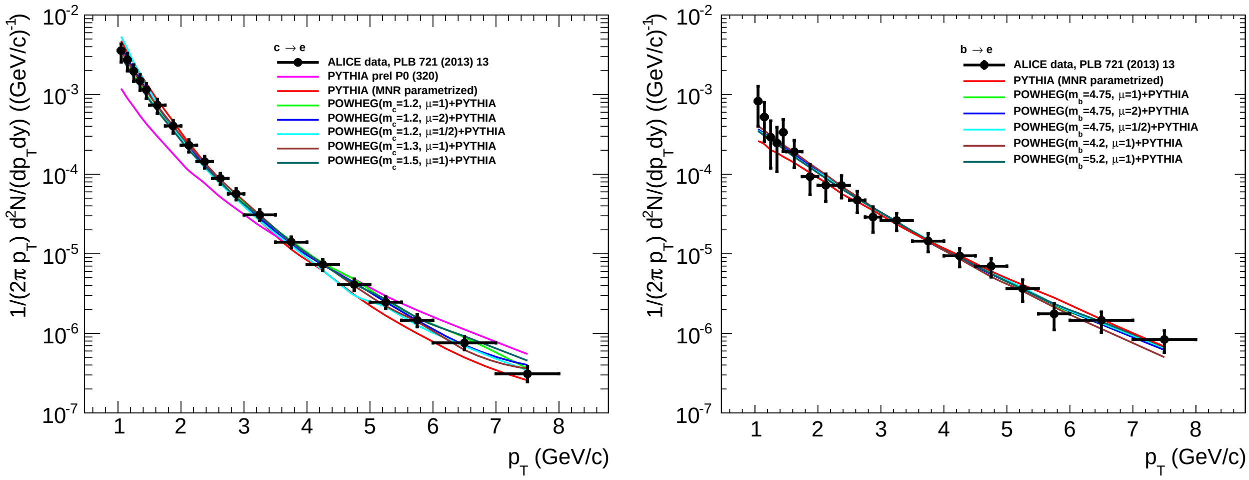

Figure 5.16.: Left: Measured single electron distributions from open charm (left panel) and open beauty (right panel) hadron decays as a function of transverse momentum p_{T}. [117]. The lines are NLO calculations from POWHEG fed into PYTHIA for fragmentation. See text for details.

The shape of the measured transverse momentum distribution of electrons is compared to LO and NLO MC simulation. The particle generation at LO is performed with PYTHIA [33]. PYTHIA simulations were parametrised[3] by NLO pQCD calculations by Mangano, Nason and Ridolfi [115]. In addition, a combination of the NLO particle generator POWHEG, see [116] for a recent review, and the LO shower MC PYTHIA is used. To generate realistic dielectron kinematics of semi-leptonic heavy-flavour decays, $c\bar{c}$ and $b\bar{b}$ pairs from POWHEG are fed into PYTHIA. PYTHIA is used as a fast simulation, which performs the particle fragmentation, showering and decays[4].

In Figure 5.16, the comparison of p_{T} spectra is shown for electrons from decays of heavy-flavour hadrons from a measurement [117] and from fast simulation. In the left panel electrons from charmed hadron decays are treated. In the right panel electrons from beauty open hadron decays are treated. All simulations reproduce the data within the uncertainties of the measurements.

In the case of processes including beauty flavour mesons, the situation is complicated. The oscillation of beauty flavours and the combination of first with second generation leptons can produce physical like-sign pairs:

- Neutral open beauty mesons B^0 and $\bar{B}^0$ undergo particle-antiparticle oscillation. The probability of such an oscillation is approximately 10 % [38]. Therefore, the combination of electrons from neutral open beauty mesons can produce a physical like-sign pair, if one of the beauty mesons underwent on oscillation.

---

[3] This parametrisation is also explained in detail in [114].

[4] An example for a configuration file for POWHEG is shown in the Appendix A.1. An example for a configuration file for a PYTHIA fast simulation in the AliRoot framework is shown using Appendix A.2.1 with POWHEG input and in A.2.2 for a fast simulation parametrised by [115]

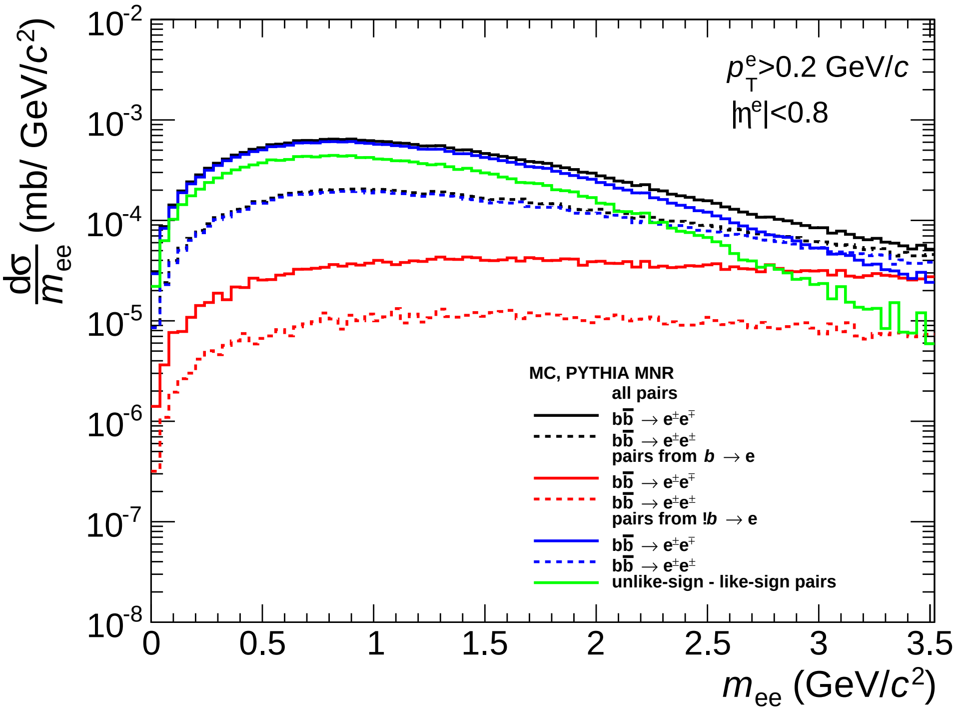

Figure 5.17.: Unlike-sign and like-sign dielectrons from open beauty meson decays for first generation electrons and second generation electrons as a function of the invariant mass. The contributions are normalised to the measured beauty cross section $\sigma_{b\bar{b}} = 281\ \mu$b, see [111]. The resulting unlike-sign mass distribution after subtraction of like-sign pairs is shown in green. [118]

- The second possibility to produce correlated like-sign dielectron pairs from open beauty mesons is due to the combination of leptons in first and second generation. First generation leptons come from a direct beauty decay $b \rightarrow e$, while second generation leptons are coming from a $b \rightarrow c \rightarrow e$ decay chain. A correlated like-sign pair can for example then be produced by

$$B^+ \rightarrow \bar{D}^0 e_1^+ \nu_e, \bar{D}^0 \rightarrow e_1^- X \quad (5.30)$$

$$B^- \rightarrow D^0 \pi^-, D^0 \rightarrow e_2^+, \quad (5.31)$$

  where $e_1^+ e_2^+$ form a correlated like-sign pair and, in addition, a correlated unlike-sign pair $e_1^- e_2^+$ is formed. This leads to an increase of the like-sign yield and a decrease of the unlike-sign yield. The branching ratios for $b \rightarrow e$ and $b \rightarrow c \rightarrow e$ is 11 % and 8 %, respectively [38].

Since only unlike-sign pairs are considered as physics signal here and because like-sign pairs are subtracted as shown in section 5.3, the same treatment needs to be applied for the cocktail contribution for electrons pairs coming from open beauty hadron decays.

In Figure 5.17, the unlike-sign pairs and the like-sign pairs are shown for dielectrons coming from

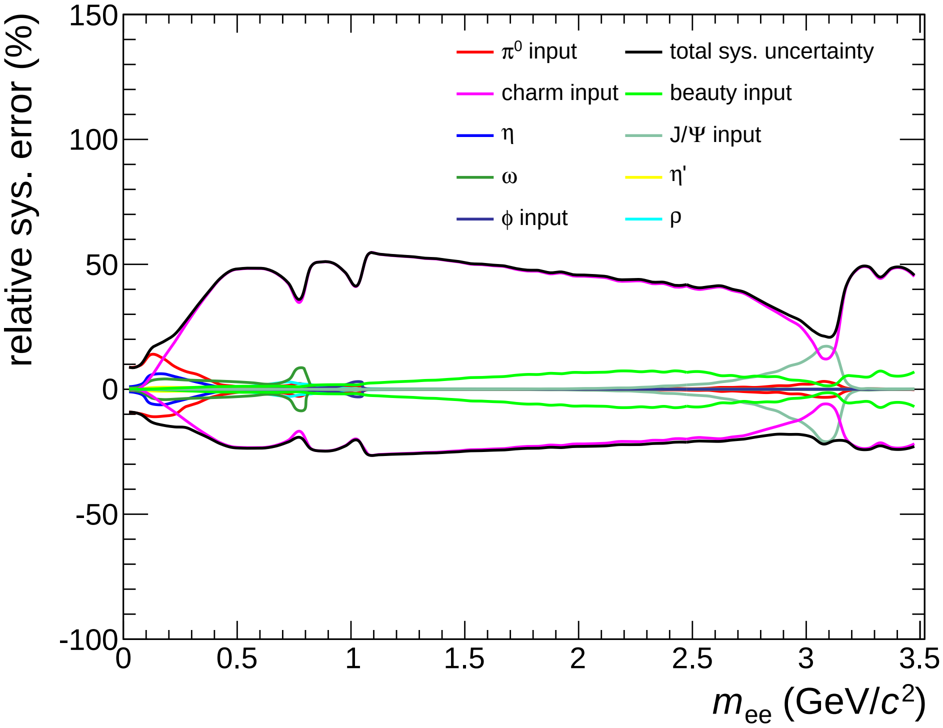

Figure 5.18.: Systematic uncertainty of the cocktail as a function of the invariant mass. The uncertainty arises from the systematic uncertainty of the cocktail input.

beauty mesons in their different decay chains. Dielectrons from first generation electrons are shown in red, while dielectrons from second generation electrons are shown in blue. The sum of all pairs is shown in black. Unlike-sign pairs are depicted by full lines, like-sign pairs by dashed lines.

For dielectrons from decays of open heavy charm hadrons, such a subtraction is not necessary since the $D\bar{D}$-oscillations [119, 38] and the like-sign contribution from their decay channels due to $D\bar{D}$ oscillations can be considered to be small [120].

Dielectrons from direct decays $b \to e$ have a harder mass distribution compared to dielectrons coming from decay chains $b \to c \to e$. The subtracted spectrum, which is used for the dielectron cocktail, is shown as the green line.

5.6.3. Systematic uncertainties

The input spectra of the cocktail contributions are measurements and therewith suffer from systematic uncertainties. The systematic uncertainties from the measurements lead to systematic uncertainties in the cocktail. To estimate these systematic uncertainties, the input spectra of the cocktail are shifted by their systematic uncertainties and refitted. The differences of these fits compared to the default fit are taken as systematic uncertainty of the various cocktail sources.

The systematic uncertainties of the charm and beauty contributions are taken from the systematic uncertainties from the measured cross sections, i.e. only a systematic uncertainty on the normalisation is considered. Systematic uncertainties of the beauty and charm contributions are considered

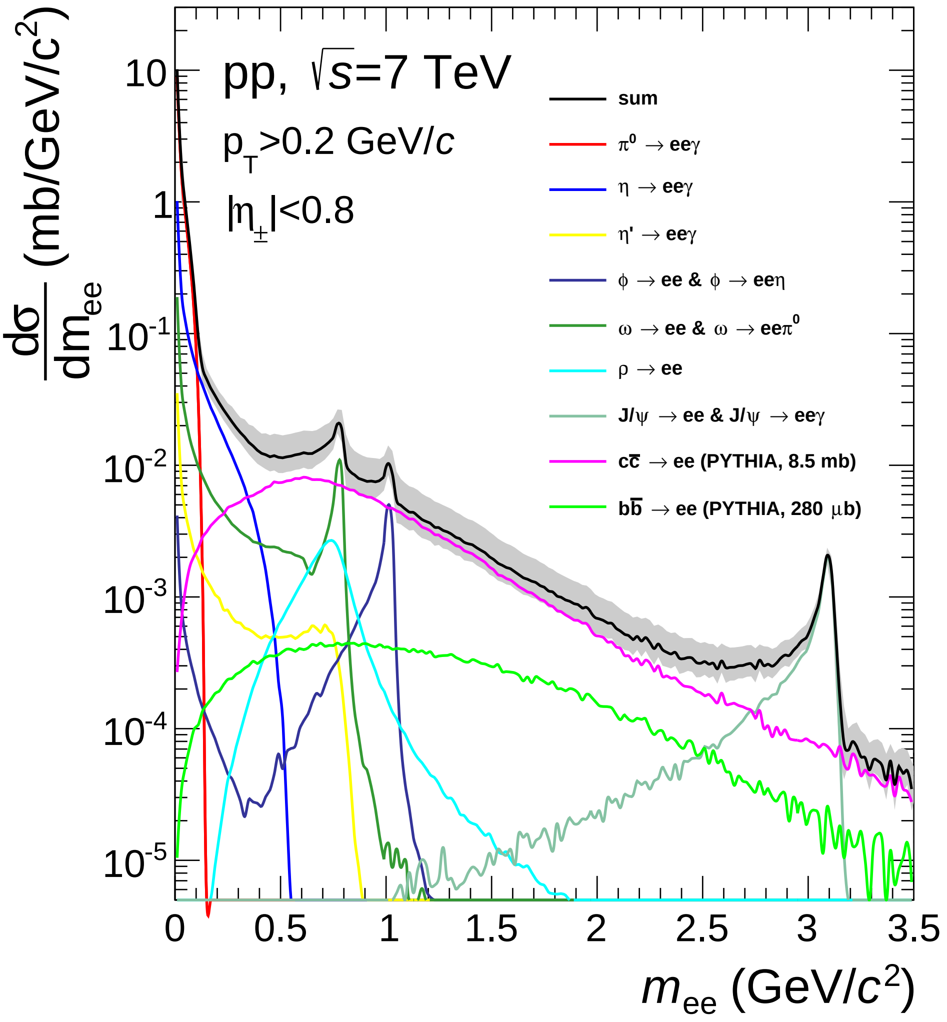

Figure 5.19.: The expected dielectron sources from hadron decays as a function of invariant mass for pp collisions at $\sqrt{s} = 7$ TeV. The sources are indicated in the legend. The band around the sum indicates the systematic uncertainty resulting from the input spectra.

uncorrelated and added quadratically.

The total systematic uncertainty of the cocktail is shown in Figure 5.18 together with the individual contributions. The contribution coming the charm continuum dominates over most of the mass range.

In Figure 5.19 the hadronic cocktail is shown as a function of the invariant dielectron mass. All expected dielectron sources from hadronic decays are indicated. The grey band around the sum represents the systematic uncertainty of the cocktail.

6. Results

The main results of the analysis are discussed in this chapter. In section 6.1, the fully corrected and absolutely normalised invariant mass-differential cross section for pp collisions at $\sqrt{s} = 7$ TeV is compared to the cocktail of dielectrons from hadronic sources in the mass range $0 < m_{ee} < 3.5$ GeV/c^2. In section 6.2, the cross section of direct photons is extracted via virtual photons as a function of the pair transverse momentum and compared to pQCD NLO calculations. The results are summarised in section 6.3.

6.1. Dielectron continuum in pp collisions at 7 TeV

The mass-differential dielectron cross section as a function of invariant mass $\frac{\mathrm{d}\sigma}{\mathrm{d}m_{ee}}$ is calculated, as

$$\frac{\mathrm{d}\sigma}{\mathrm{d}m_{ee}} = \frac{N_{ee}^{\mathrm{corr}}}{N_{\mathrm{MB}}\Delta m_{ee}} \times \sigma_{\mathrm{MB}}, \tag{6.1}$$

where N_{ee}^{corr} is the efficiency corrected yield of electrons, $N_{\mathrm{MB}}^{\mathrm{corr}}$ is the vertex reconstruction efficiency corrected number of minimum-bias events, Δm_{ee} is the bin width and σ_{MB} is the minimum-bias pp cross section.

$\frac{\mathrm{d}\sigma}{\mathrm{d}m_{ee}}$ is shown in Figure 6.1 and compared to the dielectron cocktail in the upper panel. The ratio of the data and the cocktail is shown in the lower panel. The cocktail is in reasonable agreement with data within the quoted statistical and systematic uncertainties.

In the mass region $m_{ee} > 1$ GeV/c^2 the data is nicely reproduced by the cocktail. The region, dominated by decays of open heavy flavour hadrons, shows a good description of the data, as well as the J/ψ resonance. However, in the low-mass region $0.4 < m_{ee} < 0.8$ GeV/c^2 a systematic difference between the data and the cocktail is visible. This mass region suffers from a low signal-over-background ratio and would be, therefore, sensitive to an over subtraction. Moreover, in this mass region the cocktail is dominated by charm decays. So an insufficient understanding of the combinatorial background or the charm contribution can lead to such a deviation.

6.2. Direct virtual photon production

Any source of real photons is also a source of virtual photons, which internally converts into a dilepton [36].

The advantage of measuring direct photons via dileptons compared to other methods is the possibility to measure simultaneously two observables, the invariant mass m_{ee} and the transverse

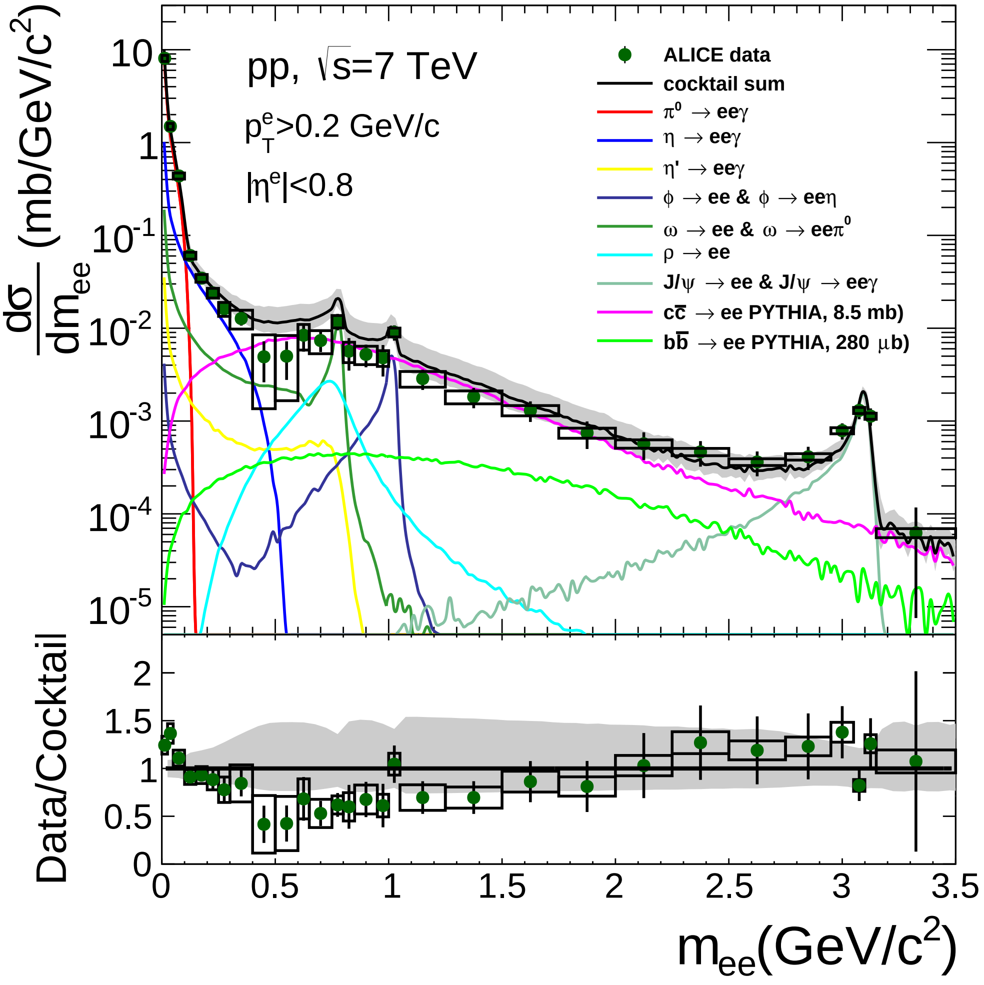

Figure 6.1.: Dielectron cross section as a function of the invariant mass. Statistical uncertainties are shown as error bars, systematic uncertainties of the data are shown as boxes. Dielectrons from the expected hadronic sources, i.e. the cocktail, are depicted as black line with the different contributions shown as coloured lines. The systematic uncertainty of the cocktail is shown as grey band. The lower panel shows the ratio between the data and the cocktail.

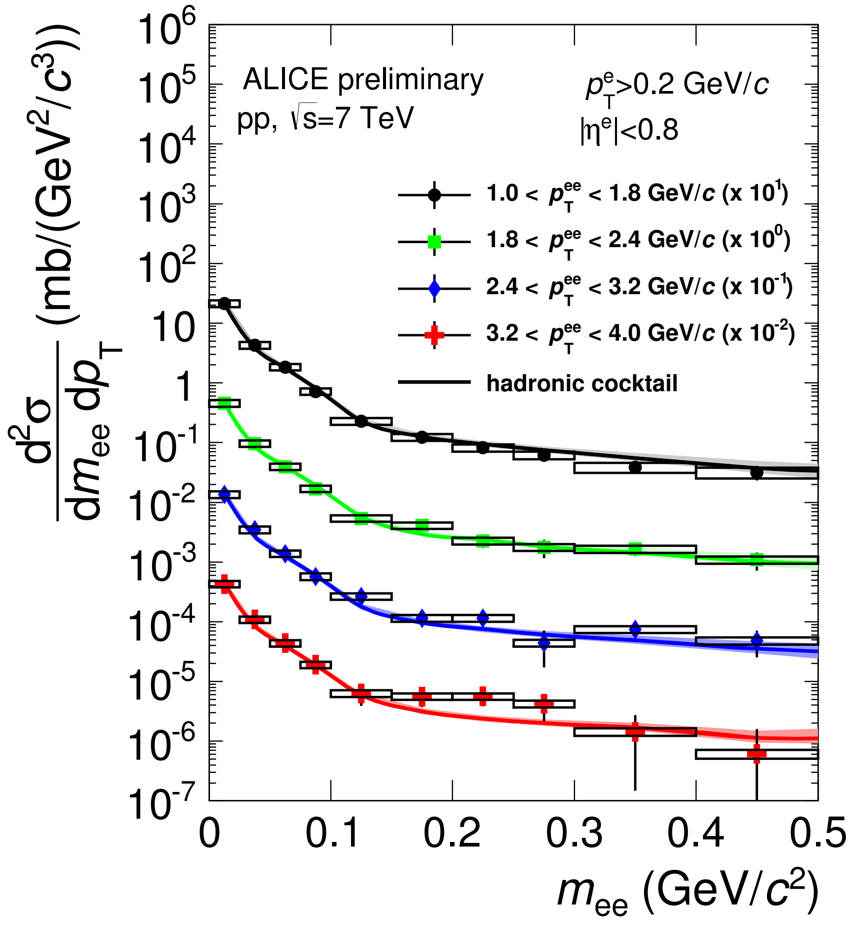

ALI-PREL-69060

Figure 6.2.: Comparison of data to the cocktail in several pair-p_{T} intervals in pp collisions at $\sqrt{s} = 7$ TeV.

momentum of the dielectron. Therefore, the rejection of photons from hadron decays, especially photons coming from the Dalitz decay of the π^0, is possible. The main background source in other approaches relying on the measurement of real photons can be rejected such that a significant reduction of the systematic uncertainty can be achieved.

In Figure 6.2, efficiency corrected data is compared to the cocktail within different pair-p_{T} ranges. Data is scaled to the cocktail in the mass region $m_{ee} < 0.025$ GeV$/c^2$ to minimize influences from normalization uncertainties. In the higher p_{T} regions, a small excess is visible for $m_{ee} \geq 0.15$ GeV$/c^2$. This excess can be identified as direct virtual photons, which are not included in the cocktail.

In the following section this excess is quantified as a function of the dielectron transverse momentum. The relation between the yield of virtual photons and the mass-differential dielectron yield is given by the Kroll-Wada equation, see Eq. 2.6. For the process of direct virtual photon production and

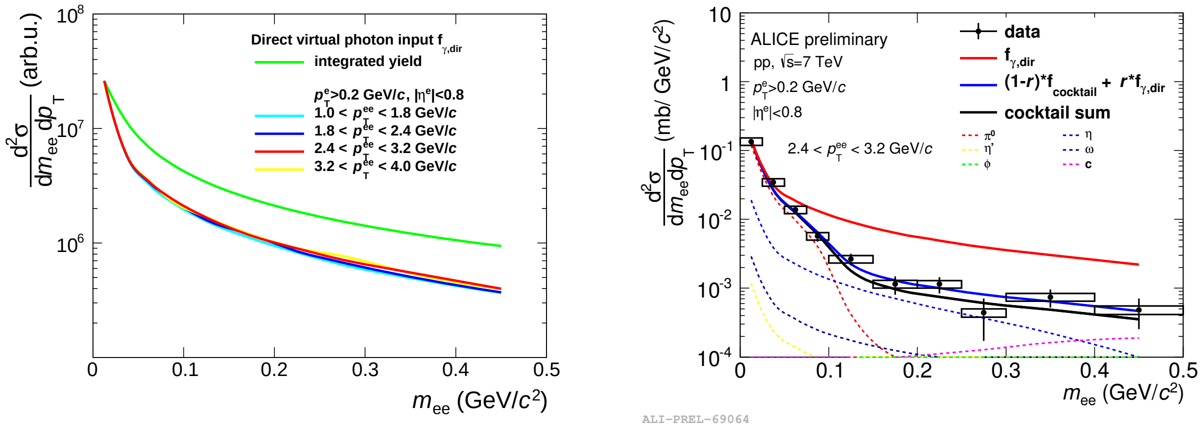

Figure 6.3.: Left: The green curve shows the pair-p_{T} integrated mass-differential yield of a heavy particle, which is forced to a Dalitz decay. The other curves are filtered by the acceptance $p_{\mathrm{T}}^{e} > 0.2$ GeV/c and $|\eta^{e}| < 0.8$. Each curve represents a pair-p_{T} interval. Right: The dielectron invariant mass distribution is shown for $2.4 < p_{\mathrm{T}}^{ee} < 3.2$ GeV/c and compared to the cocktail. The data points are fitted with Eq. 6.4.

$p_{\mathrm{T}}^{ee} \gg m_{ee}$, Eq. 2.6 becomes

$$\frac{1}{N_{\gamma}}\frac{\mathrm{d}N_{ee}}{dm_{ee}} = \frac{2\alpha_{\mathrm{e.m.}}}{3\pi}\sqrt{1-\frac{4m_e^2}{m_{ee}^2}}\left(1+\frac{2m_e^2}{m_{ee}^2}\right) \times \frac{1}{m_{ee}}, \tag{6.2}$$

where $\alpha_{\mathrm{e.m.}}$, m_e and m_{ee} are the fine structure constant, the electron rest mass and the dielectron invariant mass, respectively.

The direct virtual photon production in pp in Au–Au collisions was also measured by PHENIX and showed a good agreement with pQCD NLO calculations [121]. It was shown later [122], that direct photon differential cross section measurements from pp and $\bar{\mathrm{p}}\mathrm{p}$ collisions at mid-rapidity from various experiments followed a x_{T}-scaling, where

$$x_{\mathrm{T}} = \frac{2p_{\mathrm{T}}}{\sqrt{s}}. \tag{6.3}$$

p_{T} is the direct photon transverse momentum and $\sqrt{s}$ is the centre of mass collision energy.

The excess in the mass-differential dielectron spectra can be described by the sum of the cocktail and a theoretical direct photon mass distribution, which is given by the Kroll-Wada equation. The measured dielectron mass distribution is fitted with Eq. 6.4 in the mass range $0.1 < m_{ee} < 0.4$ GeV/c^2 to avoid influences from form factors of the Dalitz decay of the η meson.

The fit function

$$f_{\mathrm{combined}} = (1-r) * f_{\mathrm{cocktail}} + r * f_{\gamma,\mathrm{dir}}, \tag{6.4}$$

has two components, f_{cocktail} and $f_{\gamma,\mathrm{dir}}$, and one fit parameter r. The fit parameter r is the relative contribution of direct virtual photons to the inclusive dielectron yield. The fit component f_{cocktail} is

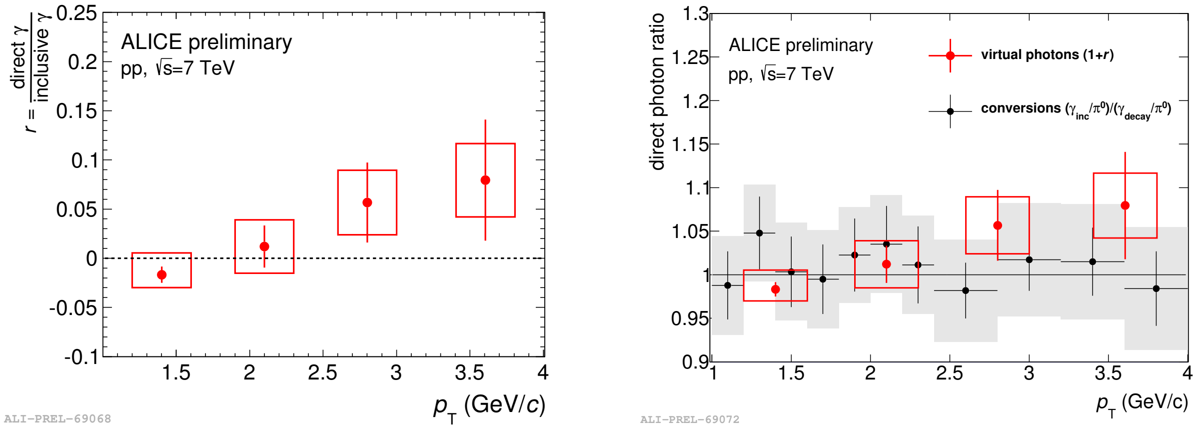

Figure 6.4.: Left: The fraction of direct in the inclusive virtual photon sample r as a function of p_{T}. Right: Comparison of direct virtual photon ratio $1 + r$ extracted from virtual photons compared to the double ratio $(\gamma_{\mathrm{inclusive}}/\pi^0)/(\gamma_{\mathrm{decay}}/\pi^0)$ extracted with the PCM. The two ratios are in good agreement.

the contribution of dielectrons from hadron decays and $f_{\gamma,\mathrm{dir}}$ is the contribution of virtual photons calculated via the Kroll-Wada equation. The component $f_{\gamma,\mathrm{dir}}$ is normalised to match the cocktail in the mass range $m_{ee} < 0.025$ GeV/c^2.

Since dielectrons are measured in the ALICE acceptance, $p_{\mathrm{T}}^{e} > 0.2$ GeV/c and $|\eta^{e}| < 0.8$, the same acceptance filter is applied for the contribution of the theoretical direct photon input.

This is done by a cocktail simulation of a heavy particle ($m_{ee} = 5$ GeV/c^2), which is forced to a Dalitz decay $X \rightarrow ee\gamma$. It is known from the Kroll-Wada equation, that the mass spectrum of such a particle decay follows a $1/m_{ee}$ shape in the low-mass region. The electrons from the decay, are filtered in the acceptance $p_{\mathrm{T}}^{e} > 0.2$ GeV/c and $|\eta^{e}| < 0.8$. On the left side of Figure 6.3, the initial dielectron mass distribution is shown as the red line. The dielectron mass distributions filtered in the acceptance for the different p_{T} intervals are included.

On the right side of Figure 6.3, an example fit using Eq. 6.4 is shown for the pair-p_{T} range $2.4 < p_{\mathrm{T}}^{ee} < 3.2$ GeV/c. The fit function describes the data and its excess over the hadronic very well, justifying the assumption of identifying the excess over the cocktail with direct virtual photons. The quality parameter of the fits χ^2/ndf are below 1 for all transverse momentum bins.

The systematic uncertainty of r is extracted from the systematic uncertainties of the initial mass spectra, which are shown in Figure 6.2. The invariant mass spectra are moved by their systematic uncertainties to the upper and lower edges allowed by the systematic uncertainties. This procedure holds for fully correlated systematic uncertainties. The systematic uncertainty of the cocktail is treated in the same way. This is done for all pair-p_{T} bins separately. The systematic uncertainty of the data and of the cocktail are added quadratically.

The resulting ratio of direct over inclusive virtual photons r as a function of pair transverse momentum is shown in Figure 6.4.

Under the assumption, that r is the same for real and virtual photons, i.e. $\gamma^{*}_{\mathrm{dir}}/\gamma^{*}_{\mathrm{incl}} = \gamma_{\mathrm{dir}}/\gamma_{\mathrm{incl}}$, the

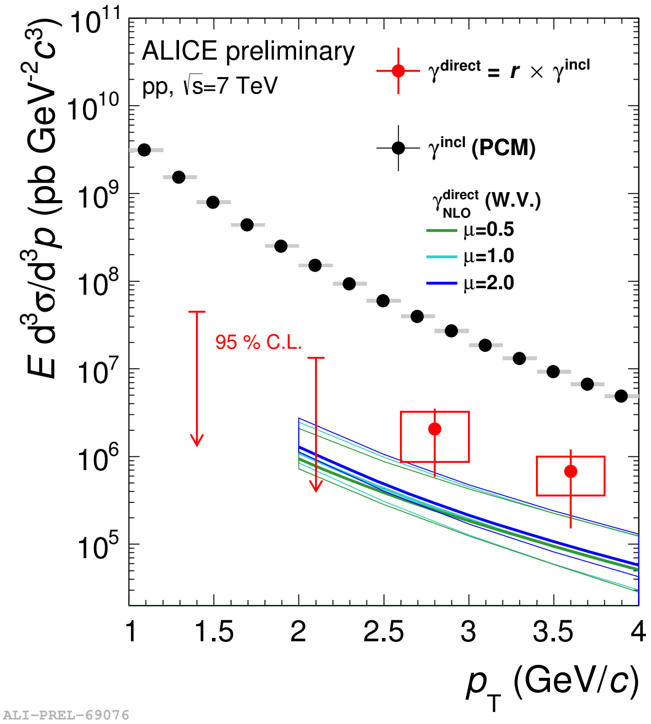

Figure 6.5.: p_T-differential cross section of direct real photon production for pp collisions at $\sqrt{s} = 7$ TeV in comparison with pQCD NLO calculations [123]. At low p_T only upper limits (95 % confidence level) can be determined as indicated by the arrows. In addition, the inclusive real photon cross section measured via photon conversions is shown.

fraction of direct real photons r can be transformed into the direct photon cross section, as follows

$$\sigma_\gamma^{\mathrm{dir}}(p_\mathrm{T}) = r \times \sigma_\gamma^{\mathrm{incl}}(p_\mathrm{T}), \tag{6.5}$$

where $\sigma_\gamma^{\mathrm{dir}}$, $\sigma_\gamma^{\mathrm{incl}}$ and r are the transverse momentum dependent values for the direct photon cross section, the inclusive photon cross section and the fraction of direct over inclusive real photons r. The real inclusive photon cross section $\sigma_\gamma^{\mathrm{incl}}$ was measured using the photon conversion method (PCM), see e.g. [124].

In Figure 6.5, the direct photon cross section calculated using Eq. 6.5 is shown together with the inclusive cross section measured via PCM as a function of transverse momentum. Additionally, pQCD NLO calculations [123] are compared with data using different values of the NLO scaling factor[1] $\mu = \{0.5; 1.0; 2.0\}$. At low transverse momentum, large systematic uncertainties of the calculations are substantial.

However, the measured direct photon cross section for pp collisions at $\sqrt{s} = 7$ TeV is in agreement with the theoretical calculations.

---

[1] It should be noted, that all involved scales, the renormalisation scale $\mu_{\mathrm{renormalization}}$ and the factorization scale $\mu_{\mathrm{factorization}}$ are set to a common value, i.e. $\mu = \mu_{\mathrm{renormalization}} = \mu_{\mathrm{factorization}}$.

6.3. Summary and conclusions

This thesis presented the analysis of the dielectron continuum in pp collisions at $\sqrt{s} = 7$ TeV. The data sample consists of 3.5×10^8 minimum-bias pp events recorded in 2010. The measured dielectron mass spectrum is described by the expected dielectron sources from hadronic decays in the mass range $0 < m_{ee} < 3.5$ GeV/c^2. An excess in the low-mass region $0.1 < m_{ee} < 0.4$ GeV/c^2 for high pair-p_{T} is identified by internal conversions of direct virtual photons. NLO pQCD calculations are in agreement to the measured p_{T}-differential cross section of direct real photons in the range $1 < p_{\mathrm{T}} < 4$ GeV/c.

The analysis provides a baseline for future dielectron measurement in ALICE.

7. Outlook

The presented dielectron analysis of the minimum-bias pp data sample of 2010 at $\sqrt{s} = 7$ TeV is only a first step of the ALICE dielectron program with the currently available data. This last chapter gives a brief outlook to planned dielectron analyses in the near and further future.

In addition to the 3.5×10^8 minimum-bias pp events used for this analysis, about 10^8 collisions more are recorded by ALICE in the 2010 run. Due to problems in the first reconstruction scheme, this data is only usable after a second reconstruction pass. The resulting statistics will reduce the statistical uncertainty and will allow to investigate dielectrons at higher mass.

Proton-proton data taking in 2011 focused on the triggering of rare probes. Of particular interest are data, in which single electrons were triggered with EMCal or TRD. The trigger threshold in transverse momentum for electrons was about 5 GeV/c for EMCal and about 2 GeV/c for TRD triggers. Dielectrons from these high-p_{T} electron samples can be used to access higher p_{T} and higher mass compared to minimum-bias triggered data. The measurement of high mass and high p_{T} dielectrons allows a better constraint for the cocktail contributions of the open heavy flavour continuum. The comparison of invariant mass and p_{T}^{ee} distributions of MC to data in mass regions dominated by the open heavy flavour continuum, i.e. charm in the mass region $1 < m_{ee} < 3$ GeV/c^2 and beauty in the mass region $3.3 < m_{ee} < 9.5$ GeV/c^2, would give important information for the mass shape of the dielectron mass continuum.

Single electron triggered events are perfectly suited to study the production mechanism of dielectrons from correlated open charm and open beauty pairs in the case of TRD triggered events and open beauty pairs in the case of EMCal triggered events. Also heavier quarkonia in the beauty sector, such as the Υ family, which currently is only measured with the forward muon spectrometer, can be expected to have a sufficient statistics in the triggered data samples and would be measurable via their dielectron decay channels down to zero pair p_{T}.

An important data sample for the dielectron measurement is the Pb–Pb data sample from 2011. Online compression of TPC clusters enabled the inspection of an integrated luminosity of 145 μb^{-1} at a centre of mass energy of $\sqrt{s_{\mathrm{NN}}} = 2.76$ TeV. This allows a systematic study of direct virtual photons emitted during the heavy-ion collision process. Thermal radiation is probably already accessible with this data sample and could extend the current understanding of the QGP.

To disentangle final-state effects in the hot and dense medium created in heavy-ion collisions from effects coming from the initial state, such as the modification of the nuclear parton distribution function of nuclei, an additional reference is necessary. This reference became available with the data taking of p–Pb collisions at $\sqrt{s_{\mathrm{NN}}} = 5.02$ TeV in 2012 and 2013. In the analysis of minimum-bias p–Pb collisions, the cocktail is consistent with the dielectron invariant mass spectra [125].

Consequently, the effects of the initial-state effects are small.

However, results on long-range correlations by ALICE [126] and ATLAS [127] in p–Pb collisions and in high-multiplicity pp collisions reported by CMS [128] show features, that are expected to be comparable with the collective expansion of a hot and dense medium. The systematic dielectron analysis of high multiplicity events in pp and p–Pb collisions would allow to extract informations of a fireball production already in lighter collision systems and bridge a gap from high multiplicity events in light collision systems to heavy-ion collisions.

The ALICE central barrel magnet can not only be operated with the nominal magnetic field of $B = 0.5$ T, but also with a lower magnetic field. Lowering the magnetic field would lead to an extension of the available dielectron phase space to lower pair p_{T}. Electrons with a transverse momentum lower than 0.4 GeV/c could fall into the TOF acceptance and profit from the electron identification capabilities of TOF [129].

Furthermore, physics beyond the study of the hot and dense medium can be addressed with dielectrons. Recent results showed, see e.g. [130], that also physics beyond the SM can be investigated. So-called dark photons are gauge bosons for dark gauge forces and could mix with SM particles. Dark photons could be detectable after the mixing into the SM sector via a conversion into a dilepton. An upper limit for the production of dark photons can be estimated by investigating the very low-mass dielectron region ($m_{ee} < 0.12$ GeV/c^2).

The internal conversion of dark photons could be detected by a sharp resonance determined by the mass resolution of the detector. Due to its excellent resolution, the ALICE detector would be well suited for such a measurement. First simulations from ALICE showed, that the combined data of pp, p–Pb and Pb–Pb collisions already taken in Run1 and expected for Run2 would allow to reduce the current upper limit estimate for dark photon production by a significant factor [131].

In 2015, the new data taking period Run2 will start. The expected integrated luminosity will increase by a factor of about four, so a significant reduction of the statistical uncertainty is expected for all collision systems. The increase of the statistics will be advantageous from many point of views. For now, the measurement of correlation of charmed hadron and electron suffers from a large statistical uncertainty. This measurement would be important to constrain the open heavy-flavour continuum in the cocktail on the pair level. The combination of this correlation measurement together with a precise dielectron cocktail comparison in the intermediate mass region would allow a new perspective on heavy-flavour production mechanisms.

Looking further into the future, after the second long shut-down of LHC, which is expected to end in 2018, ALICE will run with several upgraded detector components [132]. Of particular importance are the upgrades of the central barrel detectors ITS and TPC.

The upgrade of the ITS [133] will allow high precision vertexing, such that dielectrons from correlated open heavy-flavour decays can be rejected. This increases the signal-over-background ratio significantly in the mass region of interest. This is of great importance especially for the analysis of Pb–Pb collisions, where the dielectron continuum of correlated pairs from open heavy-flavour mesons is the dominant physical background in the low-mass region.

The continuous read-out in the upgraded TPC [134] will allow to take full advantage of the high luminosity at the upgraded LHC. The expected integrated luminosity for Run3 is expected to be a factor 100 times larger than in Run1 and Run2.

Systematic investigations in the mass region of the expected enhancement will profit from the rejection of this physical background and increase the signal-over-background ratio significantly. The increased integrated luminosity will allow multi-differential analysis of the contributions induced by the medium in the dielectron mass and transverse momentum spectra.

A. Leading-order and Next-to-leading-order Monte Carlo results of heavy flavour quark-antiquark pairs

A.1. POWHEG

In this appendix, an example for a configuration file is shown to produce $c\bar{c}$ pairs for proton-proton collisions at a collision energy of $\sqrt{s} = 7$ TeV with the POWHEG event generator [116]. The charm quark mass is set to $m_c = 1.3$ GeV/c^2 and the NLO scale parameter is $\mu = 1$. It should be noted, that throughout this chapter, all involved scales, the renormalisation scale $\mu_{\text{renormalization}}$ and the factorization scale $\mu_{\text{factorization}}$ are set to a common value, i.e. $\mu = \mu_{\text{renormalization}} = \mu_{\text{factorization}}$. Systematic results on quark level with different parameter settings are shown in section A.1.2.

A.1.1. Configuration files

```
 !randomseed 352345 ! uncomment to set the random seed to a value of your choice.
                   ! It generates the call RM48IN(352345,0,0) (see the RM48 manual).
                   ! THIS MAY ONLY AFFECTS THE GENERATION OF POWHEG EVENTS!
                   ! If POWHEG is interfaced to a shower MC, refer to the shower MC
                   ! documentation to set its seed.

!Heavy flavour production parameters
numevts 100000   ! default number of events to be generated
ih1   1        ! hadron 1 (1 -> proton)
ih2   1        ! hadron 2 (1 -> proton)
lhans1  10550         ! pdf set for hadron 1 (LHA numbering)
lhans2  10550         ! pdf set for hadron 2 (LHA numbering)
ebeam1 3500    ! energy of beam 1
ebeam2 3500    ! energy of beam 2
qmass  1.3     ! mass of heavy quark in GeV
facscfact 1    ! factorization scale factor: mufact=muref*facscfact
renscfact 1    ! renormalization scale factor: muren=muref*renscfact
#fixedscale 1    ! use ref. scale=qmass (default 0, use running scale)

! Parameters to allow-disallow use of stored data
use-old-grid 1    ! if 1 use old grid if file pwggrids.dat is present (# 1: regenerate)
use-old-ubound 1  ! if 1 use norm of upper bounding function stored in pwgubound.dat, if present; # 1: regenerate

ncall1 50000   ! number of calls for initializing the integration grid
itmx1 5        ! number of iterations for initializing the integration grid
ncall2 100000  ! number of calls for computing the integral and finding upper bound
itmx2 5        ! number of iterations for computing the integral and finding upper bound
foldcsi   5      ! number of folds on x integration
foldy   5      ! number of folds on y integration
foldphi 1      ! number of folds on phi integration
nubound 500000  ! number of bbarra calls to setup norm of upper bounding function
```

```
iymax 1         ! <= 10, normalization of upper bounding function in iunorm X iunorm square in y
      , log(m2qq)
ixmax 1         ! <= 10, normalization of upper bounding function in iunorm X iunorm square in y
      , log(m2qq)
xupbound 2       ! increase upper bound for radiation generation
```

A.1.2. Results from POWHEG on quark level

In Figure A.1, examples for Feynman diagrams for the production processes in NLO are shown. In Figure A.2 and Figure A.3 results from POWHEG on generator level are shown for charm and beauty quark distributions, respectively. On the left side the NLO scaling parameter μ is varied in the range $\{0.5; 1.0; 2.0\}$, on the right side the quark mass is varied in the range $\{1.2; 1.3; 1.5\}$ GeV/c^2 and $\{4.2; 4.75; 5.2\}$ GeV/c^2 for charm and beauty quarks, respectively.

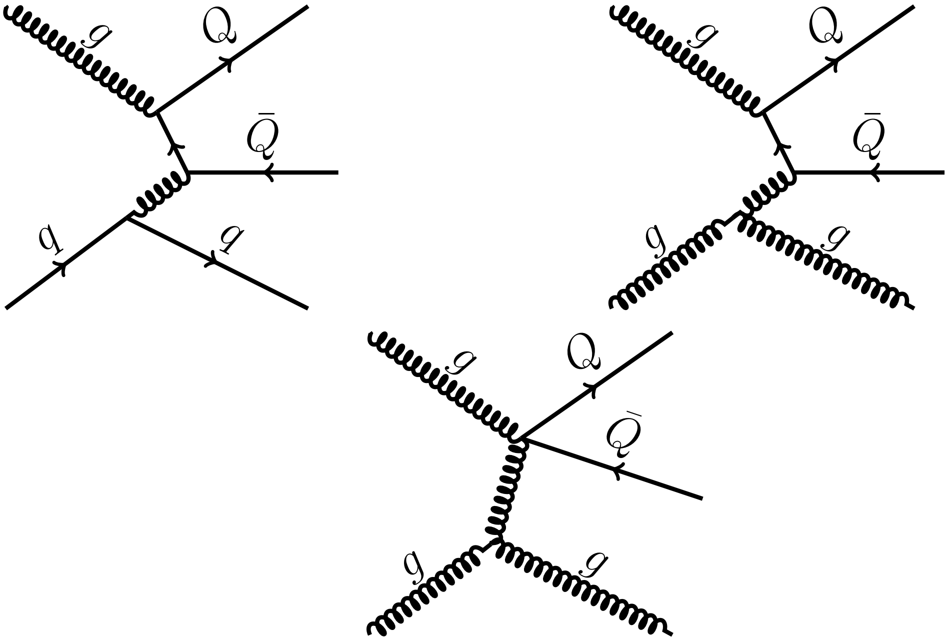

Figure A.1.: Examples of Feynman diagrams for NLO processes contributing to the production of heavy flavour quark-antiquark pairs.

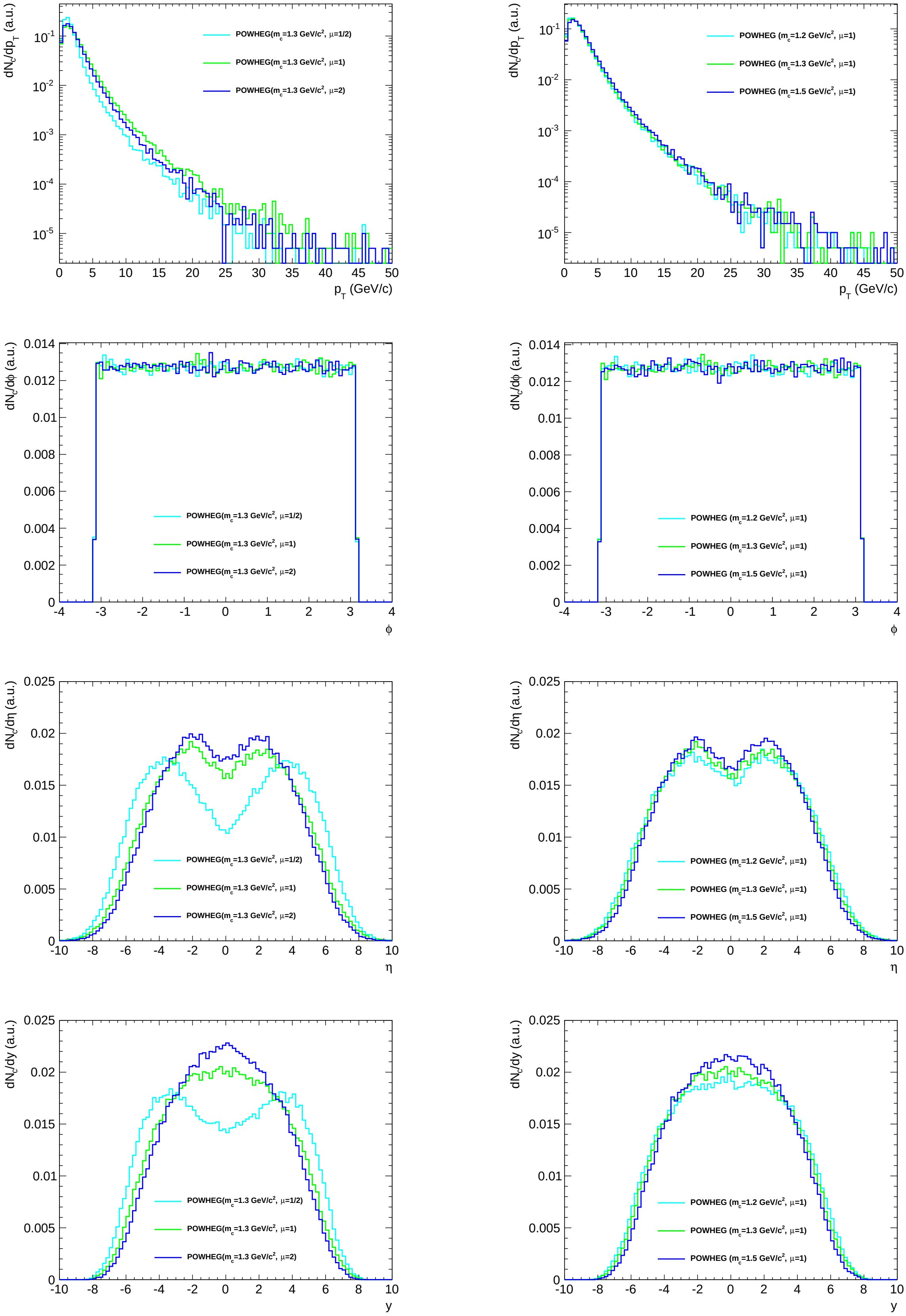

Figure A.2.: Charm quark distributions. The NLO scale parameter μ is varied in the four plots on the left panel, the charm quark mass m_c in the four plots on the right panel.

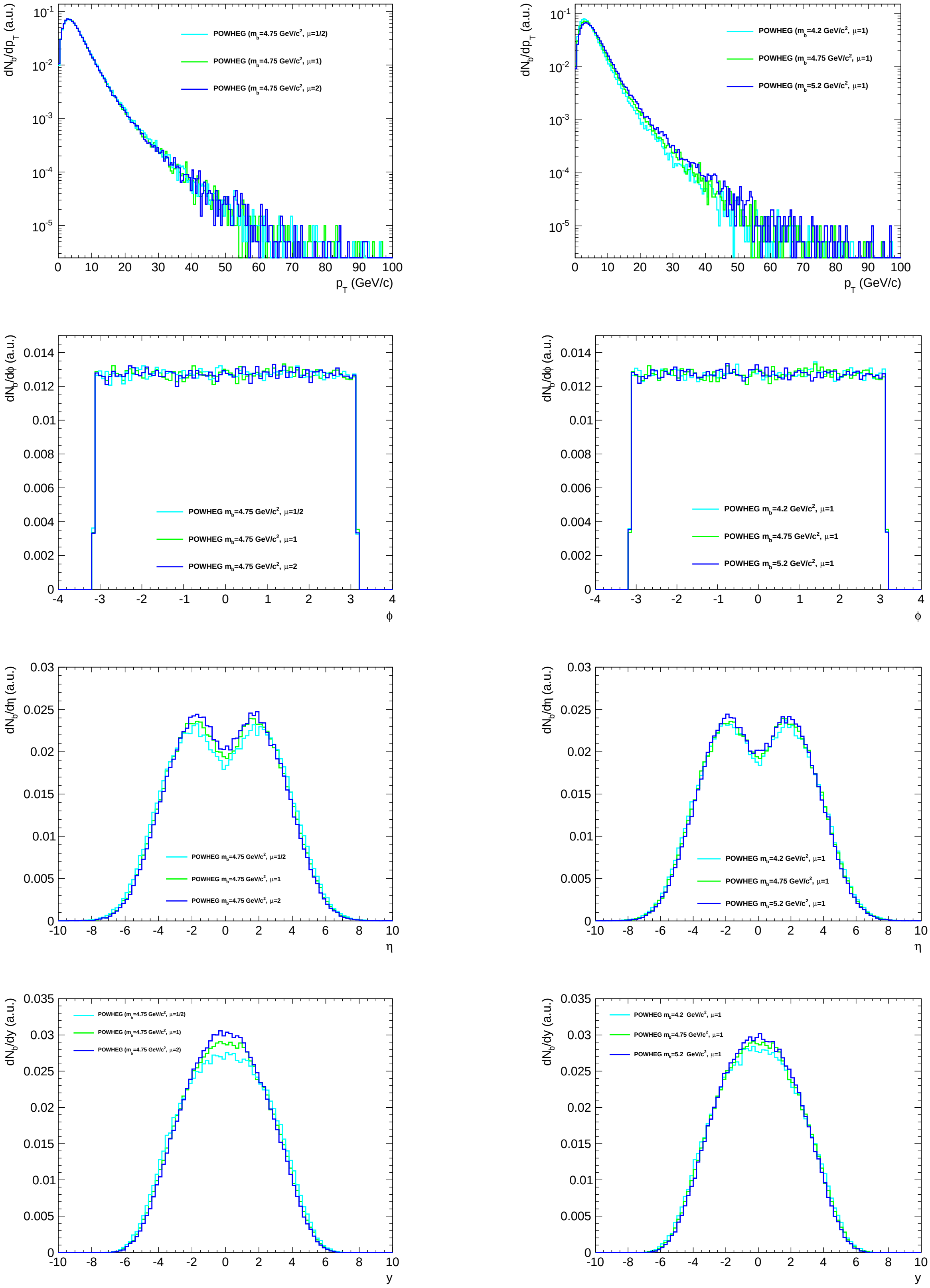

Figure A.3.: Beauty quark distributions. The NLO scale parameter μ is varied in the four plots on the left panel, the beauty quark mass m_b in the four plots in the right panel.

A.2. PYTHIA

In this section, configuration files are shown to generate events including $c\bar{c}$ pairs with PYTHIA within the AliRoot framework.

In appendix A.2.1, an example for a configuration file is shown, in which a heavy flavour quark-antiquark pair generated by POWHEG, is embedded into a PYTHIA event. The process `kPyCharmPWHG` indicates, that $c\bar{c}$ pairs are read from POWHEG. The command `SetReadLHEF` reads the lhe file[1] Fast simulations produced with this method are used as a cross check for the open heavy-flavour continuum in the cocktail, see e.g. Figure 5.16.

In appendix A.2.2, a configuration file for the generation of pp events is shown, which are parametrized to NLO calculations from MNR [115]. To reach an excellent agreement between the PYTHIA simulation and the NLO calculations [115], an additional normalization on the initial transverse momentum $p_{\mathrm{T}}^{\mathrm{hard}}$, i.e. `SetPtHard(`$p_{\mathrm{T,min}}^{\mathrm{hard}}$`,`$p_{\mathrm{T,max}}^{\mathrm{hard}}$`)`, for the heavy-flavour quarks has to be applied, see [114]. Due to the good acceptance of ALICE in the low-momentum regime, this is of essential interest for ALICE simulations.

A.2.1. Configuration file with POWHEG input

```
AliGenPythia* pythia = new AliGenPythia(-1);
pythia->SetMomentumRange(0, 999999.);
pythia->SetThetaRange(0., 180.);
pythia->SetYRange(-1.,1.);
pythia->SetPtRange(0,1000.);

pythia->SetProcess(kPyCharmPWHG); //set POWHEG output usage
pythia->SetReadLHEF(<lhe-file>);  //read POWHEG result

pythia->SetEnergyCMS(energy);
pythia->SetForceDecay(kSemiElectronic);
return pythia;
```

A.2.2. Configuration file for charm pairs in PYTHIA with MNR parametrisation

```
Int_t ran = gRandom->Integer(100);

AliGenPythia* pythia = new AliGenPythia(-1);
pythia->SetMomentumRange(0, 999999.);
pythia->SetThetaRange(0., 180.);
pythia->SetYRange(-1.,1.);
pythia->SetPtRange(0,1000.);
pythia->SetProcess(kPyCharmppMNRwmi);
pythia->SetEnergyCMS(energy);

if(ran>0 && ran<=25)       {pythia->SetPtHard(2.76,3.);}
else if(ran>25 && ran<=65) {pythia->SetPtHard(3.00001,4.);}
else if(ran>65 && ran<=93) {pythia->SetPtHard(4.00001,8.);}
else if(ran>93)            {pythia->SetPtHard(8.00001,1000.);}
```

---

[1] The results from POWHEG are produced in the lhe file format, i.e. the Les Houches Event format, which has a XML-style structure. See e.g. [135] for more information.

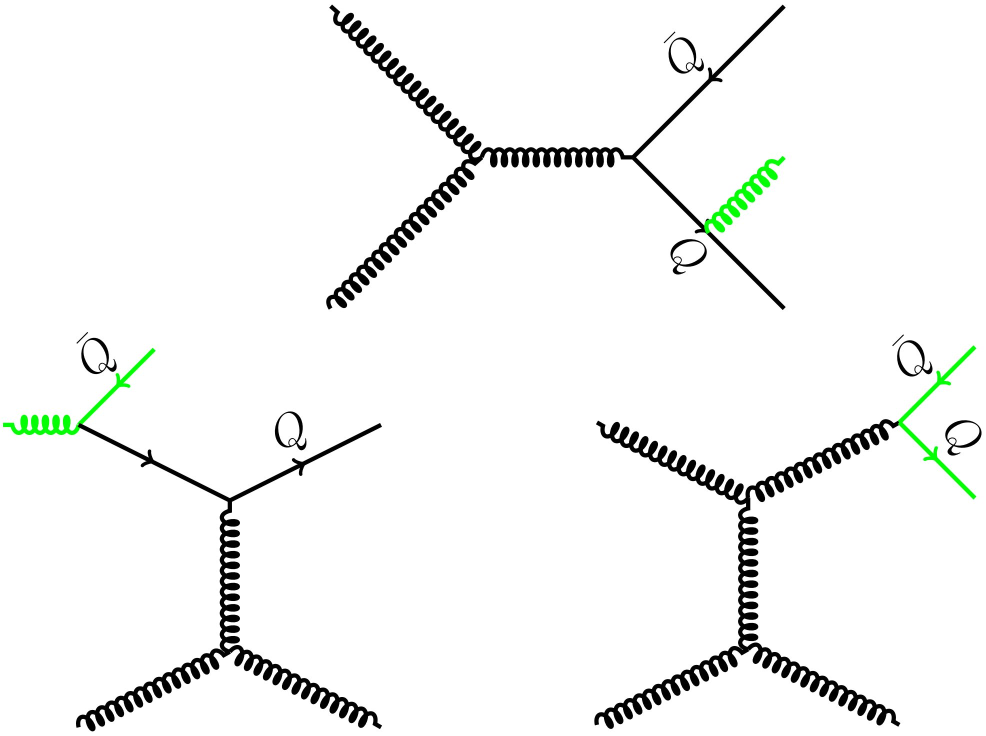

Figure A.4.: Example for Feynman diagrams of pair creation (upper plot), flavour excitation (lower left), gluon splitting (lower right). The black lines correspond to the hard processes, the green line to the parton shower.

```

    pythia->SetForceDecay(kSemiElectronic);
    return pythia;
```

The heavy-flavour continuum contribution to the cocktail used in this analysis is generated with the PYTHIA event generator tuned on NLO calculations, described in [115]. In PYTHIA, heavy-flavour production processes are divided into three classes, depending on the number of heavy-flavour quarks produced in the LO hard scattering process.

gluon splitting No heavy quark is involved in the hard scattering. The heavy quark is produced by a $g \to Q\bar{Q}$ shower in initial or final state.

flavour excitation A heavy quark coming from an initial state gluon splitting in the incoming hadron is put on mass shell via scattering with a parton from the second hadron.

pair creation The two heavy quarks are generated in the final state by quark anti-quark or gluon annihilation.

In Figure A.4, examples for Feynman diagrams for the three classes are shown.

Bibliography

[1] D. Gross and F. Wilczek *Phys. Rev. Lett.*, vol. 30, p. 1343, 1973.

[2] E. Shuryak *Phys. Lett. B*, vol. 78, p. 150, 1978.

[3] P. Braun-Munzinger and J. Wambach *Rev. Mod. Phys.*, vol. 81, p. 1031, 2008.

[4] F. Englert and R. Brout *Phys. Rev. Lett.*, vol. 13, p. 321, 1964.

[5] P. Higgs *Phys. Lett.*, vol. 12, p. 132, 1964.

[6] ATLAS Collaboration *Phys. Lett. B*, vol. 716, p. 1, 2012.

[7] CMS Collaboration *Phys. Lett. B*, vol. 716, p. 30, 2012.

[8] W. Pauli *Phys. Rev.*, vol. 58, p. 716, 1940.

[9] J. Beringer *et al. Phys. Rev. D*, vol. 86, p. 010001, 2012.

[10] Particle Data Group *Phys. Rev. D*, vol. 86, p. 010001, 2012.

[11] R. Hagedorn *Nuovo Cim. Suppl.*, vol. 3, p. 147, 1965.

[12] N. Cabibbo and G. Parisi *Phys. Lett. B*, vol. 59, p. 67, 1975.

[13] V. Koch *Int.J.Mod.Phys. E*, vol. 6, p. 203, 1997.

[14] M. Alford, K. Rajagopal, T. Schaefer, and A. Schmitt *Rev. Mod. Phys.*, vol. 80, p. 1455, 2008.

[15] F. Karsch *Lect. Notes Phys.*, vol. 583, p. 209, 2002.

[16] A. Andronic, P. Braun-Munzinger, and J. Stachel *Nucl. Phys. A*, vol. 834, p. 237c, 2010.

[17] Z. Fodor and S. Katz *JHEP*, vol. 0404, p. 050, 2004.

[18] M. Miller, K. Reygers, S. Sanders, and P. Steinberg *Ann. Rev. Nucl. Part. Sci.*, vol. 57, p. 205, 2007.

[19] ALICE Collaboration *Phys. Lett. B*, vol. 696, p. 30, 2011.

[20] STAR Collaboration *Phys. Rev. Lett.*, vol. 91, p. 172302, 2003.

[21] PHENIX Collaboration *Phys. Rev. C*, vol. 69, p. 034910., 2004.

[22] ALICE Collaboration *Eur. Phys. J. C*, vol. 73, p. 2662, 2013.

[23] STAR Collaboration *Phys. Rev. C*, vol. 77, p. 054901, 2008.

[24] M. Luzum and P. Romatschke *Phys. Rev. C*, vol. 78, p. 034915, 2008. Erratum-ibid.C79:039903,2009.

[25] M. Gyullasy and L. McLerran *Nucl. Phys. A*, vol. 750, p. 30, 2005.

[26] P. Kovtun, D. Son, and A. Starinets *Phys. Rev. Lett.*, vol. 94, p. 111601, 2005.

[27] STAR Collaboration *Phys. Rev. C*, vol. 77, p. 054901, 2008.

[28] J.-Y. Ollitrault, A. M. Poskanzer, and S. A. Voloshin *Phys. Rev. C*, vol. 80, p. 014904, 2009.

[29] L. McLerran and R. Venugopalan *Phys. Rev. D*, vol. 49, p. 2233, 1994.

[30] L. McLerran *Int. J. Mod. Phys. A*, vol. 25, p. 5847, 2010.

[31] CMS Collaboration *Phys. Lett. B*, vol. 718, p. 773, 2013.

[32] X.-N. Wang, Z. Huang, and I. Sarcevic *Phys. Rev. Lett.*, vol. 77, p. 231, 1996.

[33] T. Sjostrand, S. Mrenna and P. Skands *JHEP*, vol. 05, p. 026, 2006.

[34] I. P. Lokhtin and A. M. Snigirev *Eur. Phys. J. C*, vol. 45, p. 211, 2006.

[35] R. Dalitz *Proc. Phys. Soc. (London)*, vol. A64, p. 667, 1951.

[36] N. Kroll and W. Wada *Phys. Rev.*, vol. 98, p. 1355, 1955.

[37] ALICE Collaboration *CERN-PH-EP-2014-088*, 2014.

[38] Particle Data Group *J. Phys. G*, vol. 37, p. 075021, 2010.

[39] J. Sakurai in *Currents and Mesons* (C. University of Chicago Press, ed.), 1969.

[40] R. Rapp, J. Wambach, and H. van Hees in *Relativistic Heavy-Ion Physics* (R. Stock and Landolt Bornstein (Springer), eds.), New Series I/23A, 2010.

[41] R. Rapp and J. Wambach *Adv. Nucl. Phys.*, vol. 1, p. 25, 2000.

[42] G. E. Brown and M. Rho *Phys. Rev. Lett.*, vol. 66, p. 2720, 1991.

[43] T. Matsui and H. Satz *Phys. Lett. B*, vol. 178, p. 416, 1986.

[44] S. D. Drell and T. M. Yan *Phys. Rev. Lett.*, vol. 25, p. 316, 1970.

[45] S. D. Drell and T. M. Yan *Ann. Phys.*, vol. 24, p. 181, 1971.

[46] DLS Collaboration *Phys. Rev. C*, vol. 57, p. 1865, 1998.

[47] DLS Collaboration *Phys. Rev. Lett.*, vol. 79, p. 1229, 1997.

[48] HADES Collaboration *Eur. Phys. J.*, vol. A 41, p. 243, 2009.

[49] HADES Collaboration *Phys. Lett. B*, vol. 663, p. 43, 2008.

[50] HADES Collaboration *Phys. Lett. B*, vol. 690, p. 118, 2010.

[51] CERES Collaboration *Phys. Lett. B*, vol. 666, p. 425, 2008.

[52] H. van Hees and R. Rapp *Nucl. Phys. A*, vol. 806, p. 339, 2008.

[53] J. Ruppert, C. Gale, T. Renk, P. Lichard, and J. Kapusta *Phys. Rev. Lett*, vol. 100, p. 162301, 2008.

[54] K. Dusling, D. Teaney, and I. Zahed *Phys. Rev.*, vol. C 75, p. 024908, 2007.

[55] NA60 Collaboration *Eur. Phys. J. C*, vol. 59, p. 607, 2009.

[56] NA60 Collaboration *Phys. Rev. Lett.*, vol. 96, p. 162302, 2006.

[57] PHENIX Collaboration *Phys. Lett. B*, vol. 670, p. 313, 2009.

[58] STAR Collaboration *arXiv:1312.7397 [hep-ex], submitted to Phys. Rev. Lett.*, 2013.

[59] W. Llope (for the STAR Collaboration) *Nucl. Instr. Meth. A*, vol. 661, p. S110, 2012.

[60] STAR Collaboration *Phys. Rev. C*, vol. 86, p. 024906, 2012.

[61] PHENIX Collaboration *Phys. Rev. C*, vol. 81, p. 034911, 2010.

[62] R. Rapp *AIP Conf. Proc.*, vol. 1322, p. 55, 2010.

[63] F. Geurts (for the PHENIX Collaboration) *Nucl. Phys. A*, vol. 904-905, p. 217c, 2013.

[64] L. Evans and P. Bryant *JINST*, vol. 3, p. S08001, 2008.

[65] ALICE Collaboration *JINST*, vol. 3, p. S08002, 2008.

[66] ATLAS Collaboration *JINST*, vol. 3, p. S08003, 2008.

[67] CMS Collaboration *JINST*, vol. 3, p. S08004, 2008.

[68] LHCb Collaboration *JINST*, vol. 3, p. S08005, 2008.

[69] ALICE Collaboration *J. Phys. G*, vol. 30, p. 1517, 2004.

[70] ALICE Collaboration *J. Phys. G*, vol. 32, p. 1295, 2006.

[71] *ALICE Inner Tracking System (ITS): Technical Design Report*. Technical Design Report ALICE, Geneva: CERN, 1999.

[72] *ALICE Time Projection Chamber (TPC): Technical Design Report*. Technical Design Report ALICE, Geneva: CERN, 2000.

[73] ALICE TPC Collaboration *Nucl. Instr. Meth. A*, vol. 622, p. 316, 2010.

[74] W. Blum, W. Riegler, and L. Rolandi in *Particle Detection with Drift Chambers* (Springer-Verlag, ed.), 2008.

[75] G. Charpak, R. Bouclier, T. Bressani, J. Favier, and C. Zupancic *Nucl. Instr. Meth. A*, vol. 62, p. 262, 1968.

[76] *ALICE transition-radiation detector (TRD): Technical Design Report*. Technical Design Report ALICE, Geneva: CERN, 2001.

[77] *ALICE Time-Of-Flight system (TOF): Technical Design Report*. Technical Design Report ALICE, Geneva: CERN, 2000.

[78] E. Cerron-Zeballos, I. Crotty, D. Hatzifotiadou, J. L. Valverde, S. Neupane, M. Williams, and A. Zichichi *Nucl. Instr. Meth. A*, vol. 374, p. 132, 1996.

[79] ALICE Collaboration *CERN-LHCC-2008-014. ALICE-TDR-14*, 2008.

[80] J. Kim, M. C. Nemes, A. de Toledo Piza, and H. Borges *Phys. Rev. Lett.*, vol. 77, p. 207, 1996.

[81] *The Technical Design Report of the Trigger, Data-Acquisition, High Level Trigger, and Control System,*. Technical Design Report ALICE, Geneva: CERN, 2003.

[82] ALICE Collaboration *CERN-LHCC-2005-018. ALICE-TDR-12*, 2005.

[83] R. Kalman *Transactions of the ASME- J. Basic Engineering*, vol. 82, p. 35, 1960.

[84] D. Huffman *Proceedings of the I.R.E.*, vol. 21, p. 514, 1952.

[85] Y. Belikov, M. Ivanov, K. Safarik, and J. Bracinik *arXiv:physics/0306108 [physics.data-an]*, 2003.

[86] G. Grastveit *et al. CHEP 2003 Proceeding, arXiv:physics/0306017*, 2003.

[87] X. N. Wang and M. Gyulassy *Phys. Rev. Lett.*, vol. 68, p. 1480, 1992.

[88] M. Richter *private communication*.

[89] J. Jowett *et al. CERN-ATS-2011-143*, 2011.

[90] M. Lamont *MOYAB 101, IPAC 2013 Proceeding*, 2013.

[91] ALICE Collaboration, "Letter of Intent for the Upgrade of the ALICE Experiment," Tech. Rep. CERN-LHCC-2012-012. LHCC-I-022, CERN, Geneva, Aug 2012.

[92] ALICE Collaboration *Eur. Phys. J. C*, vol. 68, p. 89, 2010.

[93] ALICE Collaboration *Eur. Phys. J. C*, vol. 68, p. 345, 2010.

[94] ALICE Collaboration *Phys. Lett. B*, vol. 704, p. 442, 2011.

[95] ALICE Collaboration *Eur. Phys. J. C*, vol. 73, p. 2456, 2013.

[96] H. Bethe *Annalen d. Physik*, vol. 397, p. 325, 1930.

[97] F. Bock *Master thesis (unpublished)*, 2012.

[98] T. Dahms *arXiv:0810.3040 [nucl-ex]*, 2008.

[99] *CERN Program Library Long Writeup W5013*, 1995.

[100] R. Averbeck *private communication.*

[101] I. Erdemir *Master thesis (in preparation)*, 2014.

[102] C. Tsallis *J. Stat. Phys.*, vol. 52, p. 479, 1988.

[103] ALICE Collaboration *Phys. Lett. B*, vol. 717, p. 162, 2012.

[104] ALICE Collaboration *Eur. Phys. J. C*, vol. 72, p. 2183, 2012.

[105] L. Landsberg *Phys. Rep.*, vol. 128, p. 301, 1985.

[106] R. I. Dzhelyadin *Phys. Lett. B*, vol. 296, p. 114, 1981.

[107] G. Gounaris and J. Sakurai *Phys. Rev. Lett.*, vol. 21, p. 244, 1968.

[108] ALICE Collaboration *JHEP*, vol. 07, p. 191, 2012.

[109] ATLAS Collaboration *ATLAS-PHYS-PUB-2011-012*, 2011.

[110] LHCb Collaboration *LHCb-CONF-2010-013*, 2010.

[111] ALICE Collaboration *Phys. Lett. B*, vol. 721, p. 13, 2013.

[112] M. Cacciari, S. Frixione, N. Houdeau, M. L. Mangano, P. Nason, *et al. JHEP*, vol. 1210, p. 137, 2012.

[113] ALICE Collaboration *Phys. Rev. D*, vol. 86, p. 112007, 2012.

[114] M. Bedjidian *et al. arXiv:hep-ph/0311048*, 2003.

[115] M. Mangano, P. Nason, and G. Ridolfi *Nucl. Phys. B*, vol. 373, p. 295, 1992.

[116] S. Alioli, P. Nason, C. Oleari, and E. Re *JHEP*, vol. 1006, p. 043, 2010.

[117] ALICE Collaboration *Phys. Lett. B*, vol. 721, p. 13, 2013.

[118] T. Gunji *private communication*.

[119] LHCb Collaboration *Phys. Rev. Lett.*, vol. 110, p. 101802, 2013.

[120] P. Braun-Munzinger and P. Crochet *Nucl. Instr. Meth. A*, vol. 484, p. 564, 2002.

[121] PHENIX Collaboration *Phys. Rev. Lett.*, vol. 104, p. 132301, 2010.

[122] PHENIX Collaboration *Phys. Rev. D*, vol. 86, p. 072008, 2012.

[123] W. Vogelsang *private communication*.

[124] M. Wilde (for the ALICE Collaboration) *arXiv:1210.5958 [hep-ex]*, 2012.

[125] T. Broeker *private communication*.

[126] ALICE Collaboration *Phys. Lett. B*, vol. 719, p. 29, 2013.

[127] ATLAS Collaboration *Phys. Rev. Lett.*, vol. 110, p. 182302, 2013.

[128] CMS Collaboration *JHEP*, vol. 1009, p. 091, 2010.

[129] O. Hinrichs *Master thesis (unpublished)*, 2012.

[130] HADES Collaboration *arXiv:1311.0216 [hep-ex]*, 2013.

[131] T. Gunji and Y. Yamaguchi *ALICE internal note*, 2014.

[132] ALICE Collaboration *CERN-LHCC-2012-012*, 2012.

[133] ALICE Collaboration *CERN-LHCC-2012-013*, 2012.

[134] ALICE Collaboration *CERN-LHCC-2013-020*, 2013.

[135] J. Alwall *et al. Comput. Phys. Commun.*, vol. 176, p. 300, 2007.

Eigenständigkeitserklärung

Hiermit versichere ich, dass ich die vorliegende Doktorarbeit selbstständig und nur mit den angegebenen Quellen und Hilfsmitteln angefertigt habe. Alle Stellen, welche Quellen entnommen wurden, sind als solche gekennzeichnet. Diese Arbeit hat in gleicher oder ähnlicher Form noch keiner Prüfungsbehörde vorgelegen.

Markus K. Köhler

Curriculum Vitae

Markus Konrad Köhler

Personal Data

Date of birth	April 26th, 1984
Place of birth	Lich, Germany
Citizenship	German
Native languages	German, Hungarian
Fluent	English

Education

11/2010 - ongoing Doctoral candidate (Dr. rer. nat) at Technische Universität Darmstadt and GSI Helmholtzzentrum für Schwerionenforschung in Darmstadt, Germany
Thesis: *Dielectron Production in proton-proton collisions with ALICE*

02/2008 - 10/2010 Master of Science in Physics at Technische Universität Darmstadt and GSI Helmholtzzentrum für Schwerionenforschung in Darmstadt, Germany
Thesis: *Dielectron Production in proton-proton collisions at ALICE*

10/2004 - 02/2008 Bachelor of Science in Physics at Technische Universität Darmstadt, Germany
Thesis: *Analysis of a Test Experiment on Photo-induced Fission of 238U at the Superconducting Darmstadt Accelerator S-DALINAC*

08/1994 - 06/2003 Degree 'abitur' from secondary school at Weidiggymnasium in Butzbach, Germany

Research and Work Experience

03/2013 - 06/2013 Research stay at Universidade São Paulo (USP), São Paulo, Brazil

11/2011 - 12/2011 Research stay at CERN, Geneva, Switzerland

05/2008 - 08/2008 Student Research Assistant at the Faculty of Light Engineering at Technische Universität Darmstadt, Germany

Publications

Low-mass dielectron production in pp and Pb–Pb collisions in ALICE
Markus K. Köhler for the ALICE Collaboration
Journal of Physics: Conference Series **446** (2013) 012049
Preprint `arXiv:1302.2049 [hep-ex]`

Suppression of Charged Particle Production at Large Transverse Momentum in Central Pb−Pb Collisions at $\sqrt{s_{\mathrm{NN}}} = 2.76$ TeV
K. Aamodt et al., ALICE Collaboration
Phys. Lett. **B 696** 30 (2011)
Preprint `arXiv:1012.1004v1 [nucl-ex]`

Co-author of more than 80 papers published in international journals with peer-reviewing (Status: June 2014)

Presentations at international conferences

- Dielectron measurements in pp, p-Pb and Pb-Pb collisions with ALICE at the LHC
  Quark Matter Conference, Darmstadt/Germany, May 2014
- Dielectron production in pp and Pb–Pb collisions with ALICE
  Hot Quarks Conference, Guanica/Puerto Rico, October 2012